SYNTHESIS AND CHARACTERIZATION OF NOVEL NANOPOROUS MATERIALS FOR ACIDIC AND BASIC GAS ADSORPTION

by

Dushyant Barpaga

Dissertation

Submitted to the Faculty of the

Graduate School of Vanderbilt University

in partial fulfillment of the requirements

for the degree of

DOCTOR OF PHILOSOPHY

in

Chemical Engineering

May 2016

Nashville, Tennessee

Approved:

M. Douglas LeVan, Ph.D.

G. Kane Jennings, Ph.D.

Sandra J. Rosental, Ph.D.

Peter N. Pintauro, Ph.D.

To Mom, Dad, Divya and Mariana,

Thank you for your love and support.

ACKNOWLEDGEMENTS

First and foremost, I would like to acknowledge my research advisor, Professor M. Douglas LeVan. I will be forever grateful for his guidance and his patience, which have taught me how to become a better researcher. His appreciation for the work, passion for teaching, and sincere integrity have and will continue to be an inspiration. He has instilled confidence in my abilities and has provided me with numerous opportunities to advance my presentation skills. I humbly thank him for all of his efforts to help me succeed and I am truly honored to have been a part of his research group.

I would also like to acknowledge the members of my Ph.D. committee, Professors Kane Jennings, Peter Pintauro, and Sandra Rosenthal. Their advice and critiques have been extremely helpful in pursuing new ideas that have advanced my research. They have also been an excellent source of motivation, which has enabled me to remain on track to complete my thesis.

For funding this research, the U.S. Edgewood Chemical Biological Center, the Army Research Office, and the Defense Threat Reduction Agency are also graciously acknowledged. It has been a privilege to attend their annual working group meetings and network with multiple groups, scientists and engineers affiliated with these agencies. I would like to acknowledge Greg Peterson, Jared Decoste and John Mahle from ECBC for many engaging discussions during monthly telephone conferences that have provided extremely useful guidance along the course of the project.

Multiple staff members in our department have also been invaluable resources during my graduate career. I would like to thank Mary Gilleran, Rae Uson and Mark Holmes for all of their general assistance. I would also like to thank Rossane Delapp in the Department of Civil and Environmental Engineering for helping me with the TGA, and Dr. James McBride in the Department of Chemistry for helping me with the TEM.

I would like to thank other members of the LeVan research group that have supported me through stimulating research discussions. Specifically, I would like to acknowledge Amanda Furtado for introducing me to the research and teaching me the numerous tools and techniques fundamental to my work. I would also like to acknowledge Trenton Tovar for his support during experiments, providing constructive criticism on presentations, being an excellent friend, and an inspiration for me to become a better researcher. I would also like to thank Tim Giesy and Lucas Mitchell for stimulating research discussions.

This thesis and my research efforts would not be possible without the contributions of my loving family and friends. I thank my mother, my father, and my sister for always providing me with the atmosphere and the environment to succeed. Their immeasurable sacrifices have allowed me to pursue my dreams and I cannot express my gratitude enough for their support and love. I thank all of my friends, old and new, for making my graduate school experience as memorable and enjoyable as possible. Thank you all for always being there for me.

Finally, I wish to acknowledge my best friend, my biggest supporter, and my love, Mariana Rendon. She continues to encourage me during times of struggle and celebrates in my times of success. No matter how far apart we may be, she is always there to provide the motivation and strength I need. I am beyond grateful to have your love and the love of your family.

TABLE OF CONTENTS

LIST OF TABLES

LIST OF FIGURES

CHAPTER I

INTRODUCTION

Adsorbent technology employing specificity towards a broad range of target molecules is becoming increasingly important for a variety of applications such as filtration, separation, purification and/or storage of fluids. The development of newer, more efficient adsorbent materials is a growing concern for civilian, first responder, and military uses.

Some commercial applications include desiccants, ion exchange, catalysis, and filtration of breathable air in a toxic environment containing harsh chemical contaminants. The most common adsorbents used for such applications fall into four major categories: carbons, zeolites, silicas, and aluminas. Activated carbon has traditionally been used as an all purpose adsorbent given its hydrophobic nature. It was commercialized during World War I for its use in filters to remove harsh chemical agents from the air. Zeolites are aluminosilicates of alkali earth elements accommodating cations such as sodium, potassium, calcium, magnesium and others. Given their unique surface chemistries and microporous, crystalline pore structure, they have been commercialized for their use in ion exchange and catalysis. Silica and aluminas have mainly been commercialized for their use as desiccants.[1]

This dissertation is focused on the development and characterization of novel, nanoporous adsorbents and how they compare with similar commercial analogues. In the approach to synthesize unique porous materials, an underlying theme involving the use of metal salts exists in this research. The oxidation and reduction tendency of metals occurring naturally as salts provides excellent reactive potential that can be useful for selective combination with various chemical species. For this reason, metal salts are employed in this work not only as precursors for synthesis, but also as reactive moieties for further functionalization of existing high performance adsorbents.

In a recent memorandum by the Toxic Industrial Chemical/Toxic Industrial Material (TIC/TIM) task force,[2] a list of prioritized hazardous chemicals of interest showed light gases such as NH_3 an SO_2 in the top ten. Due to their high volatility, light toxic gases at low concentrations are difficult to capture. For use in potential filtration applications, novel adsorbents must have broad scale capability against many types of adsorbate molecules. Therefore, the majority of materials synthesized in this research will incorporate metal salts as functionalities on a biphasic carbon silica composite (CSC) adsorbent to target a wide range of low concentration, light gases with NH_3 and SO_2 as representatives of both ends of the spectrum (reducers/basic gases and oxidizers/acidic gases). As the primary measure of performance, an equilibrium capacity will be calculated representing the quantity of NH_3/SO_2 able to be captured per weight of the adsorbent. Other characterization techniques such as powder X-ray diffraction, thermogravimetric analysis, porosimetry measurements, diffuse reflectance infrared Fourier transform spectroscopy (DRIFTS), Raman spectroscopy, X-ray photoelectron spectroscopy, and electron microscopy will be used in this project to understand the pore structure, chemical composition, surface reactivity, surface functionality, and overall adsorption behavior of the synthesized adsorbents.

In order to design and synthesize an effective adsorbent, it is important to understand the interactions between the adsorbate and the adsorbent. Along with the understanding of the adsorbate-adsorbent interactions, the surface area and porosity of the adsorbent must be taken into consideration. An effective adsorbent having a high surface area as a result of high porosity must be nanoporous. Three basic forces that make up adsorbate-adsorbent interactions include dispersion, electrostatic and chemical bonds.[1] Adsorption as a result of dispersion and electrostatic forces is known as physical adsorption (or physisorption). On the other hand, adsorption resulting in the formation of a chemical bond between the adsorbate and the adsorbent is known as chemical adsorption (or chemisorption). Most commercial adsorbents perform physisorption on adsorbates, although chemisorption binds adsorbates

irreversibly. Therefore, it is important to take advantage of chemisorptive properties of materials such as metal salts during the design and synthesis of novel adsorbents.

In Chapter 2, the CSC along with its mesoporous MCM-41 precursor were functionalized with a number of single, water-soluble metal salts to introduce active sites of adsorption that can potentially react irreversibly to capture the representative TIC targets. Salt-containing MCM-41 materials were shown to have increased ammonia adsorption given the exposed hydroxyl surface of the mesoporous silica along with larger pore volumes for higher metal loadings. CSCs with metal salts had comparable ammonia capacities and much more significant sulfur dioxide capacities given the addition of a basic carbon phase with an affinity for acid-forming gas. K_2CO_3 and $ZnCl_2$ were found to be the most effective individual impregnants for NH_3 or SO_2 adsorption, respectively. [3–5]

In Chapter 3, the addition of both K_2CO_3 and $ZnCl_2$ sequentially on CSC as well as other single phase substrates was shown to react via in-pore synthesis to form a well-dispersed insoluble $ZnCO_3$. Found to be effective as individual impregnants, the combination of both metal salts to form a precipitate resulted in the consolidation of high NH_3 and SO_2 capacities. Washing the in-pore synthesized material with water resulted in the removal of only unreacted potassium and chlorine ions leaving behind the newly formed precipitate. As compared with solution impregnation of poorly dispersed, pre-synthesized $ZnCO_3$, the in-pore synthesis via dual salt functionalization provided greater TIC adsorption.

In Chapter 4, dual salt functionalization of various combinations of metal chlorides with potassium carbonate or potassium phosphate was shown to form insoluble precipitates on CSC and MCM-41. The adsorption performance of the precipitates was justified by differences in the pH of the functionalized materials. The acidity of the metal chloride or basicity of the potassium salt alone did not influence the overall pH of the dual functionalized material. Zinc chloride, copper chloride or potassium carbonate containing composites yielded significant increases in TIC adsorption, while composites containing magnesium chloride or

potassium phosphate did not. The incorporation of K_2CO_3 and $ZnCl_2$ to form $ZnCO_3$ on CSC provided the highest adsorption capacities for both NH_3 and SO_2.

In Chapter 5, the presence of metal salts as building blocks during the synthesis of porous materials was explored. Metal-organic framework (MOF) materials possess well-ordered crystalline structures containing extremely high surface area and pore volumes leading to significant potential in light gas storage applications. In this characterization study, the well-known water stability issues with MOF materials[6] were studied using carboxylate-based MOFs analyzed with spectroscopic measurements before and after exposure to various levels of hydration in order to interpret manipulations in chemical bonding as a result of water adsorption. Cu-BTC, known to degrade in humid conditions, was examined via Raman spectroscopy and results showed that upon water adsorption, copper dimer bonds that hold the backbone of the structure together were broken, ultimately leading to its degradation. Mg-DOBDC showed higher susceptibility to water as evident by permanent IR peak shifts and peak dissolutions when examined via diffuse reflectance infrared spectroscopy (DRIFTS). Other MOFs such as Fe-BTC and Ni-DOBDC showed little change in spectroscopic signatures even after extreme water exposure, justifying previously determined stability differences.

Finally, Chapter 6 summarizes the major conclusions and some recommendations for future work as a result of this research.

References

(1) R. T. Yang. Adsorbents: Fundamentals and Applications. **2003**

(2) Toxic Industrial Chemical/Toxic Industrial Material Task Force. TIC/TIM Task Force Prioritization and Application Recommendations. Memorandum. Joint Program Executive Office for Chemical and Biological Defense. **Feb, 2009**.

(3) Fortier, H.; Zelenietz, C.; Dahn, T. R.; Westreich, P.; Stevens, D. A.; Dahn, J. R. SO_2 Adsorption Capacity of K_2CO_3-Impregnated Activated Carbon as a Function of K_2CO_3 Content Loaded by Soaking and Incipient Wetness. *Appl. Surf. Sci.*. **2007**, *253*, 3201-3207.

(4) Fortier, H.; Westreich, P.; Selig, S.; Zelenietz, C.; Dahn, J. R. Ammonia, Cyclohexane, Nitrogen and Water Adsorption Capacities of an Activated Carbon Impregnated with Increasing Amounts of $ZnCl_2$, and Designed to Chemisorb Gaseous NH_3 from an Air Stream. *J. Colloid Interface Sci.*. **2008**, *320*, 423-435.

(5) Barpaga, D.; LeVan, M. D. Functionalization of carbon silica composites with active metal sites for NH_3 and SO_2 adsorption. *Microporous Mesoporous Mater.*. **2016**, *221*, 197-203.

(6) Burtch, N. C.; Jasuja, H.; Walton, K. S. Water Stability and Adsorption in Metal-Organic Frameworks. *Chem. Rev.*. **2014**, *114*, 10575-10612.

CHAPTER II

FUNCTIONALIZATION OF CARBON SILICA COMPOSITES WITH ACTIVE METAL SITES FOR NH_3 AND SO_2 ADSORPTION

2.1 Introduction

Recently, our group has developed a biphasic carbon-silica composite (CSC) material to target a wide spectrum of adsorbates.[1–3] Originally reported by Glover et al.,[1] this biphasic adsorbent consists of a polar siliceous phase and a non-polar carbonaceous phase that has been studied for the adsorption of various light gases such as carbon dioxide, methane, ethane, and nitrogen. The CSC consists of a carbon phase derived from polyfurfuryl alcohol and a silica phase comprised of MCM-41.

MCM-41 is a mesoporous silica material that belongs to the M41S family of materials developed by Kresge et al.[4] of the Mobile Oil Corporation. MCM-41 contains a well-ordered structure with well defined hexagonal pores that are tunable in size. Though the walls of calcined MCM-41 are made of multiple Si-O-Si bonds, the pore surfaces contain free hydroxyl groups. These free polar groups serve as useful sites for adsorption, which ultimately make MCM-41 a very good base adsorbent material, especially for interactions with polar gases such as NH_3.[4–7]

The thermosetting polymer polyfurfuryl alcohol (PFA) has been extensively studied by Foley et al.[8,9] When polymerized furfuryl alcohol undergoes pyrolysis at high temperatures (>300 °C), the ether linkages within the furan ring break apart and react to form polyaromatics and several carbonyl functionalities. By 600 °C, CH_4, CO, CO_2, and H_2O are released from the resin to form an amorphous carbon with an extensive microporous structure having pores smaller than 10 Å. The basic nature of the carbon derived from PFA promotes the adsorption of acidic/acid-forming gases such as SO_2.[3,8,9]

The synthesis of CSC simply involves the addition of furfuryl alcohol, with toluene as the solvent, to a pre-synthesized sample of MCM-41. The furfuryl alcohol is allowed to disperse through the pores of the silica and polymerize. After polymerization, the product is subjected to pyrolysis/carbonization, resulting in the formation of the biphasic material containing porous carbon within a well ordered silica matrix. The performance of CSCs for use as a biphasic adsorbent was tested by Furtado et al.[3] via full breakthrough capacity measurements for NH_3 and SO_2. Relative to the independent precursors, PFA-derived carbon and MCM-41, the CSC showed an improvement in the SO_2 capacity and a comparable NH_3 capacity, attributed to the basic nature of the carbon and the remaining exposed silica surfaces, respectively. The formation of micropores after carbonization diversified the pore size distribution of the material, which helped to promote adsorption as well.

In other work by Furtado et al.,[7] various metal salts dissolved in an aqueous solution were mixed with calcined MCM-41 via a wet impregnation through which metal sites accessed the porous network of MCM-41. The water solvent was removed through evaporation resulting in the synthesis of metal-salt-containing-MCM-41. The salt incorporated MCM-41 materials were tested for only NH_3 adsorption. It was concluded that [Zn Salt]-MCM-41 (from $ZnCl_2$, $ZnSO_4$, and $Zn(NO_3)_2$), $Cu(NO_3)_2$-MCM-41, and $Fe_2(SO_4)_3$-MCM-41 provided the highest capacities, between 6-7 mol NH_3/kg total sample after being dried at 120 °C.

Dahn et al.[10,11] also studied the effects of metal salt functionalization on toxic gas adsorption. In their work, however, the salts were loaded on commercially purchased activated carbon via incipient wetness rather than on synthesized mesoporous silica loading via "wet" impregnation as with Furtado et al.[7] In one study, Dahn et al.[11] analyzed NH_3 adsorption as a function of $ZnCl_2$ loading on activated carbon. Their results show that a maximum capacity of 2.7 mol NH_3/kg total sample was obtained at a loading of ∼30 wt% $ZnCl_2$. They also concluded that the stoichiometric reaction ratio, x, between $ZnCl_2$ and NH_3 to form $Zn(NH_3)_xCl_2$, at the loading of $ZnCl_2$ that resulted in the highest NH_3 capacity, was ap-

proximately 1.65. According to their results, this reaction ratio is dependent on the partial pressure of ammonia used in the capacity measurements, which in their case was 1000 ppm by volume. In a separate study, Dahn et al.[10] also analyzed SO_2 adsorption as a function of K_2CO_3 loading on activated carbon. From that work, their results show that a maximum capacity of ∼1.8 mol SO_2/kg total sample was obtained at a loading of ∼20 wt% K_2CO_3.

The goal of this study is to extend the filtration capability of one adsorbent material to target both basic and acidic gas adsorbates. Building upon the strategies used by Furtado et al.[7] and Dahn et al.,[10,11] the biphasic CSC material originally designed for this purpose is further enhanced by the incorporation of metal salts to promote the adsorption of both NH_3 and SO_2. Similar to unsaturated metal centers in MOFs, metal cations in zeolites, and impregnations within activated carbon, the addition of metal salts within CSCs is expected to enhance adsorption by providing sites for potential redox reactions and chemisorption. Therefore, a variety of water-soluble metal salts similar to the ones found to be effective within MCM-41 and activated carbon will be incorporated into the biphasic adsorbent. Specifically, $ZnCl_2$, $CuCl_2$, $MgCl_2$, $Cu(NO_3)_2$, K_2CO_3, and K_3PO_4 are added to the CSC at various concentrations. Along with performance measurements from breakthrough capacities, the structural integrity and textural properties of the synthesized adsorbents are characterized.

2.2 Experimental Methods

Materials

Tetraethyl orthosilicate (TEOS) was purchased from Sigma Aldrich. Hexadecyltrimethylammonium chloride (CTAC, 25% in water) was purchased from Pfaltz and Bauer. A solution of ammonium hydroxide (29 wt.% in water) and Cab-O-Sil M5 were purchased from Fisher Scientific. Furfuryl alcohol (99%) and toluene (99%) were purchased from Sigma Aldrich. Zinc chloride ($ZnCl_2$), potassium carbonate (K_2CO_3), potassium phosphate (K_3PO_4), and magnesium chloride ($MgCl_2$) were purchased from Sigma Aldrich. Copper

nitrate ($Cu(NO_3)_2$) and copper chloride ($CuCl_2$) were purchased from Fisher Scientific. Gas cylinders of 1500 ppmv ammonia in helium, 500 ppmv sulfur dioxide in He, and ultrahigh purity helium were purchased from A-L Compressed Gas.

Synthesis Procedures

MCM-41

The synthesis of MCM-41,[12] involves a liquid crystal templating mechanism in which an ionic surfactant (e.g., CTAC) of certain chain length is mixed into a polar solution (ammonium hydroxide in water). After the added surfactant groups conglomerate to form micelles, a solution containing TEOS is slowly added, which interacts with the polar head groups to form a liquid crystal around the boundary of the micelle. The silicate source forms a templated silica matrix taking on the shape of the surfactant micelles. Upon completion of the synthesis, the surfactant is burned off during high temperature calcination (550 °C), leaving behind the well-ordered mesoporous silica matrix.

CSC

The synthesis of the carbon silica composite (CSC) involves the deposition of the carbon source within the pores of pre-synthesized MCM-41. An aqueous solution containing ∼0.1 g of $AlCl_3$ is mixed with ∼0.9 g of calcined MCM-41 to increase the acidity of the pores and promote polymerization of the furfuryl alcohol on the substrate. This solution is dried and re-calcined at 540 °C. Then, a carbon precursor solution containing 4 mL of furfuryl alcohol with 46 mL toluene (∼8% by volume furfuryl alcohol) is allowed to polymerize onto the aluminated MCM-41 at room temperature for 3 days. After this, the solution is placed into a Parr reactor and heated in an oven at 80 °C for 24 hours to ensure complete polymerization. The as-synthesized product (filtered and dried) is subject to pyrolysis under a N_2 purge stream at 600 °C, and carbonization occurs to form the biphasic CSC material.

Compared to the original CSC synthesis procedure of Glover et al.,[1] our carbonized CSC material consists of a 90% reduction in furfuryl alcohol content during synthesis. Herein, this optimized material with enhanced adsorption capacities relative to the original composite material is referred to as CSC.

CSC with Metal Salts

The synthesis of CSCs with metal salts is conducted via incipient wetness impregnation. In this procedure, an aqueous solution containing the metal salt of interest is dribbled onto the pre-synthesized CSC until wet and allowed to air dry. After removal of water through evaporation, the desired quantity of metal salt remains within the pores of the CSC. Various concentrations of each metal salt (10, 30, 50, 65 wt%) are added to the CSC as well as to MCM-41 for comparison. After impregnation, to further remove any adsorbed water, samples are degassed in a vacuum oven at 60 °C for a minimum of 2 hours prior to any characterization. The resulting fine powders are used for characterization and adsorption performance measurements.

Materials Characterization

Porosimetry

For textural characterization, adsorption equilibrium isotherms are measured using a Micromeritics ASAP 2020 at -196 °C with nitrogen as the analysis gas. Before analysis, approximately 0.1 g of each sample is degassed under vacuum (20 μbar) and heated to 120 °C. The BET method was used to determine surface areas. The reported pore volumes, calculated using density functional theory, correspond to $P/P_0 \cong 0.99$.

X-ray Diffraction

Powder X-ray diffraction patterns were used to confirm the long-range structure of the base composite material made from mesoporous silica. These patterns are measured using a

Scintag X1h/h automated powder diffractometer with Cu target, a Peltier-cooled solid-state detector, a zero background Si(5 1 0) support, and a copper X-ray tube as the radiation source.

Microscopy

Transmission electron microscopy measurements are performed using the FEI Tecnai Osiris consisting of a fully digital 200 kV S/TEM system that allows EDX signal detection. STEM images provided color-coded spatial resolution of specific elements of interest for each sample. Samples are prepared by dissolving small quantities (∼10 mg) of adsorbent in 5 mL of H_2O. The solution is dribbled onto a lacey carbon TEM grid and allowed to air dry before analysis using the microscope.

Adsorption Capacity

As the primary measure of performance, adsorption capacities are calculated from room temperature gas adsorption of NH_3 and SO_2 on all synthesized materials using breakthrough measurements. These measurements are performed using a breakthrough apparatus, a schematic of which is shown elsewhere.[7] With accumulation of target adsorbate in the gas phase being negligible relative to that in the adsorbed phase, the capacity of the adsorbent material, n (mol adsorbate/kg adsorbent), is calculated from

$$n = \frac{F}{m} \int_0^\infty (C_0 - C)\, dt \tag{1}$$

where C_0 is the feed concentration in units of mol/m^3, and C is the effluent concentration at time t. The volumetric flow rate of gas through the adsorbent bed, F, is held constant at 25 sccm. Once adsorption is complete, the effluent concentration of analysis gas measured by the mass spectrometer in the apparatus mentioned above is normalized as the inlet concentration,

C_0, from the feed. The mass of the sample, m, varies between 15-30 mg and is contained in a small cylindrical adsorbent bed with an internal diameter of 4 mm.

The standard deviations in adsorption capacities that is representative of differences between measurements on the same sample is approximately 6% and 3% for NH_3 and SO_2, respectively. These are calculated from several measurements of NH_3 and SO_2 capacities on MCM-41 synthesized from the same batch. For many of the synthesized adsorbents in this study, in order to confirm reproducibility, the materials were re-synthesized (multiple batches). This implies that deviations in capacity measurements for the same material are due to not only the standard deviation from measurement to measurement but also differences in batch-to-batch synthesis of the same material. Overall, the error in NH_3 and SO_2 capacities reported, calculated using capacity measurements of MCM-41 synthesized in three separate batches, is approximately $\pm 12\%$ and $\pm 9\%$, respectively.

2.3 Results and Discussion

To appropriately understand the differences between metal functionalization of MCM-41 and CSC, as well as the effect of increasing salt content, six representative materials are analyzed using X-ray diffraction, porosity, and microscopy techniques. These adsorbents are MCM-41, CSC, [10 wt% $ZnCl_2$]-MCM-41, [10 wt% K_2CO_3]-MCM-41, [10 wt% $ZnCl_2$]-CSC, [10 wt% K_2CO_3]-CSC, and [50 wt% $ZnCl_2$]-CSC.

Porosimetry

Nitrogen adsorption equilibrium isotherms for the selected materials are shown in Figure 2.1. MCM-41 has a Type IV isotherm based on the IUPAC classification scheme. It has an inflection point located at a reduced partial pressure, P/P_0, of $\sim$0.3 and some hysteresis during desorption, which is characteristic of capillary condensation in the mesopores. The CSC material is both microporous and mesoporous and exhibits more Type I behavior than

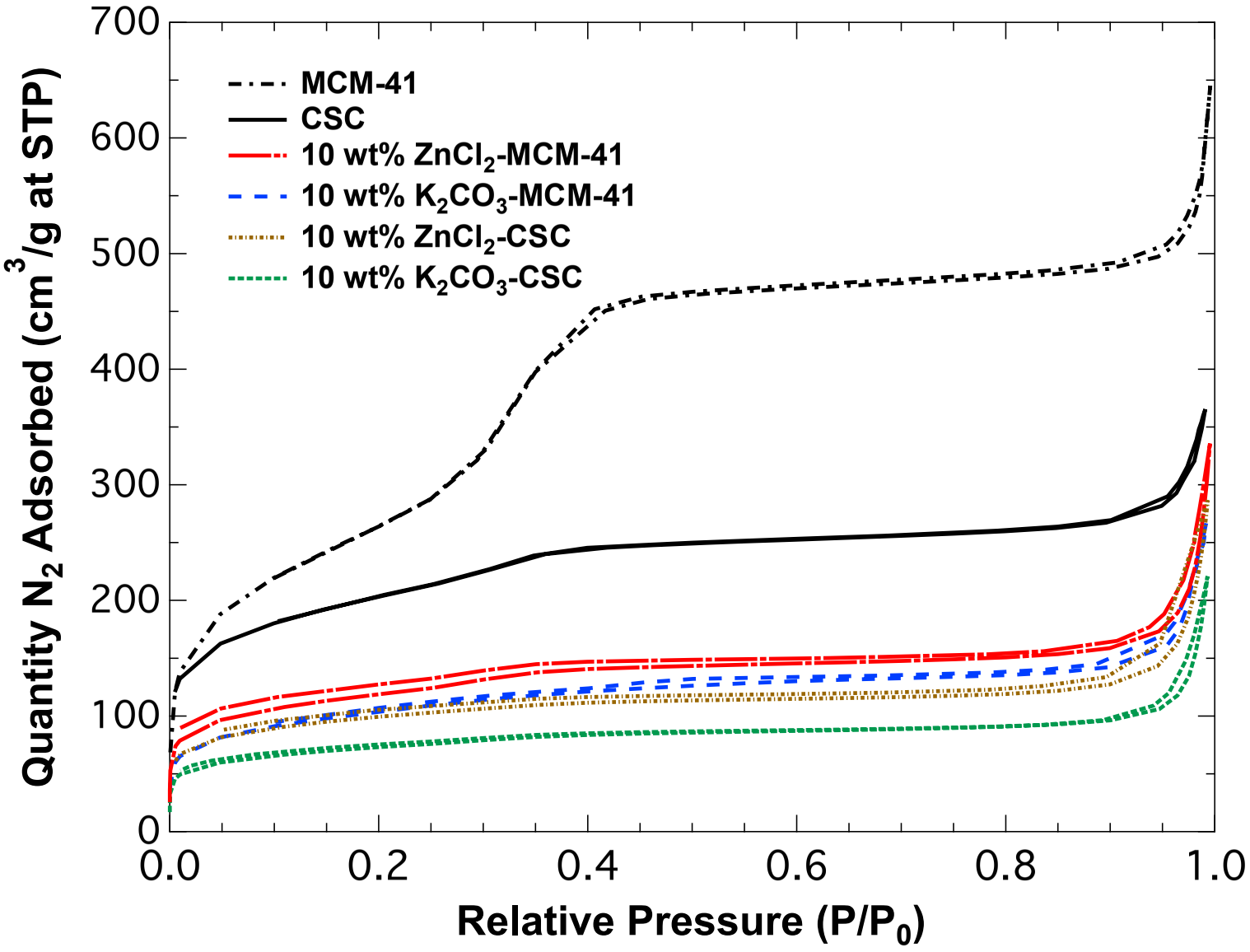

Figure 2.1. N_2 adsorption isotherms for MCM-41 and CSC functionalized with select, single metal salts.

Type IV, given the lack of an inflection point as well as a sharper increase in adsorbed N_2 at low P/P_0 followed by a more rapid leveling off as P/P_0 approaches 1. The addition of a carbon phase also significantly reduces the amount of adsorbed nitrogen, which is likely due to steric limitations caused by smaller pore sizes. Upon functionalization with metal salts, isotherms maintain Type I behavior and as the salt content increases, the quantity of nitrogen adsorbed decreases compared to the non-impregnated substrate. This indicates the inability of nitrogen to access adsorption sites due to pore blockage and agglomeration of incorporated metal salts.

Pore size distributions for the same materials are shown in Figure 2.2. As expected, it is evident that a large percentage of the pore volume for MCM-41 has a pore size centered at approximately 35 Å. Relatively sharper peaks for MCM-41 are shown given the uniform pore sizes developed through the controlled synthesis procedure. For the CSC and metal impregnated materials, significant amounts of the pore volume are shifted towards the micropore region and centered around pore sizes smaller than 20 Å. The broadened distribution implies that carbonization and further functionalization reduces the uniformity of pore sizes. Overall, functionalization with metal salts results in smaller pore-sized adsorbents due to the successful incorporation of metal salts in the pores of both the CSC and MCM-41.

Adsorption equilibrium isotherms also allow a quantitative analysis of textural characterization via surface area and pore volume calculations as shown in Table 2.1. Surface area measurements directly correlate to the quantity of nitrogen adsorbed. Calculated using the BET method, upon introducing a carbon phase and/or further functionalization with metal salts, the surface area decreases compared to parent MCM-41 or single phase carbon materials such as BPL activated carbon. Similarly, the pore volumes also decrease upon functionalization with metal salts, as should be expected. Drastic changes in pore characteristics are seen with increased salt concentrations as a result of agglomeration and pore hinderance issues.

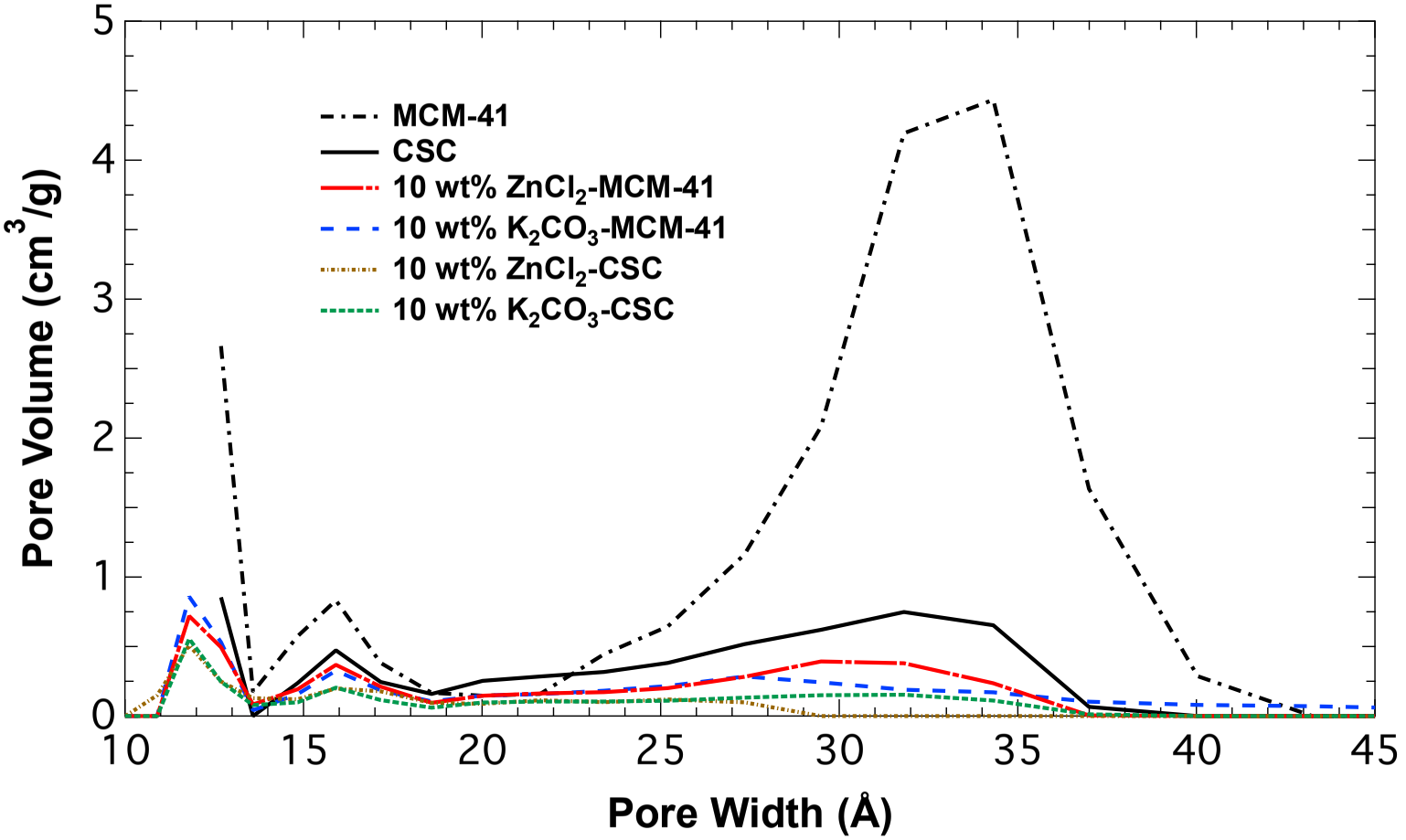

Figure 2.2. Pore size distributions for MCM-41 and CSC functionalized with select, single metal salts.

Table 2.1. BET surface area and pore volumes of MCM-41 and CSC functionalized with various concentrations of active metal sites.

	Surface Area (m^2/g)	Pore Volume (cm^3/g)
MCM-41	990	1.00
BPL AC	1050	0.55
CSC	690	0.57
[10 wt% $ZnCl_2$]-MCM-41	480	0.63
[10 wt% K_2CO_3]-MCM-41	400	0.45
[10 wt% $ZnCl_2$]-CSC	290	0.40
[10 wt% K_2CO_3]-CSC	250	0.34
[50 wt% $ZnCl_2$]-CSC	17	0.12

X-ray Diffraction

XRD patterns shown in Figure 2.3 are analyzed to interpret the structural integrity of the pores of the synthesized adsorbents. MCM-41 is a well-ordered structure with distinct peaks in the low angle spectrum. The strongest peak at $\sim 2.5^\circ$ 2θ corresponds to the (100) basal plane. Two peaks between 4.5° and 5.5° 2θ correspond to the distance between planes (110) and (200). The addition of an amorphous carbon phase causes an interference in signal as shown by reduced intensities. The CSC structure indeed maintains the hexagonal order of the silica backbone as evident by the similarity of identifiable peaks relative to MCM-41. Similarly, patterns for the selected MCM-41 and CSC materials functionalized with metal salts also reveal evidence of an ordered phase showing characteristic peaks. Increased loading of metal salt on each substrate results in apparent diminishing order of the silica phase, which is due to interference from the incorporated state rather than reduced "crystallinity".

Microscopy

TEM images of the selected materials are shown in Figure 2.4. All samples show evidence of mesopores from the MCM-41 contribution. The well-ordered porosity of each synthesized adsorbent is evident in theses images through axial and radial planes (in cylindrical geometry) as seen by parallel lines and/or honeycomb-shaped matrix. To confirm the well-mixed dispersion of metal salt impregnants on the CSC substrate, STEM images of $ZnCl_2$-CSC shown in Figure 2.5 provide spatial resolution of each element present in the sample. Well-ordered porosity is further shown in STEM images of silicon, oxygen, and carbon atoms that make up the base material. Results confirm that successful incorporation of $ZnCl_2$ is achieved since the zinc and chlorine atoms line the pores of the adsorbent throughout the material rather than agglomerate in a specific part of the sample.

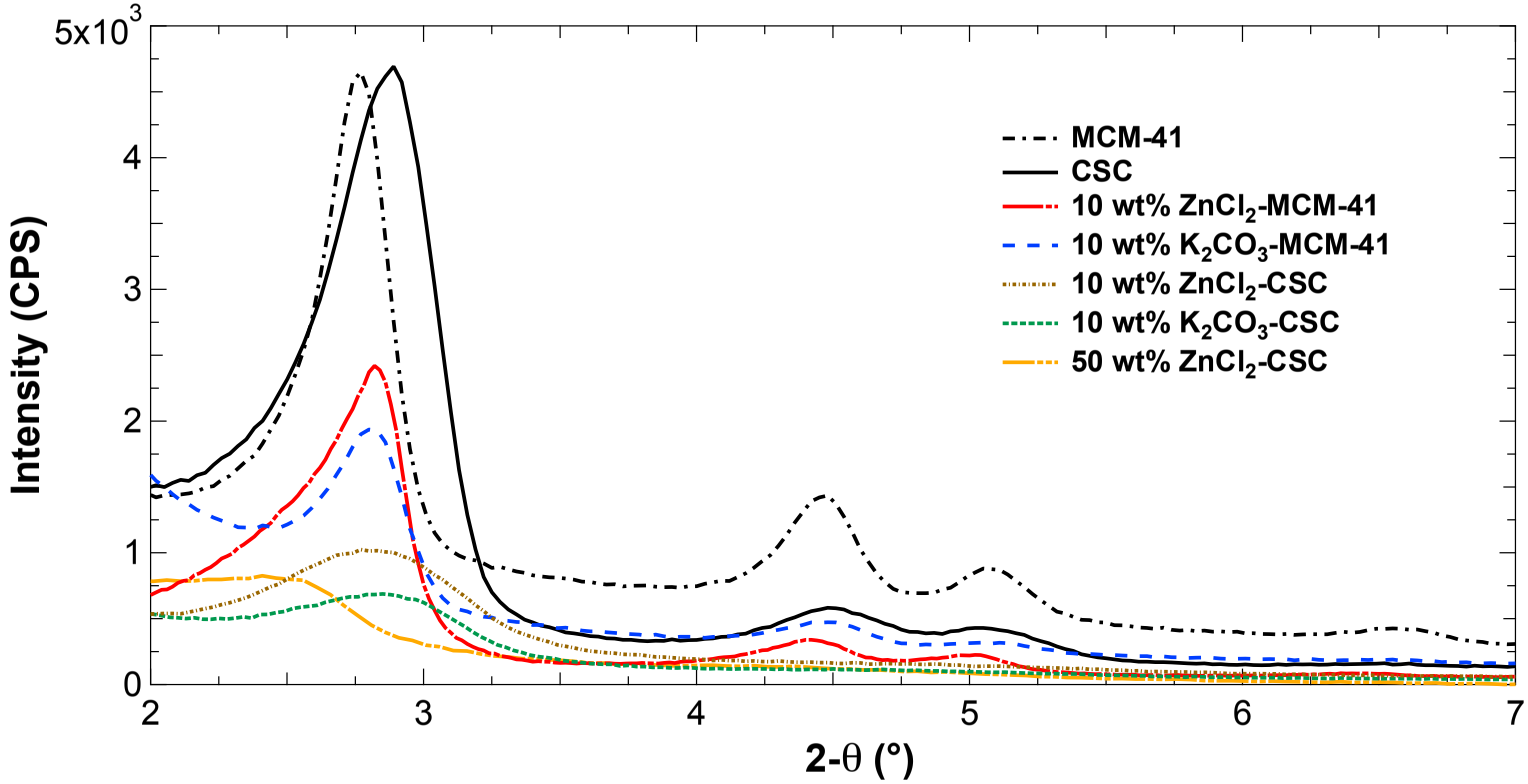

Figure 2.3. XRD patterns for MCM-41 and CSC functionalized with various concentrations of select, single metal salts.

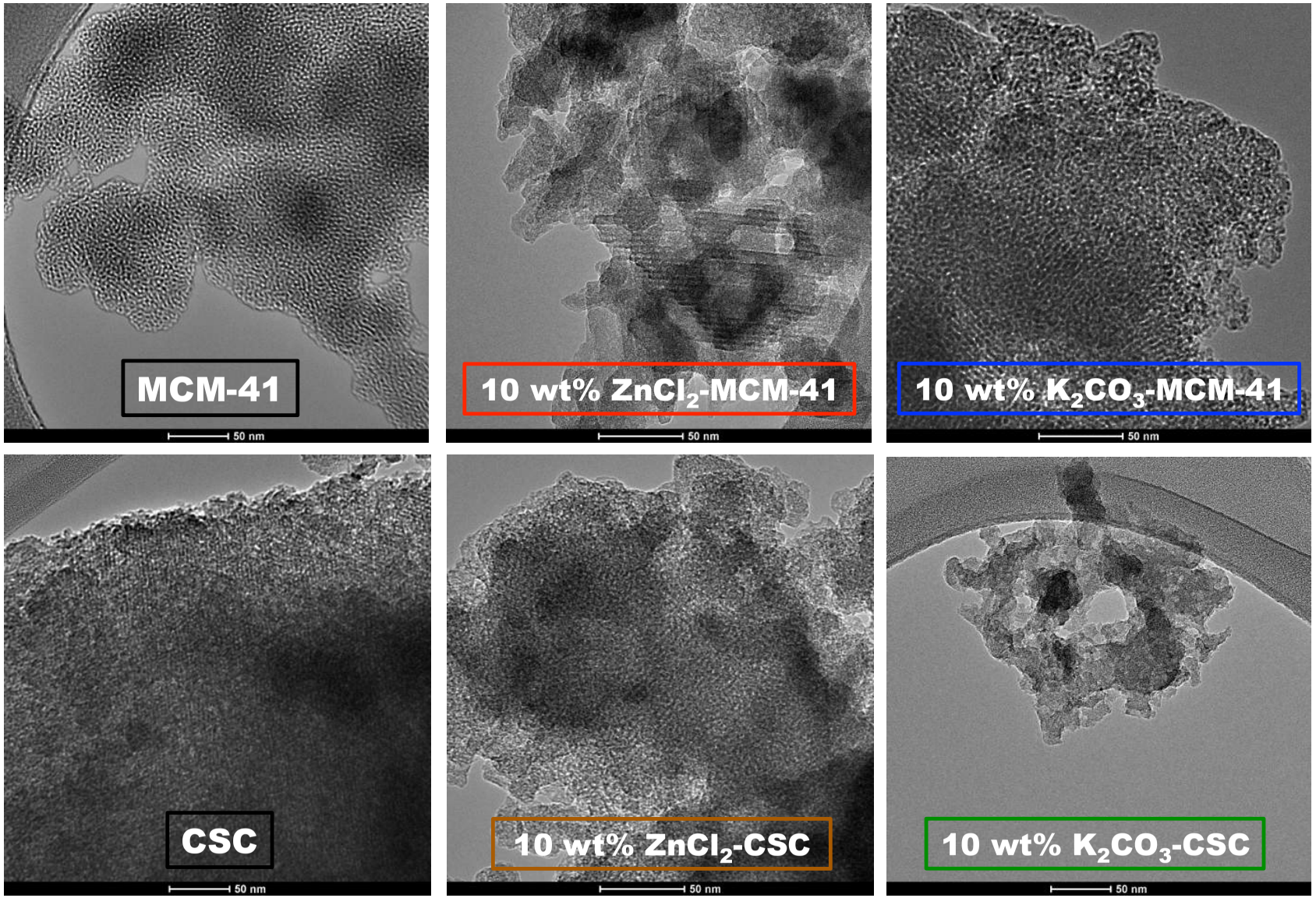

Figure 2.4. TEM images for MCM-41 and CSC functionalized with select, single metal salts.

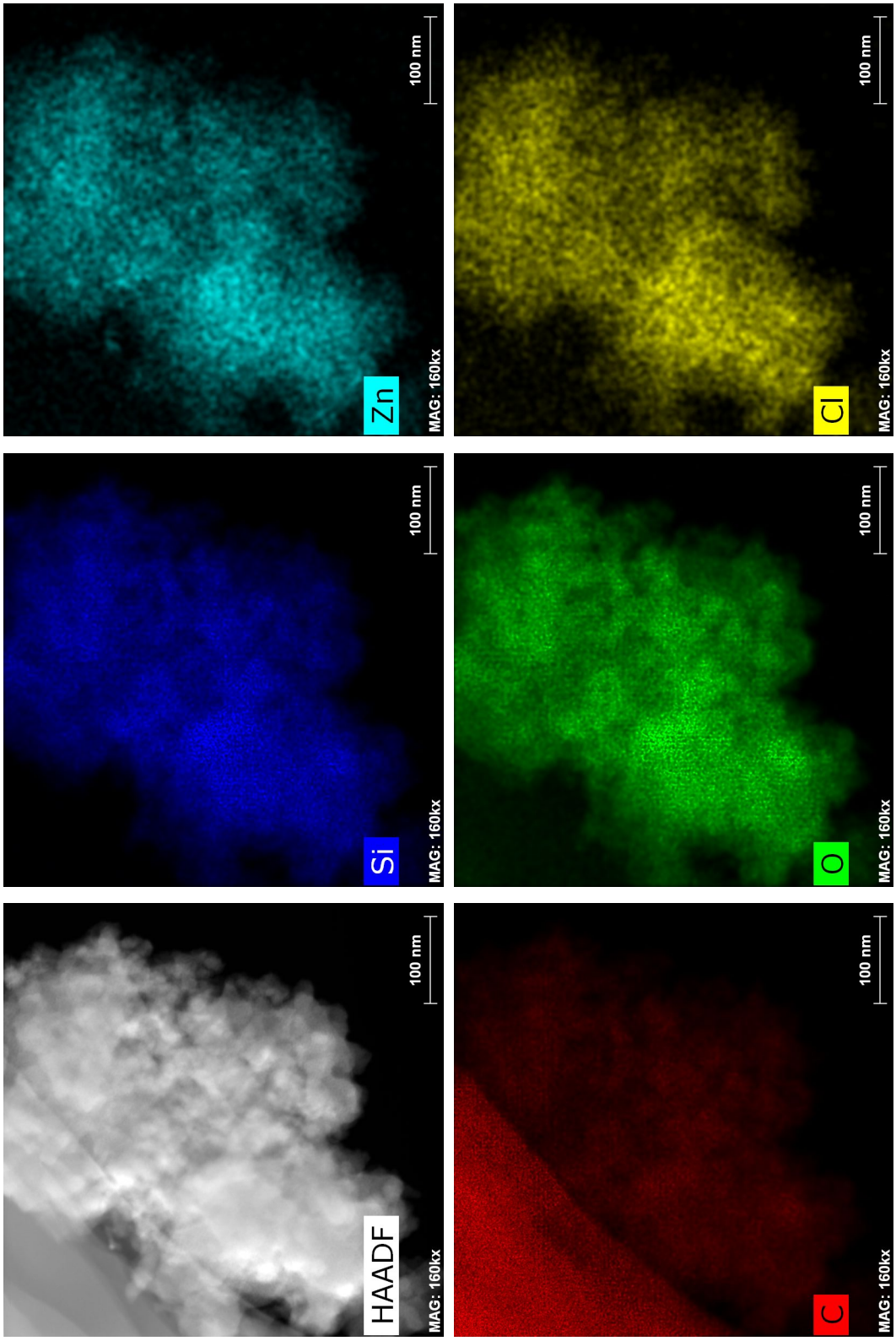

Figure 2.5. STEM images for [10 wt% $ZnCl_2$]-CSC.

Adsorption Capacity

The effect of single-salt functionalization on the adsorption capacity of NH_3 and SO_2 is shown in Figures 2.6 and 2.7, respectively. The capacities shown represent an average of multiple measurements. Metal functionalization on CSCs is compared with functionalization on MCM-41. In general, on a total weight basis, the NH_3 capacities of CSCs with metal salts are lower than the NH_3 capacities of MCM-41 with metal salts. Since the only difference between these materials is the addition of a carbon phase, the smaller pore size distribution in CSCs with metal salts limits the accessibility of NH_3 molecules to traditional adsorption sites. This implication is supported by previously mentioned N_2 adsorption equilibrium isotherms that show reduced surface areas and pore volumes for the composite relative to MCM-41 as well as reduced surface areas and pore volumes for the CSCs with metal salts relative to MCM-41 with metal salts. When comparing simply MCM-41 and CSC, the addition of a carbon phase does not reduce NH_3 adsorption capacity. This suggests that the addition of metal sites via further functionalization comes at the cost of losing traditional NH_3 adsorption sites on the base material due to reduced porosity. On the other hand, as a benefit of adding a carbonaceous phase, the increased basicity from nucleophilic carbon promotes acidic gas adsorption. Therefore, on a total weight basis, the SO_2 capacities of CSCs with metal salts are higher than the SO_2 capacities of MCM-41 with metal salts materials.

A comparison between the effectiveness of various salts yields multiple high performance candidates for each adsorbate. Among both MCM-41 and CSC functionalized materials, the incorporation of $ZnCl_2$ and $Cu(NO_3)_2$ results in the highest NH_3 capacities. NH_3 capacities up to 7.6 mol/kg and 8.8 mol/kg were obtained with $ZnCl_2$ and $Cu(NO_3)_2$ incorporation, respectively, on MCM-41 with concentrations greater than or equal to 50 wt%. NH_3 capacities up to 5.8 and 3.9 mol/kg were obtained with $ZnCl_2$ and $Cu(NO_3)_2$ incorporation, respectively, on CSC with concentrations between 10-30 wt%. As was reported by

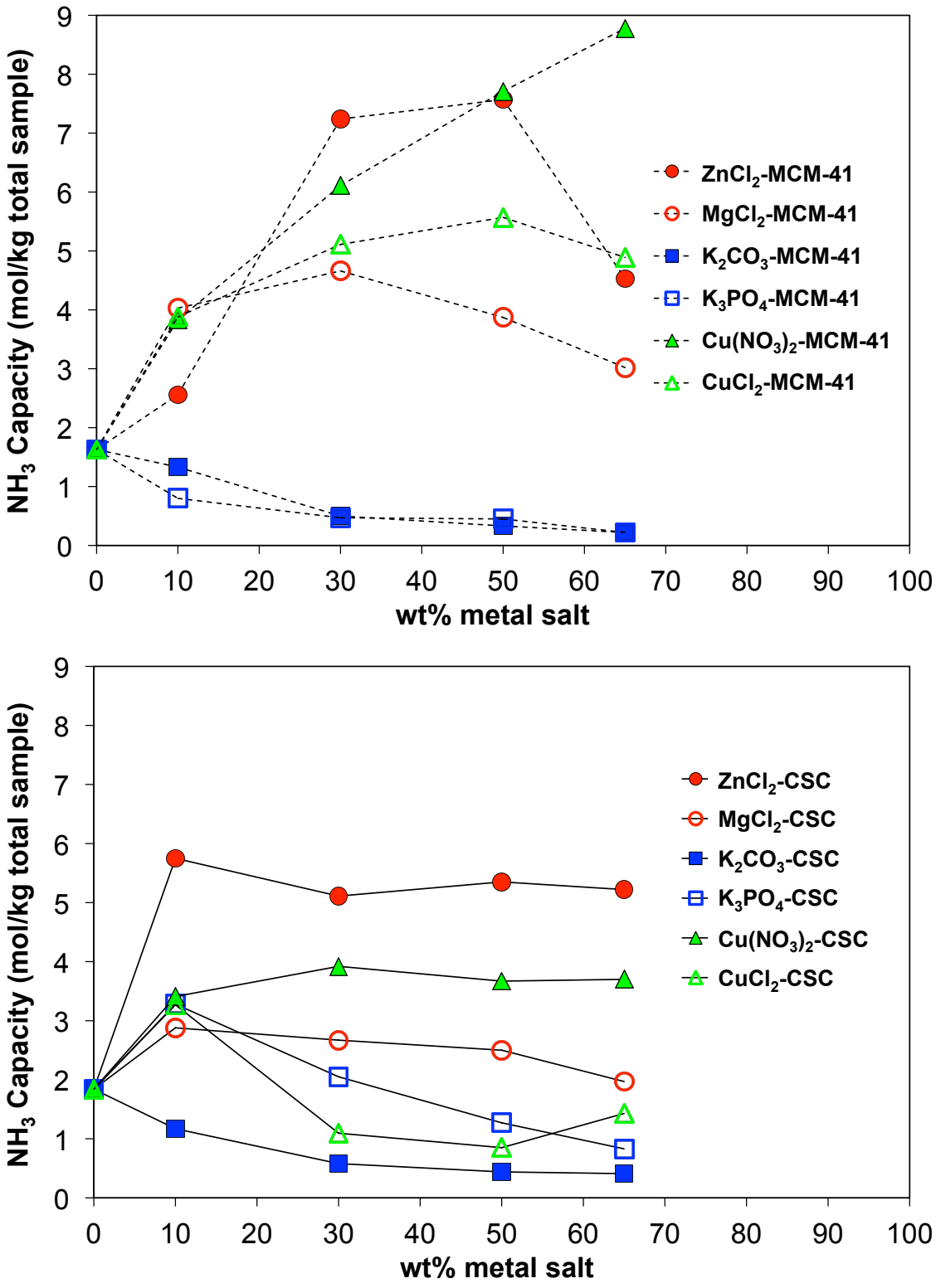

Figure 2.6. NH_3 adsorption capacity measurements for MCM-41 and CSC functionalized with select, single metal salts.

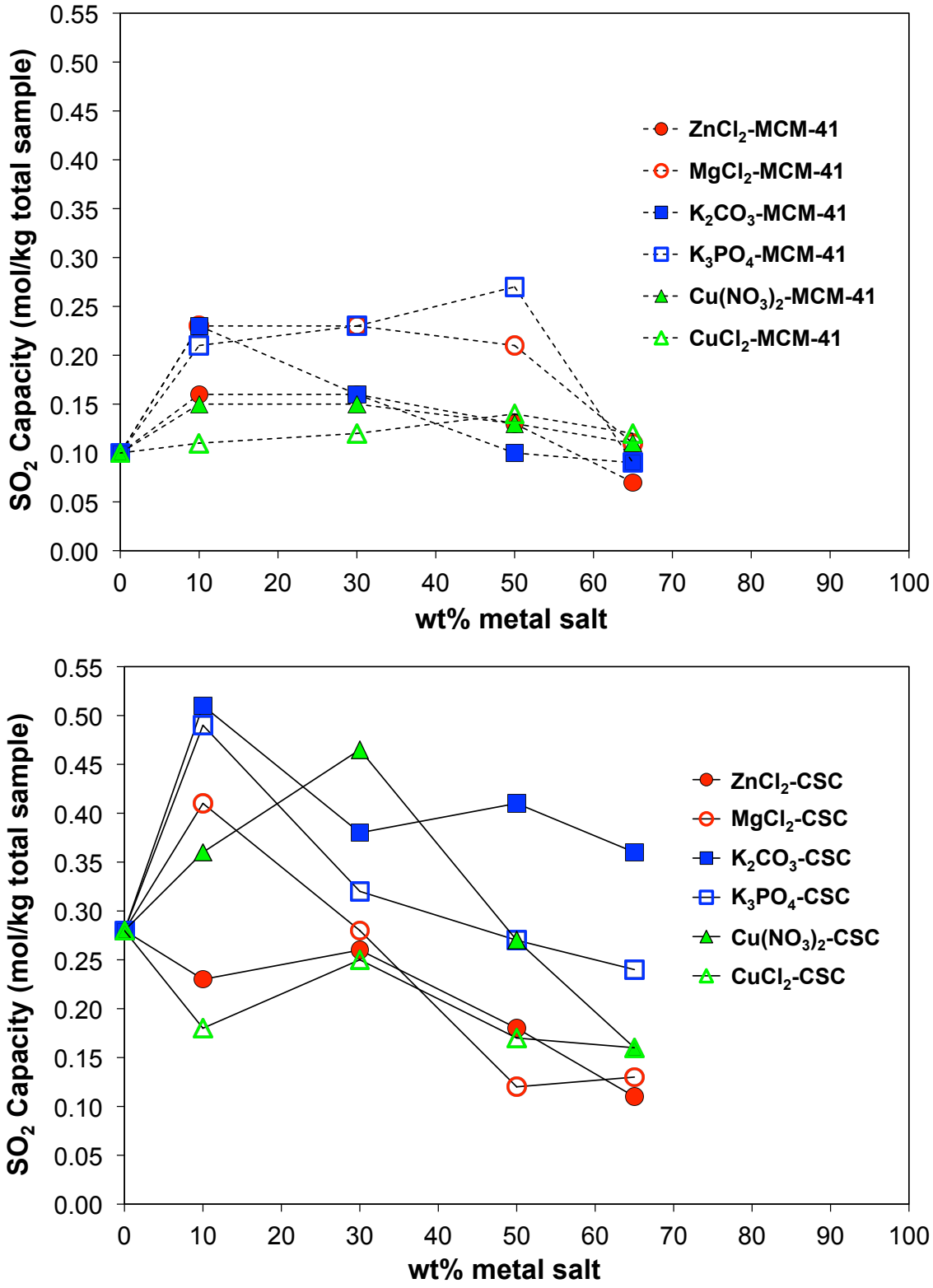

Figure 2.7. SO_2 adsorption capacity measurements for MCM-41 and CSC functionalized with select, single metal salts.

Furtado et al.,[7] the chemisorption reaction between gaseous ammonia to form a salt complex results in high capacities with $ZnCl_2$ functionalization. The displacement of nitrate ions in the aqueous solution prior to functionalization may allow for hydrated copper sites to also form ammonia-salt complexes resulting in high capacities with $Cu(NO_3)_2$ functionalization. Incorporation of potassium containing salts, K_2CO_3 and K_3PO_4, on both substrates hindered NH_3 adsorption given their high alkalinity in solution.

Among both MCM-41 and CSC functionalized materials, the incorporation of potassium salts K_2CO_3 and K_3PO_4 resulted in the highest SO_2 capacities. SO_2 capacities up to 0.23, 0.27, and 0.23 mol/kg were obtained with K_2CO_3, K_3PO_4, and $MgCl_2$ incorporation, respectively, on MCM-41 with concentrations between 10-50 wt%. SO_2 capacities up to 0.51, 0.49, and 0.47 mol/kg were obtained with K_2CO_3, K_3PO_4, and $Cu(NO_3)_2$ incorporation, respectively, on CSC with concentrations between 10-30 wt%. The increased alkalinity of the adsorbent upon the addition of potassium salts promotes interactions with acid-forming gases like SO_2. The ability of $Cu(NO_3)_2$ to displace nitrate ions in solution and form reactive copper sites promotes SO_2 adsorption. The formation of a copper sulfate complex as a result of chemisorption may justify the relatively high capacity of $Cu(NO_3)_2$-CSC for SO_2. Functionalization with $Cu(NO_3)_2$ increases SO_2 capacity on CSC much more than on MCM-41 due to the increased alkalinity of reactive copper sites in CSCs compared to MCM-41. The addition of $ZnCl_2$ and $CuCl_2$ on both substrates hindered SO_2 adsorption.

Overall, for the biphasic CSC composite material, $ZnCl_2$ is the best impregnant for boosting NH_3 adsorption with capacities as high as 5.8 mol/kg, and K_2CO_3 is the best impregnant for boosting SO_2 adsorption with capacities as high as 0.5 mol/kg. However, $ZnCl_2$-CSC shows low SO_2 adsorption capacities and K_2CO_3-CSC shows low NH_3 adsorption capacities. For the metal salt functionalized material to be effective for both target adsorbates, as determined by this work, the development of [30 wt% $Cu(NO_3)_2$]-CSC should yield an adsorbent with capacities of 4.0 and 0.45 mol/kg for NH_3 and SO_2, respectively.

Compared to the base CSC material prior to any metal salt functionalization, this is approximately a 113% increase in NH_3 adsorption and a 71% increase in SO_2 adsorption. On CSC materials, salt functionalization at a loading between 10-30 wt% is most effective at enhancing capacity measurements, whereas for MCM-41 materials, functionalization at a loading between 30-50 wt% is most effective at enhancing capacities.

2.4 Conclusions

In an effort to improve upon the gas adsorption performance of the biphasic carbon-silica composite material, further functionalization with the addition of reactive metal sites is considered. Various water-soluble metal salts are added to the CSC material as well as on MCM-41 for comparison at concentrations ranging from 10-65 wt%. As characterized by X-ray diffraction, microscopy and porosity measurements, the successful, well-dispersed incorporation of metal salts within CSCs resulted in increased microporosity and reduced surface areas while maintaining structural integrity. Optimal metal salt loading concentrations between 10-30 wt% on CSCs yielded highest adsorption capacities. For NH_3 adsorption, $ZnCl_2$-CSC is most effective with a capacity as high as 5.8 mol/kg. For SO_2 adsorption, K_2CO_3-CSC is most effective with a capacity as high as 0.51 mol/kg. In order to target both adsorbates with one material, [30 wt% $Cu(NO_3)_2$]-CSC is identified as the best compromise with NH_3 and SO_2 capacities of 4.0 and 0.45 mol/kg, respectively.

References

(1) Glover, T. G.; Dunne, K. I.; Davis, R. J.; LeVan, M. D. Carbon-Silica Composite Adsorbent: Characterization and Adsorption of Light Gases. *Microporous Mesoporous Mater.*. **2008**, *111*, 1-11.

(2) Glover, T. G.; LeVan, M. D. Carbon-Silica Composite Adsorbent: Sensitivity to Synthesis Conditions. *Microporous Mesoporous Mater.*. **2009**, *118*, 21-27.

(3) Furtado, A. M. B.; Wang, Y.; LeVan, M. D. Carbon Silica Composites for Sulfur Dioxide and Ammonia Adsorption. *Microporous Mesoporous Mater.*. **2013**, *165*, 48-54.

(4) Kresge, C. T.; Leonowicz, M. E.; Roth, W. J.; Vartuli, J. C.; Beck, J. S. Ordered Mesoporous Molecular Sieves Synthesized by a Liquid Crystal Template Mechanism. *Nature*. **1992**, *359*, 710-712.

(5) Beck, J. S.; Vartuli, J. C.; Roth, W. J.; Leonowicz, M. E.; Kresge, C. T.; Schmitt, K. D.; Chu, C. T.-W.; Olson, D. H.; Sheppard, E. W.; McCullen, S. B.; Higgins, J. B.; Schlenker, J. L. A New Family of Mesoporous Molecular Sieves Prepared with Liquid Crystal Templates. *J. Am. Chem. Soc.*. **1992**, *14*, 10834-10843.

(6) Oye, G.; Glomm, W. R.; Vralstad, T.; Volden, S.; Magnusson, H.; Stocker, M.; Sjoblom, J. Synthesis, Functionalisation and Characterisation of Mesoporous Materials and Sol-Gel Glasses for Applications in Catalysis, Adsorption and Photonics. *Adv. Colloid Interface Sci.*. **2006**, *123*, 17-32.

(7) Furtado, A. M. B.; Wang, Y.; Glover, T. G.; LeVan, M. D. MCM-41 Impregnated with Active Metal Sites: Synthesis, Characterization and Ammonia Adsorption. *Microporous Mesoporous Mater.*. **2011**, *142*, 730-739.

(8) Burket, C. L.; Rajagopalan, R.; Marencic, A. P.; Dronvajjala, K.; Foley, H. C. Genesis

of Porosity in Polyfurfuryl Alcohol Derived Nanoporous Carbon. *Carbon.* **2006**, *44*, 2957-2963.

(9) McNamara, K. W.; Ayyappan, P.; Rajagopalan, R.; Chen, J. G.; Foley, H. C. Localized Crystallization of Polyfurfuryl Alcohol Derived Carbon by Alkali Metals. *Carbon.* **2013**, *56*, 109-120.

(10) Fortier, H.; Zelenietz, C.; Dahn, T. R.; Westreich, P.; Stevens, D. A.; Dahn, J. R. SO_2 Adsorption Capacity of K_2CO_3-Impregnated Activated Carbon as a Function of K_2CO_3 Content Loaded by Soaking and Incipient Wetness. *Appl. Surf. Sci.*. **2007**, *253*, 3201-3207.

(11) Fortier, H.; Westreich, P.; Selig, S.; Zelenietz, C.; Dahn, J. R. Ammonia, Cyclohexane, Nitrogen and Water Adsorption Capacities of an Activated Carbon Impregnated with Increasing Amounts of $ZnCl_2$, and Designed to Chemisorb Gaseous NH_3 from an Air Stream. *J. Colloid Interface Sci.*. **2008**, *320*, 423-435.

(12) Janus, R.; Wach, A.; Kustrowski, P.; Dudek, B.; Drozdek, M.; Silvestre-Albero, A. M.; Rodríguez-Reinoso, F.; Cool, P. Investigation on the Low-Temperature Transformations of Poly(furfuryl alcohol) Deposited on MCM-41. *Langmuir.* **2013**, *29*, 3045-3053.

CHAPTER III

IN-PORE SYNTHESIS OF $ZnCO_3$ IN CARBON SILICA COMPOSITES, MCM-41, ACTIVATED CARBONS, AND SILICA GEL FOR NH_3 AND SO_2 ADSORPTION

3.1 Introduction

Many functionalities can be useful for the chemisorption of TICs, though not all may be water soluble to allow easy impregnation. By chemically adsorbing TICs, such functionalized adsorbents are meant to be expended for potential high performance, one-pass, non-regenerable filtration applications. Given their low solubility, coarse distributions of water-insoluble functionalities can limit their effectiveness on the substrate. A novel impregnation method to incorporate these reactive, water-insoluble functionalities in a more dispersed manner is desirable.

Metal salts have been shown to provide the potential for various chemical reactions with TICs. Their incorporation in porous adsorbents to enhance adsorption capacities is well-studied. Previous works have shown that impregnated salts can act as isolated reactive sites.[1–9] When well dispersed, these salts can supplement traditional adsorption sites and boost capacity measurements. Many water soluble metal salt functionalities have been added to adsorbents such as activated carbon or mesoporous silica. Among the salts tested, $ZnCl_2$ and K_2CO_3 have been identified as most effective against TICs such as NH_3 and SO_2, respectively.[1–5] The high performance of these functionalities have been attributed to chemisorption. Ammonia reacts with $ZnCl_2$ to form a $Zn(NH_3)_2Cl_2$ complex,[2] while sulfur dioxide reacts with K_2CO_3 to liberate CO_2 and form $KHSO_3$ in the presence of adsorbed H_2O.[1] In previous work, concentration dependence of these salts showed that approximately 10 wt% of $ZnCl_2$ on a biphasic adsorbent increased NH_3 capacity by 190%, while 10 wt% of K_2CO_3 on the adsorbent increased SO_2 capacity by 85%.[4,5]

The purpose of this paper is to add an insoluble, reactive metal salt functionality to porous adsorbent substrates such that the affinity for both basic and acid-forming gases is greatly enhanced. This contribution follows directly from our previous work[5] in which single, soluble, metal salts were added to a mesoporous silica and a biphasic adsorbent. The adsorbents used as substrates for this work will also include the biphasic adsorbent and mesoporous silica MCM-41, along with commercially purchased silica gel, BPL activated carbon and Norit SX Ultra activated carbon. Activated carbon has traditionally been commercialized for use in filtration applications for air purification. Such carbons have large pore size distributions containing macropores and mesopores for efficient gas transport as well as micropores for physisorption due to strong well potential. Among the activated carbons used here, BPL is a bituminous coal-based product available for purchase from Calgon Carbon, while Norit SX Ultra derived from peat, a partially carbonized phytomass, available for purchase from Cabot Corporation. Silica gel is a commercially available, porous, granular form of silica synthesized from sodium silicate containing pores larger than 2 nm in size.[12] MCM-41 is a mesoporous silica belonging to the M41s family of materials developed by Kresge et al.[13] of the Mobile Oil Corporation. It contains ordered, hexagonal pores 3-4 nm wide, though tunable in size based on the length of the surfactant chain used during synthesis. The free surface hydroxyl groups lining the pore surfaces and pore walls serve as useful sites of adsorption especially for interactions with polar gases such as NH_3. The biphasic, microporous carbon silica composite (CSC) material, developed recently by our group,[5,14–16] takes advantage of both the polar silica (consisting of MCM-41) and nonpolar carbon phases to target a wide spectrum of adsorbates. Further functionalization with additional reactive moieties using such substrates should enhance the broad scale applicability of the adsorbent material.

When added individually to the porous material, both $ZnCl_2$ and K_2CO_3 are well dispersed. By adding them sequentially on the same material, the dispersion is maintained,

and where interactions between the two are possible, a well known reaction occurs to form a solid precipitate of $ZnCO_3$ within the pores of the adsorbent. This incorporation of a well dispersed, insoluble moiety involves dual salt functionalization with two water soluble precursors. To the best of our knowledge, this in-pore synthesis method to functionalize porous materials, specifically with insoluble metal salts has not been previously examined.

Albeit, a few examples of in-pore synthesis to achieve effective incorporation do exist in the literature; however, they concern much different applications. In one study, Froba et al.[17] synthesized iron (III) oxide nanoparticles within the mesoporous carbon CMK-1 via in-pore synthesis. During this synthesis, iron nitrate was impregnated into the carbon and calcined post impregnation in order to form iron (III) oxide within the pores of the substate. In another study, Froba et al.[18] synthesized Au_{55} clusters within the mesopores of SBA-15 via in-pore synthesis. During this procedure, the two derivates used to make the gold clusters were added simultaneously with the substrate to achieve reaction within pores rather than adding the pre-synthesized cluster to the substrate after reaction. In both cases of in-pore synthesis, a greater level of dispersion of the functionalities was achieved. In contrast, in the case of $ZnCO_3$ functionalization, since the metal salt itself is insoluble in water, a reaction to form the functionality using two soluble metal salt precursors is meant to avoid agglomeration on the porous substrate, which would occur with an insoluble salt.

In this work, single phase silica materials, single phase carbon materials, and a biphasic carbon silica composite are incorporated with reactive $ZnCO_3$ in order to enhance the ammonia and sulfur dioxide adsorption capacities. Given the insolubility of the $ZnCO_3$, the incorporation of this salt is varied either by adding a commercially purchased sample onto the substrate or by forming the $ZnCO_3$ within the pores of the substrate via in-pore synthesis using two water-soluble precursors. The performance of these functionalized composites are measured using full equilibrium breakthrough adsorption capacities for low concentrations of NH_3 and SO_2 gases. The synthesized materials are characterized using X-ray diffraction,

porosimetry, and microscopy techniques to provide evidence of the incorporation as well as an understanding of the effects of functionalization.

3.2 Experimental Methods

Materials

Tetraethyl orthosilicate (TEOS) was purchased from Sigma Aldrich. Hexadecyltrimethylammonium chloride (CTAC, 25% in water) was purchased from Pfaltz and Bauer. A solution of ammonium hydroxide (29 wt.% in water) and Cab-O-Sil M5 were purchased from Fisher Scientific. Furfuryl alcohol (99%) and toluene (99%) were purchased from Sigma Aldrich. Anhydrous salts zinc chloride ($ZnCl_2$), potassium carbonate (K_2CO_3), and zinc carbonate ($ZnCO_3$) were purchased from Sigma Aldrich. Norit SX Ultra activated carbon with a surface area of $\sim$1100 m^2/g and a pore volume of $\sim$0.8 cm^3/g was purchased from Cabot Corporation. BPL activated carbon with a surface area of $\sim$1000 m^2/g and a pore volume of $\sim$0.5 cm^3/g was purchased from Calgon Carbon. Silica gel with a surface area of $\sim$500 m^2/g and a pore volume of $\sim$0.8 cm^3/g was purchased from Sigma Aldrich. Gas cylinders of 1500 ppmv ammonia in helium, 500 ppmv sulfur dioxide in helium, and ultrahigh purity helium were purchased from A-L Compressed Gas.

Synthesis Procedures

The synthesis procedures of the substrates MCM-41 and CSC have been thoroughly described previously.[5] Briefly, the MCM-41 is synthesized by the incorporation of surfactant molecules into a polar solution which form a liquid crystal of rod shaped micelles. Fumed silica is cast around the hexagonal array of micelles, after which the surfactants are burned off via calcination at high temperatures to leave behind the mesoporous, honeycomb framework of MCM-41. The synthesis of CSC involves the addition of pre-synthesized, MCM-41 to a solution containing furfuryl alcohol in a toluene solvent. The alcohol polymerizes readily

at room temperature and condenses within the silica matrix. Upon carbonization at high temperatures in the absence of oxygen, the microporous carbon silica composite is obtained. Confirmed via thermogravimetric analysis, approximately 25 wt% of the composite structure consists of carbonaceous material and the remainder corresponds to the siliceous phase.

In-Pore Synthesis of $ZnCO_3$

The formation of $ZnCO_3$ in the various substrates involves sequential dual salt functionalization leading to in-pore synthesis. Briefly, in implementing the incipient wetness approach, approximately 260 μL of an aqueous solution, formed by mixing 1 g of K_2CO_3 in 10 mL of water, was first dribbled onto 200 mg of porous material until wet and allowed to dry. After removal of water through evaporation approximately 25 mg of K_2CO_3 remained within the material. Upon drying, approximately 260 μL of another aqueous solution, formed by mixing 1 g of $ZnCl_2$ in 10 mL of water, was dribbled onto the dried, K_2CO_3-containing adsorbent. After removal of water through evaporation approximately 25 mg of $ZnCl_2$ was now also present in the material. Theoretically, with 25 mg of each impregnant loaded on 200 mg of adsorbent material, approximately 10 wt% (on a total sample basis) of both $ZnCl_2$ and K_2CO_3 were present on the substrate. The similarity in the quantities of impregnant solutions added to the adsorbent was due to very similar molecular weights and solution densities of both salts. During the addition of $ZnCl_2$, a stoichiometrically balanced reaction occurs between free zinc ions and carbonate anions in solution leading to the synthesis of $ZnCO_3$. If all quantities of the two impregnated salts are expected to react, approximately 9 wt% of the total sample would be comprised of $ZnCO_3$. These lower concentrations of salt impregnants were chosen based on previous work,[5] which showed that optimal salt loadings on CSC were between 10-30 wt% while on MCM-41, they were between 30-50 wt%.

For dual functionalization, the order in which the two impregnants were added to form $ZnCO_3$ was specifically chosen based on results with MCM-41. In prior experiments where $ZnCl_2$ was added first, followed by K_2CO_3, $ZnCO_3$ still formed within pores; however, the

adsorption capacities for this functionalized material were lower. It is possible that the reactive and basic siliceous phase of MCM-41, also present in the CSC, may participate in electrostatic interactions with the $ZnCl_2$, which can behave as a Lewis acid. In contrast, the K_2CO_3 is basic in aqueous solution, which may sustain its reactivity within the basic substrate when added first during the dual functionalization. For this reason, the in-pore synthesis reaction to form $ZnCO_3$ within the pores of each of the substrates tested begins first with K_2CO_3 functionalization followed by $ZnCl_2$ functionalization. This dual salt functionalization to form $ZnCO_3$ via in-pore synthesis was also performed in other substrates for comparison including MCM-41, silica gel, BPL activated carbon, and a Norit carbon.

Water Washing of Dual-Functionalized Materials

The dual functionalized substrates were washed with water in order to remove any free, soluble, unreacted ions within the composite. Consequently, this resulted in only insoluble $ZnCO_3$ formed via in-pore synthesis. In this procedure, the dual functionalized substrates were placed on filter paper and approximately 50 mL of H_2O were poured onto the sample while filtering under vacuum. Once the sample was completely dried, another 50 mL of H_2O were poured onto the sample while filtering under vacuum. This was repeated three more times for a total of five wash steps and the dried sample was collected for characterization.

Wet Impregnation with $ZnCO_3$

For comparison with in-pore synthesis, approximately 22 mg of commercially purchased $ZnCO_3$, corresponding to 10 wt%, was added to 200 mg of the substrate via a wet impregnation method. In this procedure, the $ZnCO_3$ and the corresponding substrate were mixed together and stirred for several hours to allow the salt to disperse on the adsorbent. After removal of water through evaporation, the commercially purchased $ZnCO_3$ was incorporated with the substrate at an amount analogous to the concentration of $ZnCO_3$ that is expected to form via the in-pore synthesis method.

Materials Characterization

Prior to any characterization, synthesized materials were placed in a vacuum oven at 60°C for approximately two hours to remove any adsorbed water.

Porosimetry

For textural characterization, adsorption isotherms were measured using a Micromeritics ASAP 2020 at -196 °C with nitrogen as the analysis gas. Before analysis, approximately 0.1 g of each sample was degassed under vacuum (20 mmHg) and heated to 120 °C. The BET method was used to determine surface areas. The reported pore volumes, calculated using density functional theory, correspond to $P/P_0 \cong 0.99$. Given the microporous nature of CSC and the extensive amount of time that would be required for extremely low pressures of nitrogen to equilibrate within the adsorbent, the pore size distribution between 0 to 1 nm could not be obtained. Instead, the pore size distribution for pores larger than 1 nm were reported.

X-ray Diffraction

Powder X-ray diffraction patterns were used to confirm the long-range structure of the base composite material made from mesoporous silica. These patterns were obtained using a Scintag X1h/h automated powder diffractometer with Cu target, a Peltier-cooled solid-state detector, a zero background Si(5 1 0) support, and a copper X-ray tube as the radiation source.

Microscopy

Electron microscopy measurements were performed using the FEI Tecnai Osiris operating at 200 kV. Transmission electron microscopy (TEM) was used to obtain high resolution images of the mesoporous and microporous structures of functionalized MCM-41 and CSC

materials. Scanning transmission electron microscopy (STEM) coupled with energy dispersive X-ray (EDX) signal detection provided color-coded, mapped images of specific elements of interest and after using the appropriate software, also provided quantitative analysis of each element in a scanned region of the sample. Samples were prepared by adding small quantities (∼10 mg) of adsorbent to approximately 5 mL of H_2O. The dispersion was then placed onto a lacey carbon TEM grid and allowed to air dry before analysis using the microscope. Since carbon was present in both the TEM grid and the CSC, to avoid misinterpretation of the carbon content of the impregnants, the functionalized MCM-41 was used to interpret the dispersion of the impregnants as well as the effects on elemental composition after washing using quantitative analysis with STEM-EDX.

Adsorption Capacity

NH_3 and SO_2 have been used as target adsorbates in this study because they represent opposite ends of a spectrum of potential, light gas TICs. Sulfur dioxide is acid-forming and an oxidizer, while ammonia is basic and a reducer. As a primary measure of performance, adsorption capacities for our synthesized, functionalized adsorbent materials were tested at low concentrations of both NH_3 and SO_2. These capacities were calculated from room temperature gas adsorption of NH_3 and SO_2 on all synthesized materials using breakthrough measurements. These measurements were performed using a breakthrough apparatus, a schematic of which is shown elsewhere.[4] With accumulation of target adsorbate in the gas phase being negligible relative to that in the adsorbed phase, the capacity of the adsorbent material, n (mol adsorbate/kg adsorbent), was calculated from

$$n = \frac{F}{m} \int_0^\infty (C_0 - C)\, dt \tag{2}$$

where C_0 is the feed concentration in units of mol/m^3, and C is the effluent concentration

at time t. The volumetric flow rate of gas through the adsorbent bed, F, was held constant at 30 sccm. The mass of the sample, m, varied between 15-30 mg and was contained in a small cylindrical adsorbent bed with an internal diameter of 4 mm.

The standard deviations in adsorption capacities that is representative of differences between measurements on the same sample is approximately 6% and 3% for NH_3 and SO_2, respectively. These were calculated from several measurements of NH_3 and SO_2 capacities on MCM-41 synthesized from the same batch. For many of the synthesized adsorbents in this study, in order to confirm reproducibility, the materials were re-synthesized (multiple batches). This implies that deviations in capacity measurements for the same material are due to not only the standard deviation from measurement to measurement but also differences in batch-to-batch synthesis of the same material. Overall, the error in NH_3 and SO_2 capacities reported, calculated using capacity measurements of MCM-41 synthesized in three separate batches, was approximately $\pm$12% and $\pm$9%, respectively.

3.3 Results and Discussion

To appropriately understand the effects of in-pore synthesis, representative materials were analyzed using X-ray diffraction, porosity, and microscopy techniques. These adsorbents include (1) MCM-41, (2) K_2CO_3-$ZnCl_2$-MCM-41, (3) Washed-K_2CO_3-$ZnCl_2$-MCM-41, (4) $ZnCO_3$-MCM-41, (5) CSC, (6) K_2CO_3-$ZnCl_2$-CSC, (7) Washed-K_2CO_3-$ZnCl_2$-CSC, and (8) $ZnCO_3$-CSC.

Porosimetry

Nitrogen adsorption isotherms for the selected materials are shown in Figure 3.1a and 3.1b. Upon $ZnCO_3$ functionalization on MCM-41, isotherms showed less Type IV behavior and more Type I behavior. Upon $ZnCO_3$ functionalization on CSC, isotherms maintained Type I behavior. The quantity of nitrogen adsorbed on functionalized materials decreased

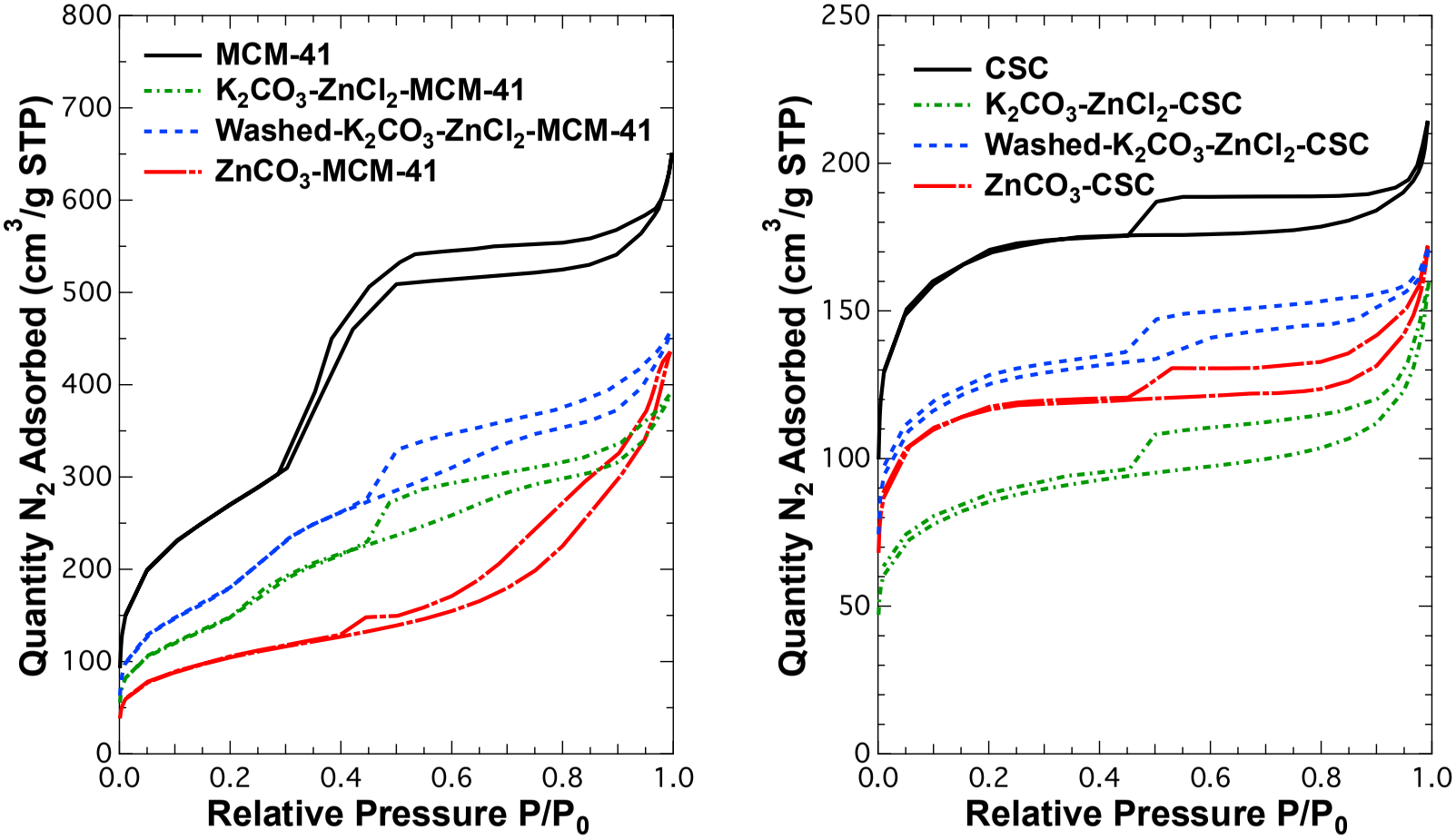

Figure 3.1. N_2 adsorption isotherms of washed and unwashed, in-pore synthesized $ZnCO_3$ compared with solution-impregnated $ZnCO_3$ on (a) MCM-41 and (b) CSC.

significantly compared to the non-impregnated substrates. This indicates the inability of nitrogen to access traditional surface adsorption sites due to pore blockage or pore filling. Washed materials showed an increase in the quantity of nitrogen adsorbed. This can be attributed to the liberation of nitrogen adsorption sites after washing away soluble, unreacted ions from the adsorbent. Crude incorporation of commercially purchased $ZnCO_3$ on MCM-41 resulted in lower quantities of adsorbed nitrogen as well as a shift to Type II isotherm behavior representative of non-porous materials due to salt aggregation and pore blockage. On CSC, incorporation of commercially purchased $ZnCO_3$ maintained Type I isotherm shape and showed a lower quantity of adsorbed nitrogen as compared to CSC but higher than that of in-pore synthesized $ZnCO_3$. Hysteresis loops occurred in all isotherms, which is evidence of capillary condensation in the mesopores of every sample.

Pore size distributions for the same materials are shown in Figure 3.2a and 3.2b. As a result of salt incorporation, pore size distributions show wider peaks with less uniformity. In-pore synthesis on MCM-41 resulted in the separation of the characteristic peak between 3-4 nm into two wider peaks with reduced intensities centered around 3 nm and 5 nm. In pore synthesis on CSC resulted in the dampening of peak intensities, but characteristic peaks of CSC were maintained. Crude incorporation of commercially purchased $ZnCO_3$ on both MCM-41 and CSC show a reduced distribution at smaller pore widths and new, broader peaks at larger pore sizes. Water washing on MCM-41 showed minimal shift of the distribution to larger pore volumes compared with water washing on CSC, which showed a significant, new peak in the mesoporous regime of the pore size distribution. Overall, in-pore synthesis of $ZnCO_3$ reduced pore size distributions and produced wider, less uniform peaks generally maintained in the micropore regime, while crude incorporation of commercially purchased $ZnCO_3$ produced a broad distribution centered around larger pores.

Adsorption isotherms also allow a quantitative analysis of textural characterization via surface area and pore volume calculations as shown in Table 3.1. Surface area measure-

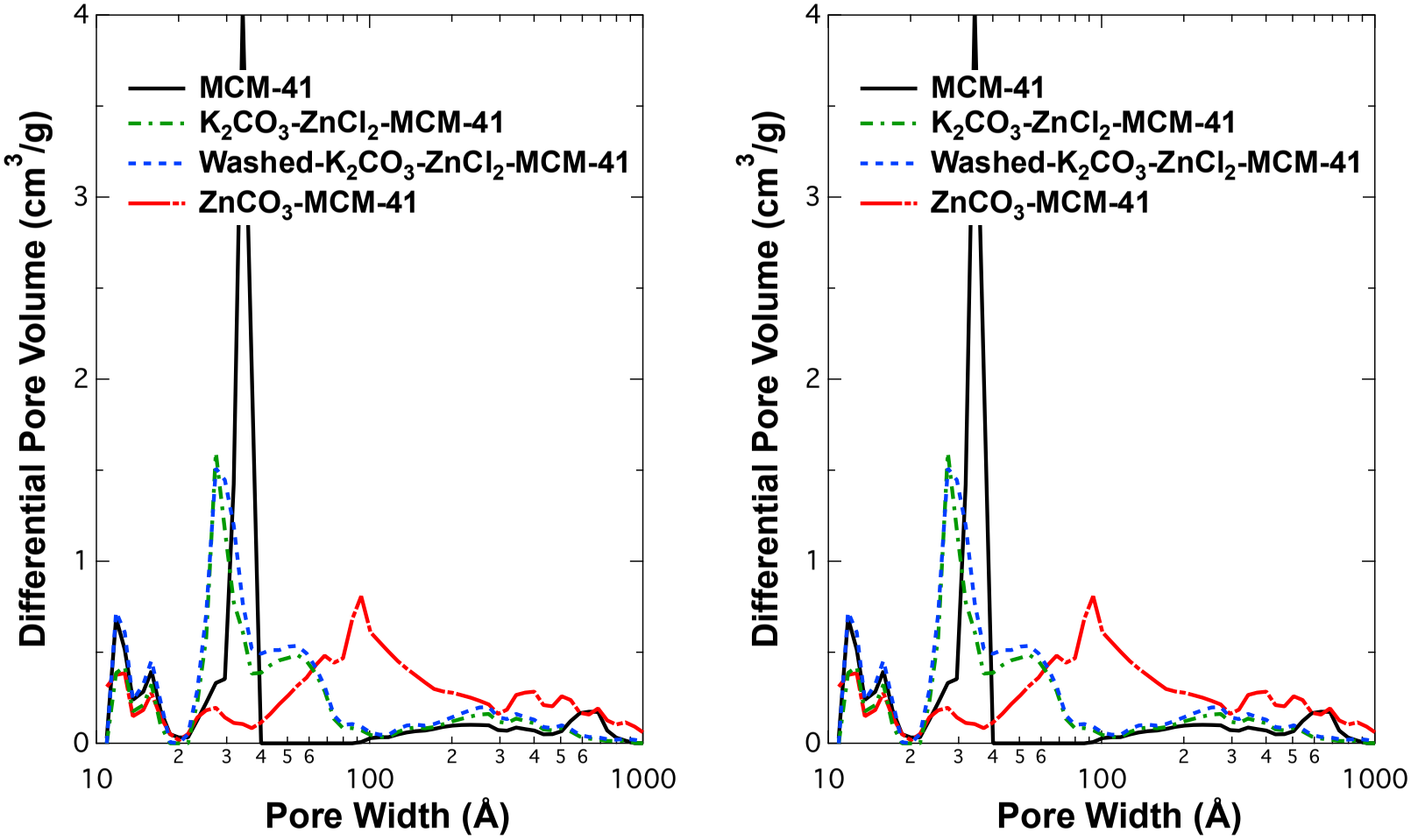

Figure 3.2. Pore size distributions of washed and unwashed, in-pore synthesized $ZnCO_3$ compared with solution-impregnated $ZnCO_3$ on (a) MCM-41 and (b) CSC.

Table 3.1. BET surface area and pore volumes of washed and unwashed, in-pore synthesized $ZnCO_3$ compared with solution-impregnated $ZnCO_3$ on MCM-41 and CSC.

Sample	Name	Surface Area (m^2/g)	Pore Volumes			
			Total (cm^3/g)	Micropore (cm^3/g)	Mesopore (cm^3/g)	Macropore (cm^3/g)
1	MCM-41	950	1.00	0.17	0.72	0.11
2	K_2CO_3-$ZnCl_2$-MCM-41	570	0.61	0.08	0.52	0.01
3	W-K_2CO_3-$ZnCl_2$-MCM-41	680	0.71	0.11	0.58	0.02
4	$ZnCO_3$-MCM-41	360	0.67	0.08	0.52	0.07
5	CSC	560	0.33	0.20	0.09	0.04
6	K_2CO_3-$ZnCl_2$-CSC	290	0.25	0.09	0.11	0.05
7	W-K_2CO_3-$ZnCl_2$-CSC	410	0.27	0.13	0.11	0.03
8	$ZnCO_3$-CSC	400	0.27	0.11	0.10	0.06

ments directly correlated to the quantity of nitrogen adsorbed, where decreasing adsorbed nitrogen amounts were consistent with decreases in surface area for functionalized materials. Upon further functionalization with a precipitate formed via in-pore synthesis or crude incorporation of commercially purchased $ZnCO_3$, the BET surface area decreases compared to non-functionalized MCM-41 or CSC. It should be noted that differences in the substrates affected the surface areas of functionalized materials when comparing the two methods of functionalization. The in-pore synthesis of $ZnCO_3$ on CSC reduced the surface area more than crude impregnation of $ZnCO_3$ on CSC. The opposite is observed on MCM-41 where crude impregnation of $ZnCO_3$ on MCM-41 reduced the surface area more than in-pore synthesis of $ZnCO_3$ on MCM-41. Pore volumes also decreased upon salt functionalization, as should be expected. Pore size distributions provided a measure of pore volumes at different pore regimes. Total pore volumes split into their respective micropore, mesopore, and macropore volumes are also shown in Table 3.1. On MCM-41, salt incorporation (both methods) reduced pore volumes in all regimes. On CSC, in-pore synthesis reduced micropore and mesopore volumes only. However, crude, wet impregnation on CSC reduced only micropore volume and instead showed slight increase in mesopore and macropore volumes. This can be attributed to the already microporous nature of the composite. Well dispersed functionalities can be incorporated into the micropores of the composite but agglomeration largely affects macropores. After washing in-pore synthesized $ZnCO_3$ materials with water, the pore volumes increased slightly due to the removal of soluble, unreacted potassium and chlorine ions.

X-ray Diffraction

XRD patterns shown in Figure 3.3 were analyzed to confirm the ordered structural integrity of the synthesized adsorbents. Results for the selected functionalized materials revealed evidence of characteristic peaks similar to MCM-41. The apparent diminishing order of the silica phase in functionalized materials is likely due to interference from the

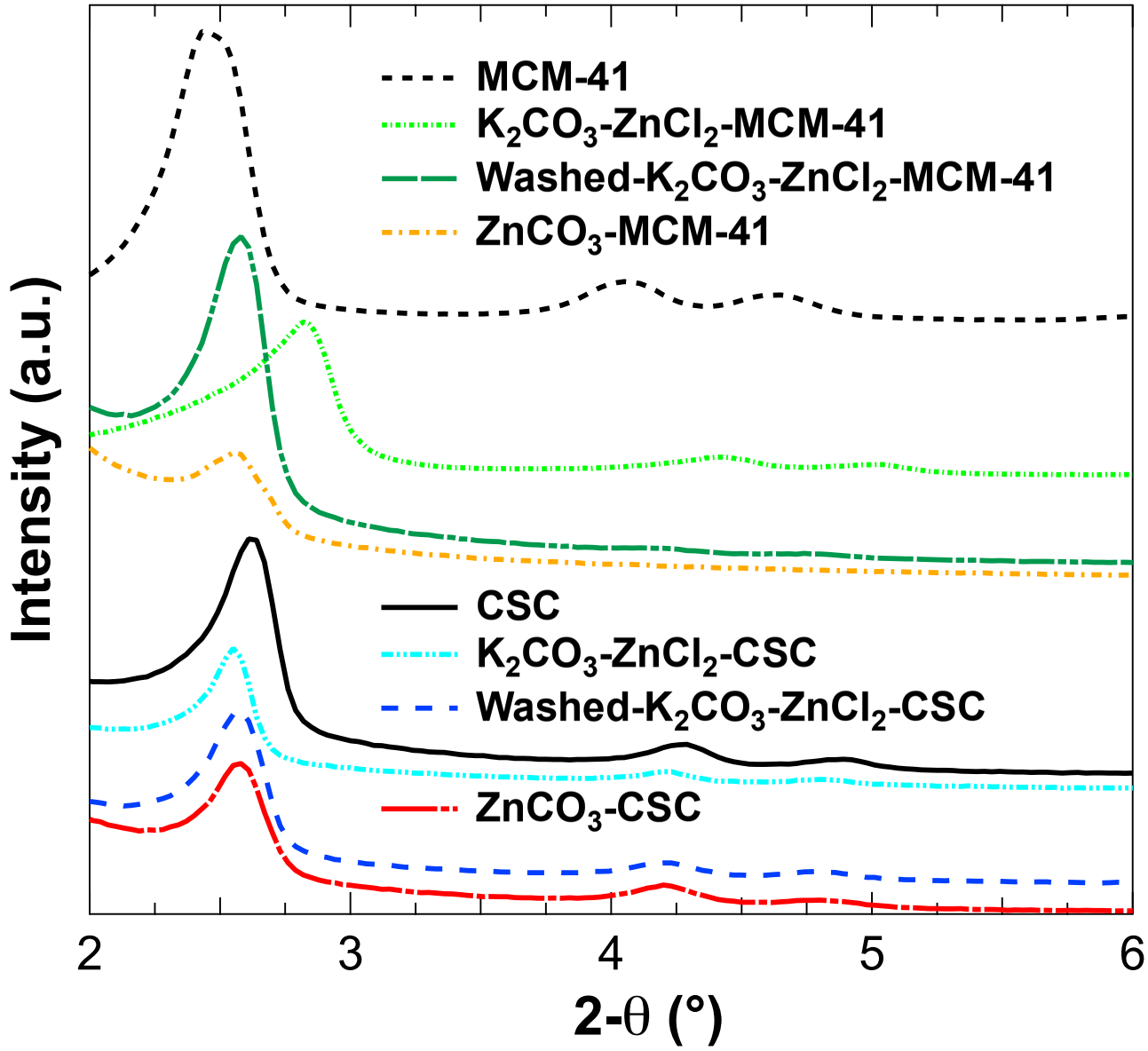

Figure 3.3. XRD patterns of washed and unwashed, in-pore synthesized $ZnCO_3$ compared with solution-impregnated $ZnCO_3$ on MCM-41 and CSC.

incorporated state rather than reduced "crystallinity". The shift of all peaks to increased diffraction angles as compared to MCM-41 corresponds to smaller distances between pore centers, which is likely due to reduced pore sizes after salt incorporation seemingly representative of a shrinking pore structure.

Microscopy

TEM images of some of the selected functionalized materials are shown in Figure 3.4. All samples showed evidence of mesopores from the MCM-41 contribution. The porosity of each synthesized adsorbent was evident in these images through axial and radial planes (in cylindrical geometry), as seen by parallel lines and/or honeycomb-shaped matrix. To confirm the well-mixed dispersion of metal salt impregnants, STEM-EDX images of sample 3 shown in Figure 3.5 provided spatial resolution of each element present in the sample. Porosity was further shown in STEM-EDX images of silicon and oxygen atoms that make up the base material. Although the potassium and chlorine micrographs appeared to show evidence of these atoms in the structure even after washing with water, the very poor resolution of these scans suggests that this amount is consistent with error in precision in the software that distinguishes the elemental difference between atoms. Results confirmed that successful incorporation of both K_2CO_3 and $ZnCl_2$ was achieved since the zinc and carbon atoms lined the pores of the adsorbent throughout the material rather than agglomerated in a specific part of the sample.

Any evidence to suggest the formation of $ZnCO_3$ was analyzed using STEM-EDX, which also provided elemental composition of a specified region of the sample. As reported in Table 3.2, more than ten STEM-EDX scans of ten unique regions on Samples 2, 3, and 4 were analyzed to determine their elemental compositions within error. Comparing the compositions of Samples 2 and 3 showed that washing the in-pore synthesized material with water released the soluble, unreacted chlorine and potassium ions, reducing their composition

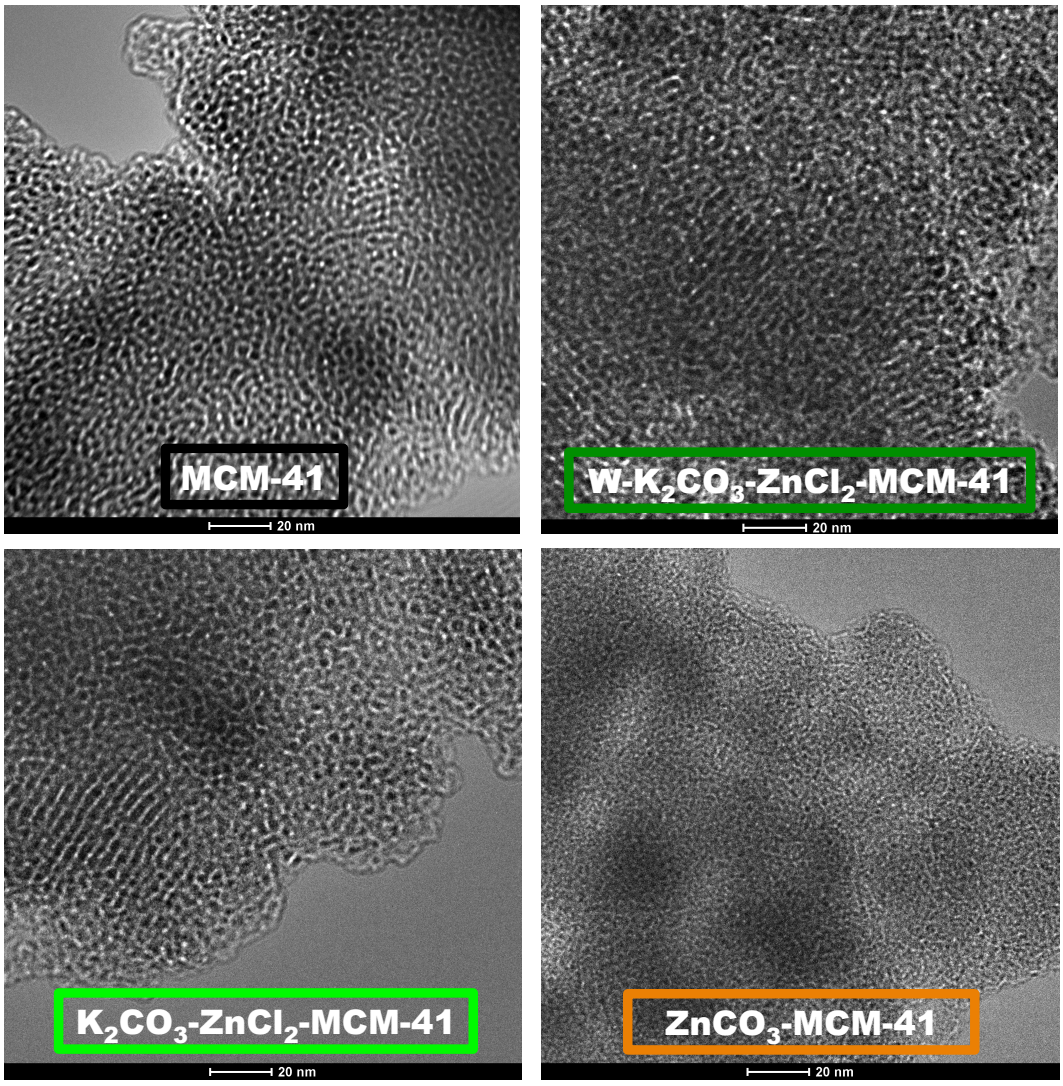

Figure 3.4. TEM images of washed and unwashed, in-pore synthesized $ZnCO_3$ compared with solution-impregnated $ZnCO_3$ on MCM-41.

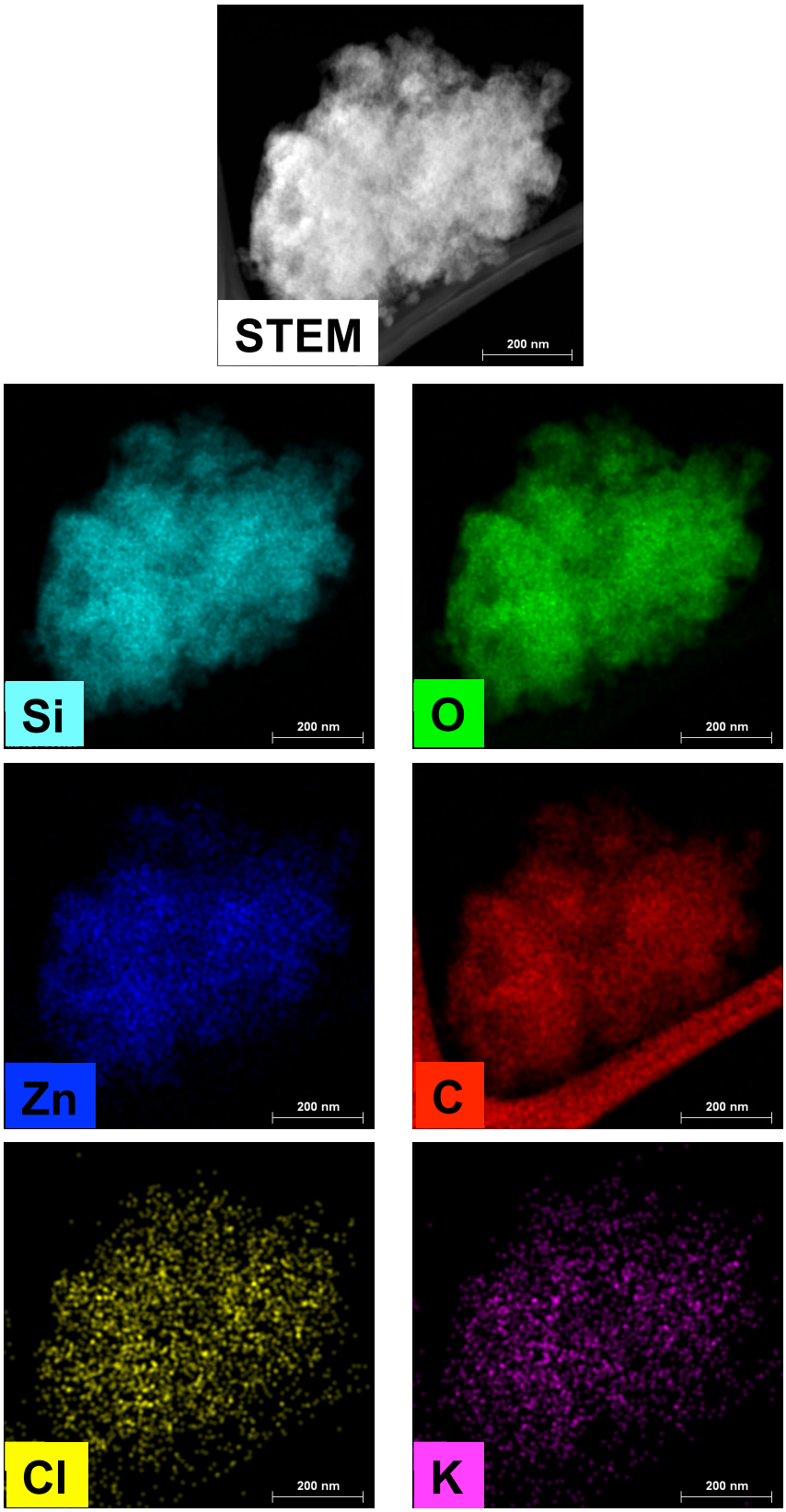

Figure 3.5. STEM images for washed, in-pore synthesized $ZnCO_3$ on MCM-41.

Table 3.2 Elemental compositions of washed and unwashed, in-pore synthesized $ZnCO_3$ compared with solution-impregnated $ZnCO_3$ on MCM-41 and CSC.

Sample	Name	Elemental Composition (Weight %)					
		Si	O	C	Zn	Cl	K
2	K_2CO_3-$ZnCl_2$-MCM-41	44 ± 2	42 ± 2	9 ± 4	3.1 ± 1.5	1.6 ± 1.0	1.3 ± 0.5
3	W-K_2CO_3-$ZnCl_2$-MCM-41	48 ± 1	45 ± 1	5 ± 2	2.5 ± 1.0	0.0 ± 0.0	0.2 ± 0.1
4	$ZnCO_3$-MCM-41	32 ± 16	35 ± 7	13 ± 7	20 ± 18	0.0 ± 0.0	0.0 ± 0.0

to 0 wt%. The release of chlorine after water washing was further confirmed by analysis of the effluent solution developed during filtration. An aqueous, clear solution containing soluble silver nitrate was slowly added dropwise to this effluent solution containing washed chlorine ions. Upon the addition of silver nitrate, a reaction with chlorine ions to yield an insoluble, cloudy silver chloride precipitate was evident. This experiment to confirm the presence of chlorine ions was also tested on the effluent solution generated from washing Sample 6 with water to yield Sample 7. The presence of zinc and carbon compositions in Sample 3 even after washing implies that they have become water-insoluble given their persistence on the support, which is possible by forming a $ZnCO_3$ precipitate on the material. Since some quantities of the two soluble precursors do not react together and instead remain isolated on the adsorbents, washing these unreacted salts results in the removal of some K_2CO_3 and $ZnCl_2$ shown by the slight reduction in zinc and carbon compositions of Sample 3. A comparison of the error in zinc and carbon compositions between Samples 3 and 4 clearly distinguished the differences in dispersion between synthesis with two soluble precursors versus incorporation of a pre-synthesized, commercially available $ZnCO_3$. There was significant error in compositions of Sample 4, which corresponds to the poor dispersion of commercially purchased $ZnCO_3$ on MCM-41 such that the STEM-EDX scan either hit a silica phase or a $ZnCO_3$ phase but not both, as it did more reasonably with in-pore synthesis.

Adsorption Capacity

The NH_3 and SO_2 adsorption capacities of the selected materials are shown in Table 3.3. The capacities shown represent an average of multiple measurements. $ZnCO_3$ functionalization on CSCs was compared with $ZnCO_3$ functionalization on MCM-41. On both substrates, the incorporation of $ZnCO_3$ increased NH_3 and SO_2 capacities, regardless of the impregnation method. Compared to MCM-41, sample 2 had a capacity of 3.6 mol/kg for NH_3 and a capacity of 0.41 mol/kg for SO_2, a 57% and 310% increase, respectively. Similarly,

Table 3.3. NH_3 and SO_2 capacities of washed and unwashed, in-pore synthesized $ZnCO_3$ compared with solution-impregnated $ZnCO_3$ on MCM-41 and CSC.

Sample	Name	Adsorption Capacities	
		NH_3	SO_2
		(mol/kg)	(mol/kg)
1	MCM-41	2.3	0.10
2	K_2CO_3-$ZnCl_2$-MCM-41	3.6	0.41
3	W-K_2CO_3-$ZnCl_2$-MCM-41	3.8	0.48
4	$ZnCO_3$-MCM-41	3.4	0.44
5	CSC	2.1	0.32
6	K_2CO_3-$ZnCl_2$-CSC	4.2	0.59
7	W-K_2CO_3-$ZnCl_2$-CSC	2.7	0.56
8	$ZnCO_3$-CSC	3.1	0.44

sample 4 had a capacity of 3.4 mol/kg for NH_3 and a capacity of 0.44 mol/kg for SO_2, a 48% and 340% increase, respectively. Compared to CSC, sample 6 had a capacity of 4.2 mol/kg for NH_3 and a capacity of 0.59 mol/kg for SO_2, a 100% and 84% increase, respectively. Similarly, sample 8 had a capacity of 3.1 mol/kg for NH_3 and a capacity of 0.44 mol/kg for SO_2, a 48% and 38% increase, respectively. These increases in capacities were attributed to the addition of reactive metal salt(s) added to the substrates which promote chemisorption of both NH_3 and SO_2. The comparisons between samples 2 and 6 with 1 and 5, respectively, shows that in-pore synthesis of $ZnCO_3$ improved NH_3 adsorption on CSC more than on MCM-41, while the improvement in SO_2 adsorption was more significant on MCM-41 than on CSC. The presence of a basic carbon phase enhances SO_2 capacities, while the incorporation of reactive $ZnCO_3$ sites in narrower pore sizes helps promote chemisorption with greater quantities of analysis gas. The comparisons between samples 4 and 8 with 1 and 5, respectively, shows that wet impregnation of commercially purchased $ZnCO_3$ did not enhance the adsorption capacities on CSC as much as MCM-41, where the increase was still not as great as during in-pore synthesis. This can be attributed to the larger pore volumes of the mesoporous silica compared to the biphasic material which can incorporate more of the $ZnCO_3$ leading to less agglomeration on MCM-41 than on CSC.

In-pore synthesis of $ZnCO_3$ provided highest adsorption capacities compared with wet impregnation of the commercially purchased $ZnCO_3$. This is due to the increased dispersion of the incorporated salt, which provides more reactive sites for adsorption compared with the incorporation of a crude, agglomerated salt containing minimal exposed reactive sites. Washed, in-pore synthesized $ZnCO_3$ on both CSC and MCM-41 was compared with crude impregnation of pre-synthesized $ZnCO_3$ on both CSC and MCM-41. As shown with porosimetry measurements, water washing increased pore volume by removing free, unreacted, soluble ions from the material. The importance of the removal of chlorine and potassium ions was not directly evident from capacity measurements given the inconsistency in

trends between the two substrates. Therefore, the differences in the results were attributed to the differences in the substrates. On MCM-41, a comparison between samples 2 and 3 shows an increase in capacities after washing due to newly exposed surface hydroxyl groups that may have been previously blocked by soluble potassium or chlorine ions. On CSC however, a comparison between samples 6 and 7 shows a significant reduction in NH_3 capacity and similar SO_2 capacity after washing. This was attributed to the liberation of basic carbon phase adsorption sites of the CSC after the water wash, which inhibited the adsorption of basic ammonia gas.

The in-pore synthesis of $ZnCO_3$ was also tested on other substrates. Single phase materials such as silica gel, BPL activated carbon, and a mesoporous carbon of the Norit series were impregnated with the dual functionalized salts. Breakthrough adsorption capacities of these materials are shown in Table 3.4. Results showed that upon functionalization, adsorption capacities increased. In general, consistent with the MCM-41 and CSC substrates, the poor dispersion of crudely impregnated, commercially purchased $ZnCO_3$ showed lower capacity increases as compared with the in-pore synthesis of $ZnCO_3$. When comparing the two incorporation methods as well as the washed and unwashed samples, the adsorption capacities behaved differently based on the type of substrate. The addition of impregnants significantly boosted capacities on carbon containing samples, but the improvement on silica gel was not as high. It should be noted that dual salt functionalization on Norit SX Ultra activated carbon enhanced the SO_2 capacity by approximately 120% up to 1.2 mol/kg, the highest amongst any of the materials tested. These varying trends between carbonaceous and siliceous substrates helps to signify the importance of the impregnants on CSC as compared to MCM-41, where washing with water reduced capacities on CSC. Washing these dual functionalized single phase substrates with water also decreases capacity measurements. This suggests that the soluble potassium and chlorine ions, removed from all substrates after the wash, do participate in reactions with TICs and their presence is necessary for significant

Table 3.4 NH_3 and SO_2 capacities of washed and unwashed, in-pore synthesized $ZnCO_3$ compared with solution-impregnated $ZnCO_3$ on other substrates.

Name	Adsorption Capacities	
	NH_3 (mol/kg)	SO_2 (mol/kg)
BPL Activated Carbon	0.1	0.35
K_2CO_3-$ZnCl_2$-BPL	1.3	0.64
W-K_2CO_3-$ZnCl_2$-BPL	1.2	0.59
$ZnCO_3$-BPL	1.0	0.58
Silica Gel	1.9	0.15
K_2CO_3-$ZnCl_2$-S.G.	2.5	0.15
W-K_2CO_3-$ZnCl_2$-S.G.	1.7	0.17
$ZnCO_3$-S.G.	2.3	0.20
Norit SX Ultra	0.3	0.55
K_2CO_3-$ZnCl_2$-NSXU	1.5	1.20
W-K_2CO_3-$ZnCl_2$-NSXU	1.5	0.73
$ZnCO_3$-NSXU	2.5	0.60

adsorption enhancement. Comparing single phase substrates with the biphasic CSC, when functionalized, these single phase substrates did not provide as significant of an increase in both NH_3 and SO_2 adsorption capacities.

Overall, the functionalization of various adsorbents with $ZnCO_3$ enhances the adsorption of NH_3 and SO_2. The importance of further functionalization on a biphasic adsorbent capable of targeting both adsorbates effectively is justified when comparing capacities of CSCs with other single phase adsorbents. Crude impregnation of commercially purchased $ZnCO_3$ does increase capacities, but the poor dispersion of the salt when incorporated in this way limits the effectiveness of the adsorption. On CSC, dual functionalization of K_2CO_3 and $ZnCl_2$ to form $ZnCO_3$ in pores provides the highest capacity measurements for both NH_3 and SO_2 at 4.2 and 0.59 mol/kg, respectively.

3.4 Conclusions

To further promote the gas adsorption of NH_3 and SO_2 on biphasic carbon silica composites, functionalization with $ZnCO_3$ was considered. Both biphasic CSC and multiple single phase adsorbents functionalized with soluble K_2CO_3 and $ZnCl_2$ to form insoluble $ZnCO_3$ via in-pore synthesis have been developed. Characterization using X-ray diffraction, microscopy and porosity measurements show that successful incorporation of the insoluble salt was achieved with greater dispersion as compared to crude impregnation of commercially purchased $ZnCO_3$ on CSC. In general, $ZnCO_3$ functionalization results in reduced surface areas and shifts in pore size distributions while maintaining structural integrity. Breakthrough measurements reveal a significant increase in the adsorption capacities of functionalized CSCs. Due to increased dispersion, in-pore synthesis of $ZnCO_3$ provides higher capacities than the incorporation of pre-synthesized $ZnCO_3$. In-pore synthesis of $ZnCO_3$ on the mesoporous carbon Norit SX Ultra activated carbon significantly improves SO_2 capacities up to 1.2 mol/kg. In order to target both ammonia and sulfur dioxide effectively, K_2CO_3-$ZnCl_2$-

CSC is identified as the best material with NH_3 and SO_2 capacities of 4.2 and 0.59 mol/kg, respectively.

References

(1) Fortier, H.; Zelenietz, C.; Dahn, T. R.; Westreich, P.; Stevens, D. A.; Dahn, J. R. SO_2 Adsorption Capacity of K_2CO_3-Impregnated Activated Carbon as a Function of K_2CO_3 Content Loaded by Soaking and Incipient Wetness. *Appl. Surf. Sci.*. **2007**, *253*, 3201-3207.

(2) Fortier, H.; Westreich, P.; Selig, S.; Zelenietz, C.; Dahn, J. R. Ammonia, Cyclohexane, Nitrogen and Water Adsorption Capacities of an Activated Carbon Impregnated with Increasing Amounts of $ZnCl_2$, and Designed to Chemisorb Gaseous NH_3 from an Air Stream. *J. Colloid Interface Sci.*. **2008**, *320*, 423-435.

(3) Bashkova, S.; Bandosz, T. J. Effect of Surface Chemical and Structural Heterogeneity of Copper-Based MOF/Graphite Oxide Composites on the Adsorption of Ammonia. *J. Colloid Interface Sci.*. **2014**, *417*, 109-114.

(4) Furtado, A. M. B.; Wang, Y.; Glover, T. G.; LeVan, M. D. MCM-41 Impregnated with Active Metal Sites: Synthesis, Characterization and Ammonia Adsorption. *Microporous Mesoporous Mater.*. **2011**, *142*, 730-739.

(5) Barpaga, D.; LeVan, M. D. Functionalization of carbon silica composites with active metal sites for NH_3 and SO_2 adsorption. *Microporous Mesoporous Mater.*. **2016**, *221*, 197-203.

(6) Smith, J. W. H.; Westreich, P.; Croll, L. M.; Reynolds, J. H.; Dahn, J. R. Understanding the Role of Each Ingredient in a Basic Copper Carbonate Based Impregnation Recipe for Respirator Carbons. *J. Colloid Interface Sci.*. **2009**, *337*, 313-321.

(7) Smith, J. W. H.; Westreich, P.; Smith, A. J.; Fortier, H.; Croll, L. M.; Reynolds, J. H.; Dahn, J. R. Investigation of Copper Oxide Impregnants Prepared from Various Precursors for Respirator Carbons. *J. Colloid Interface Sci.*. **2010**, *341*, 162-170.

(8) Romero, J. V.; Smith, J. W. H.; Sullivan, B. M.; Croll, L. M.; Dahn, J. R. SO_2 and NH_3 Gas Adsorption on a Ternary ZnO/CuO/$CuCl_2$ Impregnated Activated Carbon Evaluated Using Combinatorial Methods. *ACS Comb. Sci.*. **2012**, *14*, 31-37.

(9) Arcibar-Orozcoa, J. A.; Rangel-Mendeza, J. R.; Bandosz, T. J. Reactive Adsorption of SO_2 on Activated Carbons with Deposited Iron Nanoparticles. *J. Hazard. Mater.*. **2013**, *246-247*, 300-309.

(10) Furtado, A. M. B.; Barpaga, D.; Mitchell, L. A.; Wang, Y.; DeCoste, J. B.; Peterson, G. W.; LeVan, M. D. Organoalkoxysilane-Grafted Silica Composites for Acidic and Basic Gas Adsorption. *Langmuir*. **2012**, *28*, 17450-17456.

(11) Le Leuch, L. M.; Bandosz, T. J. The Role of Water and Surface Acidity on the Reactive Adsorption of Ammonia on Modified Activated Carbons. *Carbon*. **2007**, *45*, 568-578.

(12) Jal, P. K.; Patel, S.; Mishra, B. K. Chemical modification of silica surface by immobilization of functional groups for extractive concentration of metal ions. *Talanta*. **2004**, *62*, 1005-1028.

(13) Kresge, C. T.; Leonowicz, M. E.; Roth, W. J.; Vartuli, J. C.; Beck, J. S. Ordered Mesoporous Molecular Sieves Synthesized by a Liquid Crystal Template Mechanism. *Nature*. **1992**, *359*, 710-712.

(14) Glover, T. G.; Dunne, K. I.; Davis, R. J.; LeVan, M. D. Carbon-Silica Composite Adsorbent: Characterization and Adsorption of Light Gases. *Microporous Mesoporous Mater.*. **2008**, *111*, 1-11.

(15) Glover, T. G.; LeVan, M. D. Carbon-Silica Composite Adsorbent: Sensitivity to Synthesis Conditions. *Microporous Mesoporous Mater.*. **2009**, *118*, 21-27.

(16) Furtado, A. M. B.; Wang, Y.; LeVan, M. D. Carbon Silica Composites for Sulfur Dioxide and Ammonia Adsorption. *Microporous Mesoporous Mater.*. **2013**, *165*, 48-54.

(17) Froba, M.; Huwe, H. Iron (III) oxide nanoparticles within the pore system of mesoporous carbon CMK-1: intra-pore synthesis and characterization. *Microporous Mesoporous Mater.*. **2003**, *60*, 151-158.

(18) Froba, M.; Lotz, A. R. Synthesis and Characterization of $Au_5$5 Clusters within Mesoporous Silica. *Z. Anorg. Allg. Chem.*. **2005**, *631*, 2800-2805.

CHAPTER IV

FUNCTIONALIZATION OF CARBON SILICA COMPOSITES WITH INSOLUBLE PRECIPITATES VIA IN-PORE SYNTHESIS

4.1 Introduction

Many functionalities such as metal salts have been shown to provide potential chemical reactions with various adsorbates. As depicted by our previous contributions regarding this theme,[1] the addition of metal salts on adsorbent substrates enhances the capacity for toxic industrial chemicals (TICs). Water-soluble salts such as $ZnCl_2$ and K_2CO_3 have been shown to enhance NH_3 or SO_2 adsorption when functionalized individually on mesoporous silica or activated carbon. Functionalization with $Cu(NO_3)_2$ increases both NH_3 and SO_2 capacities though not as significantly as individual increases with $ZnCl_2$ and K_2CO_3 addition.[1–12]

Another approach to achieve high capacities for a variety of adsorbate molecules involves the addition of multiple impregnants on a single porous material that can diversify the types of available adsorption sites.[6] Given the effectiveness of $ZnCl_2$ and K_2CO_3 as individual impregnants, both of these salts added sequentially on one substrate have been shown to boost both NH_3 and SO_2 adsorption capacities. As a result of this dual salt functionalization, where interactions between the two are possible, a reaction between the impregnants occurs to precipitate well-dispersed, water-insoluble $ZnCO_3$. Amongst the number of metal salts available for functionalization, water-insoluble salts can also be useful for the chemisorption of TICs. However, their low solubility leads to coarse distributions and crude incorporations on a porous material, which can limit their adsorption efficiency. This in-pore synthesis via dual salt functionalization can be used to incorporate various well-dispersed insoluble precipitates on porous substrates.

The primary adsorbent used as a substrate for this functionalization is biphasic in nature. This microporous carbon silica composite (CSC) material, developed recently by

our group,[1,10–12] takes advantage of both the polar silica and nonpolar carbon phases to target a wide spectrum of adsorbates. Further functionalization with additional reactive moieties using such a substrate would only enhance the broad scale applicability of the adsorbent material. For comparison, insoluble salts can also be incorporated on the CSC precursor, MCM-41, a mesoporous silica.

Solubility rules state that metal carbonates and metal phosphates are frequently insoluble in water. Some such materials, as shown in Table 4.1, are sparingly soluble in contrast to potassium or chloride containing salts. Found to occur naturally in mineral deposits, carbonates and phosphates such as magnesite, siderite, smithsonite, malachite, bobierrite, vivianite, hopeite, and libethenite provide use in cosmetics, jewelry, food additives, drying agents, reinforcing agents, pigments, and many other applications. When incorporated in adsorbent materials, the presence of these insoluble salts is known to correlate positively with the amount of metal ion uptake, playing a critical role in regulating aquatic environments for treatment applications.[14–16] These insoluble metal salts can also be readily synthesized via precipitation reaction between water-soluble precursors like metal chlorides (XCl_2, where X = Mg^{+2}, Fe^{+2}, Zn^{+2} and Cu^{+2}) with potassium carbonate or potassium phosphate. The acidity of metal chlorides provides reactivity towards basic ammonia[1,3,7,9,13] while basicity of potassium carbonate and potassium phosphate provides strong affinity towards acid-forming sulfur dioxide gas.[1,2,7] Precipitates formed among these impregnants on CSC or MCM-41 will affect the overall acidity/basicity of the functionalized material influencing the enhancement (or lack thereof) in NH_3 and SO_2 adsorption.

In this work, the carbon silica composite is functionalized with well-dispersed, insoluble metal salts synthesized via in-pore reactions from dual salt functionalization in order to enhance the ammonia and sulfur dioxide adsorption capacities. These insoluble metal salt functionalities form within pores as a result of precipitation reactions between combinations

Table 4.1 Solubility of metal salts in water at 25°C. (g/100 mL H_2O)[17–19]

Solubility (g/100 mL H_2O)			
	Cl^-	CO_3^{-2}	PO_4^{-3}
K^+	36	111	106
Fe^{+2}	65	5.3×10^{-5}	8.8×10^{-7}
Cu^{+2}	76	1.9×10^{-4}	6.4×10^{-7}
Zn^{+2}	408	1.3×10^{-4}	1.3×10^{-6}
Mg^{+2}	56	1.6×10^{-3}	9.4×10^{-5}

of potassium carbonate and potassium phosphate with various metal chlorides. The performance of these functionalized composites are measured using full equilibrium breakthrough adsorption capacities for low concentrations of NH_3 and SO_2 gases. The differences between the impregnants leading to differences in TIC adsorption will be analyzed using pH measurements of functionalized materials. Furthermore, the synthesized materials are characterized using X-ray diffraction and porosimetry techniques to provide evidence of the incorporation as well as an understanding of the effects of functionalization.

4.2 Experimental Methods

Materials

Tetramethylammonium hydroxide pentahydrate, TMAOH (97 %), tetramethylammonium silicate solution, TMASi (99.99 %, 15-20 wt % in water), and sulfuric acid (95.0-98.0 %) were purchased from Sigma Aldrich. Hexadecyltrimethylammonium chloride, CTAC, (25 %) in water was purchased from Pfaltz and Bauer. A solution of ammonium hydroxide (29 wt.% in water) and Cab-O-Sil M5 were purchased from Fisher Scientific. Furfuryl alcohol (99%), toluene (99%), and aluminum chloride ($AlCl_3$) were purchased from Sigma Aldrich. Anhydrous salts zinc chloride ($ZnCl_2$), magnesium chloride ($MgCl_2$), copper chloride ($CuCl_2$), iron chloride ($FeCl_2$), potassium carbonate (K_2CO_3), and potassium phosphate (K_3PO_4) were purchased from Sigma Aldrich. Gas cylinders of 1500 ppmv ammonia in helium, 500 ppmv sulfur dioxide in helium, and ultrahigh purity helium were purchased from A-L Compressed Gas.

Synthesis Procedures

The synthesis procedures of the substrates MCM-41 and CSC have been thoroughly described previously.[1,7]

Dual Salt Functionalization

The synthesis of MCM-41 or CSCs with metal salts was conducted via incipient wetness impregnation. In this procedure, an aqueous solution containing the metal chloride of interest was dribbled onto the pre-synthesized substrate until wet and allowed to air dry. After removal of water through evaporation, the desired quantity of the metal chloride remained within the pores of the substrate. Another aqueous solution containing the potassium salt of interest was dribbled onto the dried substrate containing the first salt. Upon removal of water through evaporation, the desired quantity of the potassium salt now also exists in the substrate. During the addition of the potassium salt, the metal of the metal chloride and the salt of the potassium salt react via in-pore synthesis to form an insoluble metal salt within the pores of the substrate. This in-pore synthesis of an insoluble metal salt provides a well-dispersed incorporation of an impregnant which otherwise can only be added crudely onto the porous substrate.

The order in which the two soluble precursors are added was also examined. In contrast to the procedure described above, and for comparison, the same insoluble metal salts were also incorporated through the addition of the potassium salt first, followed by the addition of the metal chloride. With all impregnations, dual functionalization was performed such that 10 wt% of the final insoluble metal salt was theoretically formed on the substrate assuming 100% of the two salt precursors reacted to form the precipitate. A theoretical loading of 10 wt% was chosen given the results from previous work[1] involving metal salt incorporation on CSC, which showed that an optimal loading concentration of metal salt on microporous biphasic CSC is ∼10 - 30 wt%. The quantity of each salt combination loaded to obtain 10 wt% of insoluble precipitate onto the substrate is shown in Table 4.2.

Materials Characterization

Prior to any characterization, synthesized materials were placed in a vacuum oven at

Table 4.2 Theoretical loading of metal salts on MCM-41 and CSC.

Precipitate	Metal Salts					
	K_2CO_3	K_3PO_4	$FeCl_2$	$CuCl_2$	$ZnCl_2$	$MgCl_2$
$FeCO_3$	13 wt%	-	10 wt%	-	-	-
$CuCO_3$	11 wt%	-	-	10 wt%	-	-
$ZnCO_3$	10 wt%	-	-	-	10 wt%	-
$MgCO_3$	15 wt%	-	-	-	-	10 wt%
$Fe_3(PO_4)_2$	-	13 wt%	10 wt%	-	-	-
$Cu_3(PO_4)_2$	-	11 wt%	-	10 wt%	-	-
$Zn_3(PO_4)_2$	-	10 wt%	-	-	10 wt%	-
$Mg_3(PO_4)_2$	-	15 wt%	-	-	-	10 wt%

60°C for approximately two hours to remove any adsorbed water.

Porosimetry

For textural characterization, adsorption isotherms were measured using a Micromeritics ASAP 2020 at -196 °C with nitrogen as the analysis gas. Before analysis, approximately 0.1 g of each sample was degassed under vacuum (20 mmHg) and heated to 120 °C. The BET method was used to determine surface areas. The reported pore volumes, calculated using density functional theory, correspond to $P/P_0 \cong 0.99$. Given the slow diffusion of nitrogen in these microporous composite materials, the isotherms at partial pressures lower than 0.001 were not measured. As a result, the pore size distributions were limited to pores greater than 1 nm. However, these profiles still allow a qualitative analysis of the shifts in the distribution as a result of salt functionalization.

X-ray Diffraction

Powder X-ray diffraction patterns were used to confirm the long-range structure of the base composite material made from mesoporous silica. These patterns were obtained using a Scintag X1h/h automated powder diffractometer with Cu target, a Peltier-cooled solid-state detector, a zero background Si(5 1 0) support, and a copper X-ray tube as the radiation source.

pH Analysis

To understand the difference between each of the incorporated metal salts, the overall acidity/basicity of the adsorbent surface was determined via pH measurements. In these experiments, approximately 100 mg of the functionalized adsorbent was mixed with 10 mL of H_2O at room temperature. The pH of this solution was measured using a double junction electrode connected to a Milwaukee MW101 PH Meter. For comparison, the pH of substrate-free, metal salts in aqueous solution was also measured. To prepare this solution,

approximately 10 mg of metal salt, equivalent to the theoretical amount of metal salt loaded on 100 mg of functionalized adsorbent, was mixed with 10 mL of H_2O at room temperature. Given the small quantities of impregnant in solution, an extra batch of aqueous salt solutions was prepared and tested for reproducibility of measurements. All pH measurements were obtained after allowing the electrode to soak in solution for a minimum of 10 minutes to let the pH equilibrate at a stable quantity.

Adsorption Capacity

As a primary measure of performance, adsorption capacities for our synthesized, functionalized adsorbent materials were tested at low concentrations of both NH_3 and SO_2. These capacities were calculated with room temperature breakthrough measurements performed using an apparatus for which the schematic is shown elsewhere.[7] With accumulation of target adsorbate in the gas phase being negligible relative to that in the adsorbed phase, the capacity of the adsorbent material, n (mol adsorbate/kg adsorbent), was calculated from

$$n = \frac{F}{m} \int_0^\infty (C_0 - C)\, dt \tag{3}$$

where C_0 is the feed concentration in units of mol/m^3, and C is the effluent concentration at time t. The volumetric flow rate of gas through the adsorbent bed, F, was held constant at approximately 30 sccm. The mass of the sample, m, varied between 15-30 mg and was contained in a small cylindrical adsorbent bed with an internal diameter of 4 mm.

The standard deviations in adsorption capacities that is representative of differences between measurements on the same sample is approximately 6% and 3% for NH_3 and SO_2, respectively. These were calculated from several measurements of NH_3 and SO_2 capacities on MCM-41 synthesized from the same batch. For many of the synthesized adsorbents in this study, in order to confirm reproducibility, the materials were re-synthesized (multiple batches). This implies that deviations in capacity measurements for the same material

are due to not only the standard deviation from measurement to measurement but also differences in batch to batch synthesis of the same material. Overall, the error in NH_3 and SO_2 capacities reported, calculated using capacity measurements of MCM-41 synthesized in three separate batches, was approximately ±12% and ±9%, respectively.

4.3 Results and Discussion

To appropriately understand the effects of dual salt functionalization, representative materials were analyzed using X-ray diffraction and porosimetry techniques. These adsorbents include (1) CSC, (2) K_2CO_3-$CuCl_2$-CSC, (3) K_2CO_3-$ZnCl_2$-CSC, (4) K_2CO_3-$MgCl_2$-CSC, (5) K_2CO_3-$FeCl_2$-CSC, (6) $CuCl_2$-K_2CO_3-CSC, (7) $CuCl_2$-K_3PO_4-CSC, and (8) K_3PO_4-$CuCl_2$-CSC.

Porosimetry

Nitrogen adsorption isotherms for the selected materials are shown in Figure 4.1. The base CSC adsorbent is both microporous and mesoporous with Type I isotherm behavior. A sharp increase in adsorbed N_2 at low partial pressure was followed by a leveling off as P/P_0 approaches unity. Upon dual salt functionalization, isotherms maintain Type I behavior and the quantity of nitrogen adsorbed decreases compared to the non-impregnated CSC. This indicates the inability of nitrogen to access traditional surface adsorption sites due to pore blockage or pore filling. Insignificant differences in isotherm shape or adsorbed N_2 amounts were evident when reversing the order of dual salt functionalization. Adsorbed nitrogen amounts for functionalized materials were not influenced by the choice of metal chloride in the composite. Rather, the carbonate containing materials showed greater adsorbed nitrogen amounts than phosphate containing materials approaching saturation. Hysteresis was

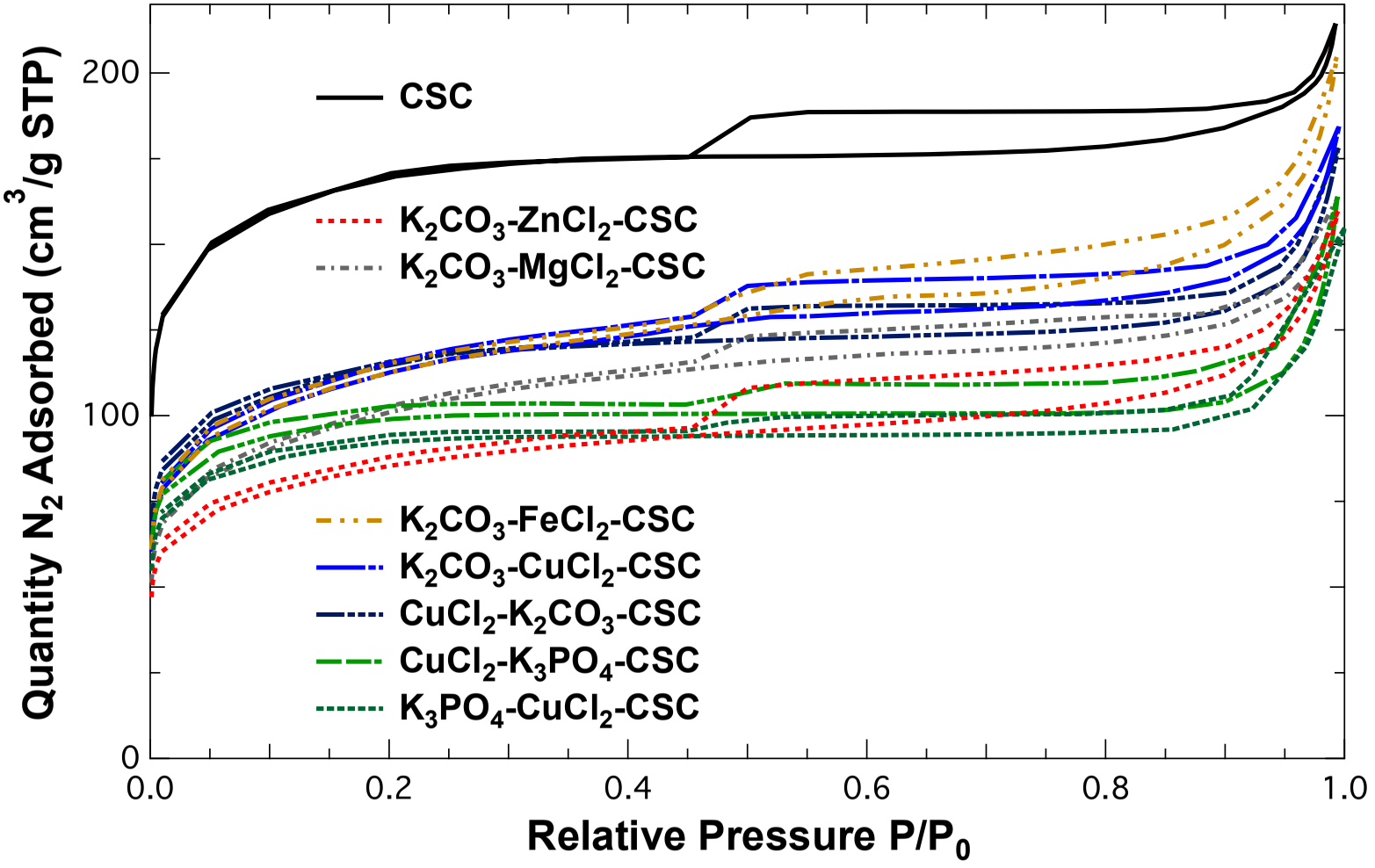

Figure 4.1. Nitrogen adsorption isotherms for select combinations of metal chlorides with potassium salts.

observed during desorption, as a result of capillary condensation in the mesopores of every sample.

Pore size distributions for the same materials are shown in Figure 4.2. The majority of the CSC pore volume has pore sizes less than 30 Å given the dominant microporosity and uniformity of pores in the composite. In general, dual salt functionalization dampened the differential pore volume amounts and broadened the distributions to larger pore sizes as a result of possible agglomeration of salt impregnants leading to pore blockage. For similar reasons, the functionalized materials also displayed larger portions of the differential pore volume in the macropore regime. No correlation between the order of salt addition or the choice of metal chloride impregnant was evident in the pore size distribution.

Adsorption isotherms also allow a quantitative analysis of textural characterization via surface area and pore volume calculations as shown in Table 4.3. Surface area measurements directly correlated to the quantity of nitrogen adsorbed, where decreasing adsorbed nitrogen amounts were consistent with decreases in surface area for functionalized materials. Upon dual salt functionalization, the BET surface area decreases compared to impregnant-free CSC. Pore volumes also decreased upon salt functionalization, as should be expected. Pore size distributions provided a measure of pore volumes at different pore regimes. Total pore volumes split into their respective micropore, mesopore, and macropore volumes are also shown in Table 4.3. As with the adsorbed nitrogen amounts, the overall surface area and pore volumes are largely unaffected by the order of the impregnant addition or the choice of metal chloride and potassium salt in the functionalized material.

X-ray Diffraction

XRD patterns shown in Figure 4.3 were analyzed to confirm the structural integrity of the synthesized adsorbents. Results for the selected functionalized materials reveal evidence of an ordered silica phase containing peaks similar to CSC. The apparent diminishing order

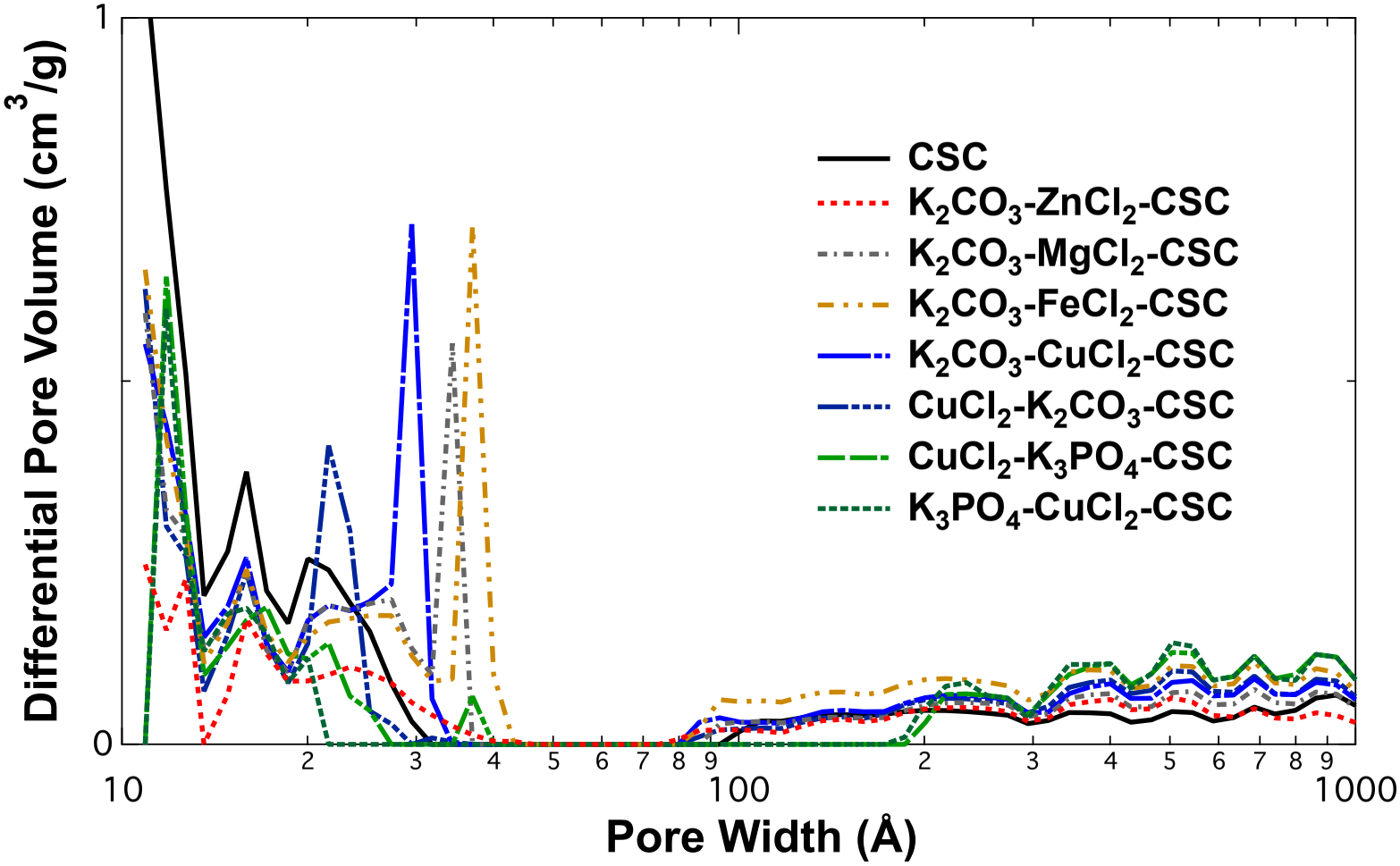

Figure 4.2. Pore size distributions for select combinations of metal chlorides with potassium salts.

Table 4.3 BET surface area and pore volumes of select combinations of metal chlorides with potassium salts.

Sample	Name	Surface Area (m^2/g)	Pore Volumes			
			Total (cm^3/g)	Micropore (cm^3/g)	Mesopore (cm^3/g)	Macropore (cm^3/g)
1	CSC	560	0.33	0.20	0.09	0.04
2	K_2CO_3-$ZnCl_2$-CSC	290	0.25	0.09	0.11	0.05
3	K_2CO_3-$MgCl_2$-CSC	340	0.25	0.09	0.11	0.05
4	K_2CO_3-$FeCl_2$-CSC	380	0.32	0.10	0.15	0.07
5	K_2CO_3-$CuCl_2$-CSC	390	0.29	0.11	0.12	0.06
6	$CuCl_2$-K_2CO_3-CSC	380	0.28	0.11	0.10	0.07
7	$CuCl_2$-K_3PO_4-CSC	320	0.25	0.09	0.06	0.10
8	K_3PO_4-$CuCl_2$-CSC	300	0.30	0.11	0.06	0.13

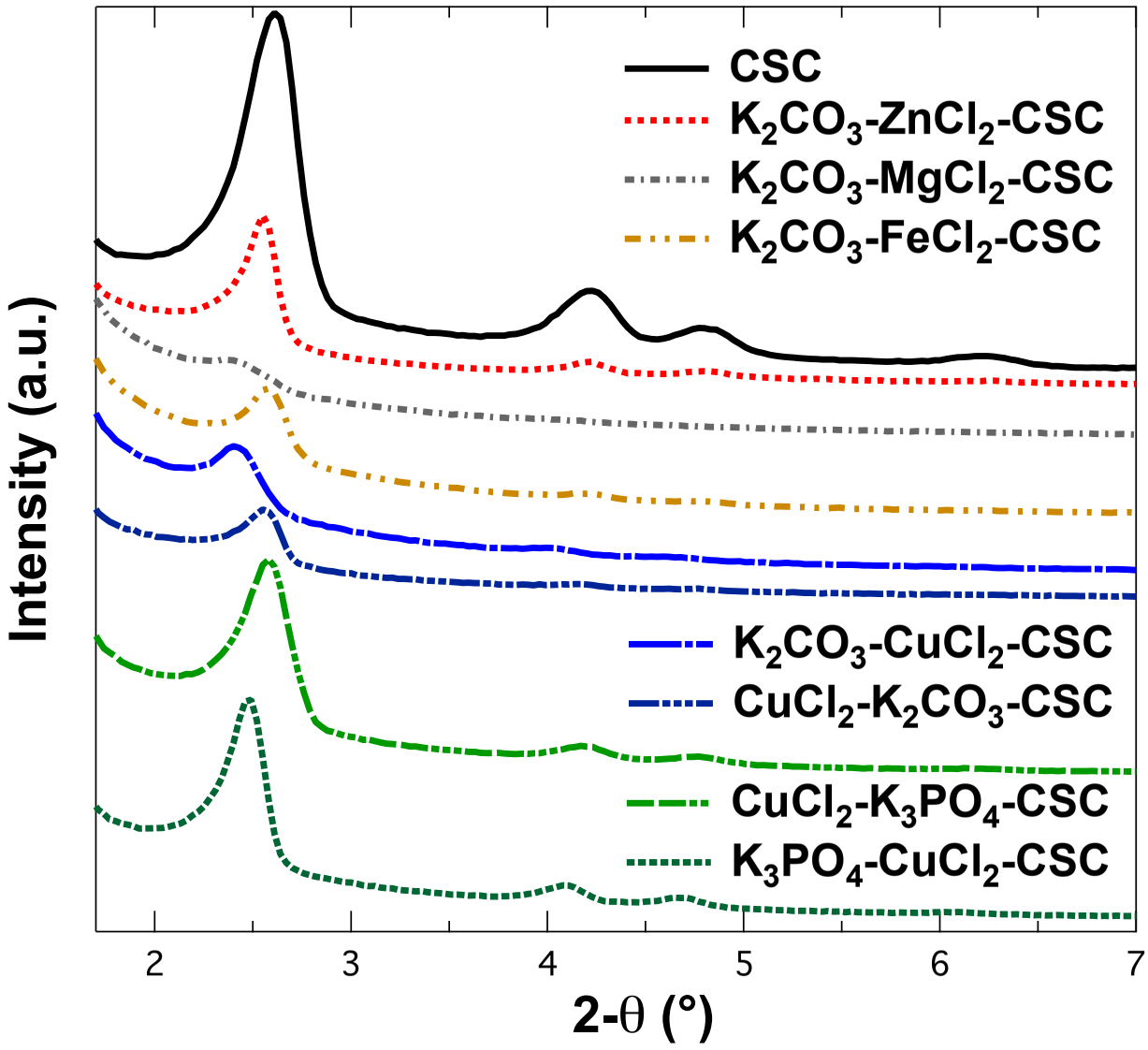

Figure 4.3. XRD patterns for select combinations of metal chlorides with potassium salts.

was likely due to interference from the incorporated state. No correlation between the acidity of metal chloride (possibly leading to reduced "crystallinity" due to dissolution of pores) and the dampening of peak intensities was evident. Rather, spectra of potassium carbonate functionalized materials showed the lowest peak intensities as compared to potassium phosphate containing materials. The insignificant shifts of all peaks among some of the materials occurs as a result of experimental error between samples.

pH Analysis

The pH of aqueous solutions containing metal salt, impregnant free substrates, and dual functionalized materials are reported in Tables 4.4 and 4.5 to gain an understanding of the nature of available adsorption sites. Between the two substrates, MCM-41 is slightly more acidic with a pH of 5.1, while CSC has a pH of 5.2. In general, after salt functionalization, composites on CSC are more acidic than on MCM-41. Amongst the basic metal salts used in this work, potassium carbonate is less basic than potassium phosphate with pHs of 10.8 and 11.5, respectively. Amongst the acidic metal chlorides, $FeCl_2$ has the lowest pH of 3.5 and $MgCl_2$ had the highest with 6.3, with the pH increasing in the order of $FeCl_2 < CuCl_2 < ZnCl_2 < MgCl_2$. Upon dual salt functionalization, the pH of the final functionalized composite varies and is not dependent on the acidity of the metal chloride. In fact, final functionalized composites are more basic in nature suggesting the effect of the potassium containing carbonate or phosphate on the overall material. Interestingly, even though K_3PO_4 itself was more basic than K_2CO_3, dual functionalization with K_3PO_4 and metal chlorides results in more acidic composite materials, with a smaller difference between the pHs of functionalized composites and metal chlorides. For both insoluble metal carbonates and insoluble metal phosphates, combinations with $ZnCl_2$ lead to an overall least basic (slightly acidic) composite on MCM-41 and CSC. In contrast, K_2CO_3 with $FeCl_2$ gives the most basic composite compared with other chlorides on MCM-41 and CSC even though iron chloride itself is more acidic than the other metal chlorides. In general, switching the order in which

Table 4.4 Adsorption capacities and pH measurements for MCM-41 and CSC materials functionalized with XCO_3 (where X = Fe^{+2}, Cu^{+2}, Zn^{+2}, Mg^{+2}).

	Sample (in 10 mL H_2O)	pH (∼0.01 M)	Capacity (mol/kg)	
			NH_3	SO_2
	MCM-41	5.1	1.8	0.05
	CSC	5.2	2.0	0.28
	K_2CO_3	10.8	-	-
$FeCO_3$	$FeCl_2$	3.5	-	-
	K_2CO_3-$FeCl_2$-MCM-41	9.4	2.2	0.49
	$FeCl_2$-K_2CO_3-MCM-41	9.2	2.1	0.42
	K_2CO_3-$FeCl_2$-CSC	9.0	1.9	0.56
	$FeCl_2$-K_2CO_3-CSC	9.0	2.6	0.46
$CuCO_3$	$CuCl_2$	4.6	-	-
	K_2CO_3-$CuCl_2$-MCM-41	8.8	2.2	0.43
	$CuCl_2$-K_2CO_3-MCM-41	9.0	1.9	0.50
	K_2CO_3-$CuCl_2$-CSC	8.3	2.4	0.49
	$CuCl_2$-K_2CO_3-CSC	8.3	2.1	0.48
$ZnCO_3$	$ZnCl_2$	5.4	-	-
	K_2CO_3-$ZnCl_2$-MCM-41	6.1	3.1	0.39
	$ZnCl_2$-K_2CO_3-MCM-41	6.2	3.0	0.52
	K_2CO_3-$ZnCl_2$-CSC	5.5	4.1	0.57
	$ZnCl_2$-K_2CO_3-CSC	6.1	3.0	0.39
$MgCO_3$	$MgCl_2$	6.3	-	-
	K_2CO_3-$MgCl_2$-MCM-41	8.5	2.5	0.23
	$MgCl_2$-K_2CO_3-MCM-41	8.6	2.6	0.34
	K_2CO_3-$MgCl_2$-CSC	8.2	2.1	0.36
	$MgCl_2$-K_2CO_3-CSC	9.4	2.4	0.51

Table 4.5 Adsorption capacities and pH measurements for MCM-41 and CSC materials functionalized with $X_3(PO_4)_2$ (where X = Fe^{+2}, Cu^{+2}, Zn^{+2}, Mg^{+2}).

	Sample (in 10 mL H_2O)	pH (∼0.01 M)	Capacity (mol/kg)	
			NH_3	SO_2
	MCM-41	5.1	1.8	0.05
	CSC	5.2	2.0	0.28
	K_3PO_4	11.5	-	-
$Fe_3(PO_4)_2$	$FeCl_2$	3.5	-	-
	K_3PO_4-$FeCl_2$-MCM-41	7.4	2.4	0.26
	$FeCl_2$-K_3PO_4-MCM-41	7.8	2.5	0.32
	K_3PO_4-$FeCl_2$-CSC	6.6	2.6	0.37
	$FeCl_2$-K_3PO_4-CSC	6.8	2.2	0.44
$Cu_3(PO_4)_2$	$CuCl_2$	4.6	-	-
	K_3PO_4-$CuCl_2$-MCM-41	6.0	2.6	0.18
	$CuCl_2$-K_3PO_4-MCM-41	6.1	3.2	0.21
	K_3PO_4-$CuCl_2$-CSC	5.1	2.7	0.38
	$CuCl_2$-K_3PO_4-CSC	5.3	3.2	0.46
$Zn_3(PO_4)_2$	$ZnCl_2$	5.4	-	-
	K_3PO_4-$ZnCl_2$-MCM-41	5.5	2.8	0.20
	$ZnCl_2$-K_3PO_4-MCM-41	5.5	3.2	0.22
	K_3PO_4-$ZnCl_2$-CSC	5.3	2.1	0.32
	$ZnCl_2$-K_3PO_4-CSC	5.6	2.0	0.36
$Mg_3(PO_4)_2$	$MgCl_2$	6.3	-	-
	K_3PO_4-$MgCl_2$-MCM-41	7.9	2.1	0.19
	$MgCl_2$-K_3PO_4-MCM-41	7.9	2.8	0.23
	K_3PO_4-$MgCl_2$-CSC	7.8	2.3	0.30
	$MgCl_2$-K_3PO_4-CSC	7.9	2.1	0.35

the chloride and the potassium containing salts were added on the substrate does not have a significant effect on the overall pH of the final material. This suggests that the individual salt impregnants are not isolated on the adsorbent, but instead react together to form similar precipitates on both analogs, regardless of the order of precursor addition.

Adsorption Capacity

The breakthrough capacities of adsorbent materials are also shown in Tables 4.4 and 4.5. For all functionalized materials, the addition of reactive metal salts via dual salt functionalization introduces additional adsorption sites and enhances NH_3 and SO_2 capacities. Differences in these increases are attributed to the various salt combinations that yield insoluble precipitates via in-pore synthesis. Given the electrostatic behavior of these TICs to form acid/base interactions with adsorbent materials, pH measurements of functionalized substrates distinguish adsorption affinity and help to justify differences in capacities. The adsorption capacity for NH_3 is similar on both CSC and MCM-41 substrates, while the SO_2 capacity is higher on CSC than on MCM-41. This can be attributed to the addition of a carbon phase in the composite which provides additional adsorption potential for both targets.

Amongst the metal carbonate impregnated materials shown in Table 4.4, the most significant increase in TIC adsorption is with K_2CO_3-$ZnCl_2$-CSC with a capacity of 4.1 and 0.57 mol/kg for NH_3 and SO_2, respectively. The order in which the salts are added to form metal carbonate slightly affected adsorption capacities. In general, adding the basic potassium carbonate last yields functionalized composites with slightly lower ammonia capacities and slightly higher sulfur dioxide capacities. Similarly, adding the acidic metal chlorides last yields slightly higher ammonia capacities and slightly lower sulfur dioxide capacities compared with the reverse order analog.

Amongst the metal phosphate impregnated materials shown in Table 4.5, the most

significant increase in TIC adsorption is with $CuCl_2$-K_3PO_4-CSC with a capacity of 3.2 and 0.46 mol/kg for NH_3 and SO_2, respectively. Interestingly, the order in which the salts are added to form metal phosphates also slightly affected adsorption capacities, but with a more distinctive trend compared with metal carbonates. Adding the potassium phosphate last yields high adsorption capacities for both TICs as compared to the reverse analog in which the metal chloride is added last. The difference in SO_2 capacities between insoluble phosphates on CSC and MCM-41 is much more significant compared to insoluble carbonates on CSC and MCM-41.

Overall, the dual functionalization of metal chlorides with potassium salts results in the in-pore synthesis of insoluble metal salts on CSCs with enhanced NH_3 and SO_2 adsorption. The pH differences between the metal carbonates and metal phosphates formed on each substrate leads to varying capacity measurements that show metal carbonates providing greater TIC adsorption than metal phosphates on both MCM-41 and CSC. On CSC, dual functionalization of K_2CO_3 and $ZnCl_2$ to form $ZnCO_3$ in pores provides the highest capacity measurements for both NH_3 and SO_2 at 4.1 and 0.57 mol/kg, respectively.

4.4 Conclusions

To further promote the gas adsorption of NH_3 and SO_2 on biphasic carbon silica composites, dual salt functionalization with combinations of metal chlorides with potassium salts were considered. Biphasic CSC and MCM-41 functionalized with two water-soluble precursors leads to the formation of insoluble precipitates via in-pore synthesis. Characterization using X-ray diffraction and porosity measurements show that successful incorporation of the insoluble salt was achieved while maintaining structural integrity. Breakthrough measurements showed an increase in the adsorption capacities of dual salt functionalized materials. Amongst the metal chlorides tested, zinc and copper chloride provided significant increases in TIC adsorption, while magnesium chloride provided the least enhancement in capacities.

Amongst the potassium salts tested, potassium carbonate yielded higher performance materials than potassium phosphate. Overall, in-pore synthesis of metal carbonates and metal phosphates on CSC and MCM-41 via dual salt functionalization resulted in significant enhancement of NH_3 and SO_2 capacities, with K_2CO_3-$ZnCl_2$-CSC as the best material.

References

(1) Barpaga, D.; LeVan, M. D. Functionalization of carbon silica composites with active metal sites for NH_3 and SO_2 adsorption. *Microporous Mesoporous Mater.*. **2016**, *221*, 197-203.

(2) Fortier, H.; Zelenietz, C.; Dahn, T. R.; Westreich, P.; Stevens, D. A.; Dahn, J. R. SO_2 Adsorption Capacity of K_2CO_3-Impregnated Activated Carbon as a Function of K_2CO_3 Content Loaded by Soaking and Incipient Wetness. *Appl. Surf. Sci.*. **2007**, *253*, 3201-3207.

(3) Fortier, H.; Westreich, P.; Selig, S.; Zelenietz, C.; Dahn, J. R. Ammonia, Cyclohexane, Nitrogen and Water Adsorption Capacities of an Activated Carbon Impregnated with Increasing Amounts of $ZnCl_2$, and Designed to Chemisorb Gaseous NH_3 from an Air Stream. *J. Colloid Interface Sci.*. **2008**, *320*, 423-435.

(4) Smith, J. W. H.; Westreich, P.; Croll, L. M.; Reynolds, J. H.; Dahn, J. R. Understanding the Role of Each Ingredient in a Basic Copper Carbonate Based Impregnation Recipe for Respirator Carbons. *J. Colloid Interface Sci.*. **2009**, *337*, 313-321.

(5) Smith, J. W. H.; Westreich, P.; Smith, A. J.; Fortier, H.; Croll, L. M.; Reynolds, J. H.; Dahn, J. R. Investigation of Copper Oxide Impregnants Prepared from Various Precursors for Respirator Carbons. *J. Colloid Interface Sci.*. **2010**, *341*, 162-170.

(6) Romero, J. V.; Smith, J. W. H.; Sullivan, B. M.; Croll, L. M.; Dahn, J. R. SO_2 and NH_3 Gas Adsorption on a Ternary $ZnO/CuO/CuCl_2$ Impregnated Activated Carbon Evaluated Using Combinatorial Methods. *ACS Comb. Sci.*. **2012**, *14*, 31-37.

(7) Furtado, A. M. B.; Wang, Y.; Glover, T. G.; LeVan, M. D. MCM-41 Impregnated with Active Metal Sites: Synthesis, Characterization and Ammonia Adsorption. *Microporous Mesoporous Mater.*. **2011**, *142*, 730-739.

(8) Arcibar-Orozcoa, J. A.; Rangel-Mendeza, J. R.; Bandosz, T. J. Reactive Adsorption of SO_2 on Activated Carbons with Deposited Iron Nanoparticles. *J. Hazard. Mater.*. **2013**, *246-247*, 300-309.

(9) Le Leuch, L. M.; Bandosz, T. J. The Role of Water and Surface Acidity on the Reactive Adsorption of Ammonia on Modified Activated Carbons. *Carbon*. **2007**, *45*, 568-578.

(10) Glover, T. G.; Dunne, K. I.; Davis, R. J.; LeVan, M. D. Carbon-Silica Composite Adsorbent: Characterization and Adsorption of Light Gases. *Microporous Mesoporous Mater.*. **2008**, *111*, 1-11.

(11) Glover, T. G.; LeVan, M. D. Carbon-Silica Composite Adsorbent: Sensitivity to Synthesis Conditions. *Microporous Mesoporous Mater.*. **2009**, *118*, 21-27.

(12) Furtado, A. M. B.; Wang, Y.; LeVan, M. D. Carbon Silica Composites for Sulfur Dioxide and Ammonia Adsorption. *Microporous Mesoporous Mater.*. **2013**, *165*, 48-54.

(13) Petit, C.; Karwacki, C.; Peterson, G.; Bandosz, T. J. Interactions of Ammonia with the Surface of Microporous Carbon Impregnated with Transition Metal Chlorides. *J. Phys. Chem. C*. **2007**, *111*, 12/05-12/14.

(14) Madrid, L.; Diazbarrientos, E. Influence of Carbonate on the Reaction of Heavy-Metals in Soils. *J. Soil Science*. **1992**, *43*, 709-721.

(15) Shahwan, T.; Zünbül, B.; Eroğlu, A. E.; Yilmaz, S. Effect of magnesium carbonate on the uptake of aqueous zinc and lead ions by natural kaolinite and clinoptilolite. *Appl. Clay Science*. **2005**, *30*, 209-218.

(16) Wersin, P.; Charlet, L.; Karthein, R.; Stumm, W. From adsorption to precipitation: Sorption of Mn^{+2} on $FeCO_3$(s). *Geochimica et Cosmochimica Acta*. **1989**, *53*, 2787-2796.

(17) Perry, R. H., and Green, D. W. (2008). Perry's chemical engineers' handbook. New York: McGraw-Hill.

(18) Olia, M. (2008) Barron's Fundamentals of Engineering Exam 2^{nd} ed. Retrieved from http://books.google.com. pg. 108

(19) Generalic, Eni. "Solubility product constants" EniG. Periodic Table of the Elements. KTF-Split, 14 Feb. 2016. Web. 3 Mar. 2016. *www.periodni.com/solubility_product_constants.html*.

CHAPTER V

CARBOXYLATE-BASED MOFS: SPECTROSCOPIC CHARACTERIZATION OF WATER EXPOSURE

5.1 Introduction

Metal-organic frameworks (MOFs) are crystalline compounds synthesized by the self assembly of metal ions coordinated to organic linker molecules. This complex network of interconnected organic and inorganic components forms well defined highly porous structures that promote the adsorption of gas molecules.[1–3] The highly modular synthesis of MOFs permits the pore structures and functionalities of these materials to be tailored based on specific applications.[4] Given the large number of metal and organic linker combinations, a diverse collection of MOFs has been synthesized in recent years.

MOFs have potential applications in industrial processes such as gas purification, catalysis, gas storage, and gas sensing.[2–15] In many of these processes, exposure to water vapor or humidity is inevitable. Therefore, for their use in such practical applications, MOF sensitivity to varying degrees of water exposure must be examined and well understood. Many studies have sought to further this understanding in recent years.[11–18] In a recent review of this topic by Burtch et al.[10] several factors concerning water stability in MOFs were presented. In general, to be thermodynamically stable towards water, the metal centers/cluster of the MOF must be inert, which depends not only on the metal-ligand bonds, but also on the reactivity of the metal-ligand cluster with water. From a kinetics standpoint, the hydrophobicity of the structure and steric factors around the metal-ligand bonds will greatly increase the activation energy of hydrolysis to allow MOF stability towards water. Thus, for long term liquid water exposure, a thermodynamically stable MOF is necessary. However, for less water exposure in the vapor phase, a MOF that is kinetically stable may suffice.[10]

In this work, the thermodynamic stability of several carboxylate-based MOFs towards water was considered. Our efforts focused on characterizing the changes in the metal-ligand clusters upon exposure of these MOFs to water. In the bulk of this study, these changes were analyzed through in situ IR and ex situ Raman spectroscopy measurements. The overall water stability of these selected MOFs cannot be judged based solely on these measurements. Rather, we aim to provide further insight and new evidence using spectroscopic techniques to compare and suggest possible mechanisms of water adsorption on these chemically similar MOFs.

Since its discovery by Chui et al.,[19] copper (II) benzene 1,3,5-tricarboxylate (Cu-BTC) has been among the most widely studied MOFs.[1,2] Containing unsaturated metal centers for improved gas adsorption, it has been investigated for separation and energy storage for gases such as hydrogen and methane.[1] Within the structure of Cu-BTC, copper paddle wheels are connected with four organic BTC (benzene 1,3,5-tricarboxylate) linkers to form a porous network.[11] Two types of pores exist: a large central pore of 9 Å diameter and surrounding pockets of 5 Å diameter.[11] Simulation studies have identified four primary sites of adsorption within the structure of Cu-BTC: (site 1) areas close to the copper atoms within the large pore, (site 2) the center of the smaller octahedral side pockets, (site 3) the windows of the side pocket, and (site 4) the center of the large pores.[20] Given the accessibility to unsaturated copper atoms (from site 1), the larger pore has been shown to be more hydrophilic than the smaller pore.[11] In general, it has been shown that polar molecules like water have a greater affinity for site 1, whereas nonpolar molecules primarily adsorb on site 2.[20]

Iron (III) benzene 1,3,5-tricarboxylate (Fe-BTC) has been notably used as a catalyst for the oxidation of benzylic compounds because it acts as a Lewis acid.[25] It has also been recently shown to remove toxic carcinogenic elements efficiently, such as arsenic from aqueous solutions.[26] Like Cu-BTC, Fe-BTC is composed of an interconnected network of iron metal (Fe^{+3}) coordinated with benzene 1,3,5-tricarboxylate. Details of the structure of this material

remain unknown and to the best of our knowledge, spectroscopic characterization after water adsorption on Fe-BTC has not been previously performed.

Aluminum(III) benzene 1,4-dicarboxylate ($Al^{III}(OH)(O_2C\text{-}C_6H_4\text{-}CO_2)$) or MIL-53,[21,22] has been shown to adsorb large quantities of CO_2 and CH_4. The structure of MIL-53 consists of a corner-sharing octahedral network of Al^{+3} bridged by hydroxyl groups to terephthalate ions of the benzene 1,4-dicarboxylate organic linker.[23] Unlike Cu-BTC, MIL-53 does not contain unsaturated metal sites available for enhanced adsorption. However, association with free hydroxyl groups and accessibility to bound metal centers through large pores promotes adsorption of gaseous adsorbates. The rhombic shaped pores present in a calcined, dehydrated form of this material are 12.8 Å long and 16.7 Å wide.[22] At room temperature and under exposure to air, MIL-53 adsorbs water within its structure.[21–24] Upon hydration and association of water molecules with metal sites, the rhombic shaped pores have been shown to compress to 7.5 Å long and 19 Å wide.[22] Heating the material reverses the pore contractions, and the water is quickly removed, resulting in the original, highly porous structure.[23] A rationale for this breathing effect[21–24] of MIL-53 had been suggested using NMR spectroscopy, which has shown that hydrogen bonding interactions between water molecules and the organic linker are responsible for the pore contraction.[22]

MOF-74 analogs have been shown to adsorb large quantities of CO_2.[12,27,28] Like Cu-BTC, these MOFs also contain unsaturated metal sites. Ni-MOF-74 and Mg-MOF-74 consist of either Ni^{+2} or Mg^{+2} metal centers connected to 2,5-dihydroxybenzenedicarboxylic acid (DOBDC). The metals bind with carboxylic acids as well as hydroxide groups available on the ligand to form 1-D pores that are 11 Å in size. The adsorption capacity of CO_2 has been shown to significantly decrease in the DOBDC series of MOFs after hydration.[12] For flue gas applications, Liu et al.[27] found that upon steaming MOF-74 analogs, the CO_2 capacity of Mg-DOBDC decreases more than that of Ni-DOBDC. This effect was attributed to the reduction potential of the metal center, where the higher the reduction potential of the metal,

the weaker the reducing agent, and the less significant the loss in CO_2 capacity after water exposure.

In this work, we report results for the exposure of these five MOFs (Cu-BTC, Fe-BTC, MIL-53(Al), Ni-DOBDC, and Mg-DOBDC) to various amounts of water, whether as vapor or as liquid. Cu-BTC, which has been well studied, is included both for comparisons and for further investigation by Raman spectroscopy. Varying levels of MOF framework hydration will be reflected in bond manipulations of the organic and inorganic moieties. The degree of change and susceptibility of characteristic bonds will be monitored and accordingly attributed to the adsorption of water molecules. The primary goal of this work is to present a sensitivity analysis of water exposure using DRIFTS and Raman spectroscopy, of which minimal results have been reported thus far for MOFs. To maintain structural integrity and avoid chemisorption, the critical bonds holding the organic and inorganic components of the MOF framework together (specifically, metal-oxygen bonds) must remain unchanged. In particular, the possible dissociation of Cu-O, Fe-O, Al-O, Ni-O and Mg-O bonds will be explored. Other physical characterization techniques, such as crystallinity and porosimetry measurements, will be used to support the effects of water exposure on the structure of these carboxylate-based MOFs.

5.2 Experimental Methods

Materials

Cu-BTC (Basolite C300), Fe-BTC (Basolite F300), and MIL-53 (Basolite A100) were purchased from Sigma Aldrich. Ni-DOBDC and Mg-DOBDC were synthesized as per previously published procedures in literature.[12,27] For Ni-DOBDC, a solvent containing 50 mL deionized water and 50 mL tetrahydrofuran was prepared in a Parr reactor. To this, 3.73 g of 2,5-dihydroxyterephthalic acid and 1.87 g of nickel acetate were added. The mixture was then heated at 110°C for 3 days, filtered, washed with water, dried, and the solvent exchanged with ethanol several times. After heating the solvent exchanged sample in an

inert nitrogen atmosphere, the evacuated pore structure of Ni-DOBDC was obtained. For Mg-DOBDC, a solvent containing 45 mL DMF, 3 mL ethanol, and 3 mL water was prepared. To this, 0.475 g of magnesium nitrate hexahydrate and 0.111 g of 2,5-dihydroxyterephthalic acid were added. The mixture was stirred well and distributed into five tightly capped vials. The vials were then heated at 125°C for 20 hours and then allowed to cool to room temperature. The mother liquor was decanted and replaced with methanol several times. After heating the solvent exchanged sample under vacuum at 250°C for 5 hours, the evacuated pore structure of Mg-DOBDC was obtained.

Water Exposure Methods

Various levels of water exposure were used to interpret structural effects: dehydrated, 50%, 80% and 100% relative humidity (RH), and immersion in liquid water. Dehydration and evacuation of physically adsorbed water molecules was performed by heating in a vacuum oven at 150 °C for 3 hours prior to characterization. For 50% RH, helium carrier gas was passed through a water sparger submersed in a cooled water bath and then fed into a saturation cell containing a MOF sample. The water bath was set to a temperature of 14 °C at a pressure of 1 atm to correspond to a relative humidity of 50% at room temperature. Similarly, for 80% and 100% RH, the water bath temperature was set to 21°C and 25°C, respectively. Samples were characterized after 24 hours of exposure. To simulate extreme water exposure, MOFs were stirred in deionized water at room temperature for 24 hours before being collected via vacuum filtration and dried overnight in air.

Physical Characterization

Powder X-ray diffraction (XRD) was used to confirm the crystallinity of MOF structures following exposure. The spectra were measured using a Scintag X1h/h automated powder diffractometer with a step size of 0.02° in two theta (2θ). A Peltier-cooled solid state

detector was used with a copper x-ray tube as the radiation source. Both the appearance and dissolution of peaks in XRD scans were interpreted as changes in the crystalline structure.

Nitrogen adsorption isotherms were measured at 77 K using a Micrometrics ASAP 2020 porosimeter with ultra high purity nitrogen gas. Before the isotherm measurement, approximately 0.5 g of the sample was degassed for at least 8 hours. Based on thermal stability and consistent with MOF literature,[15,25] the degas temperature for Cu-BTC, Fe-BTC, Ni-DOBDC, and Mg-DOBDC samples was 150 °C. The degas temperature for MIL-53 samples was 200 °C.[39] The isotherms collected were interpreted via BET theory to calculate the surface areas and porosities of the adsorbents. Pore volumes were determined using pores smaller than 1500 Å at a partial pressure approaching saturation.

Infrared Spectroscopy

Following exposure to water, the functional groups in the chemical structures of the samples were examined using infrared spectroscopy. Diffuse reflectance infrared Fourier transform spectroscopy (DRIFTS) was used to measure characteristic vibrational stretches upon light absorption in the mid-IR region, spanning 2 – 10 μm (1000 – 5000 cm^{-1}). Raman spectroscopy was used to measure characteristic vibrational stretches upon light scattering in the far-IR region, spanning 10 – 100 μm (100 – 1000 cm^{-1}).

DRIFTS

A Nicolet 6700 Fourier transform infrared (FTIR) spectrometer was used to harbor the DRIFTS accessory unit that allowed the analysis of characteristic vibrational stretches of IR active (with absorbed light causing a change in dipole moment within vibrating molecules) carboxylate groups common to the structure of each MOF. Samples of MOFs were loaded under an inert environment into a Praying Mantis high temperature reaction chamber that fits into the DRIFTS accessory unit. A high resolution, liquid nitrogen cooled mercury cadmium telluride (MCT) detector was used to collect the reflected IR beams. In situ IR

scans were collected to measure real time spectroscopic changes by configuring an apparatus to connect a constant stream of humid carrier gas to the scanning chamber of the DRIFTS accessory reaction cell. The resolution of each scan was set to 4 cm^{-1} with 128 acquisitions collected and averaged.

Starting with an initial purge with dry helium for 24 hours, the environment in the reaction chamber was made fully inert and most of the physically adsorbed water was removed. After this, the sample was regenerated by heating at a rate of 5 °C per minute to 150 °C (or 200 °C for MIL-53), held for several hours, and a subsequent IR scan was measured. Once regenerated, the sample was allowed to cool back to room temperature under helium flow. After cooling, the humid stream (representing either 50%, 80% or 100% humidity) was passed through the chamber for a period of 24 hours and another IR scan was taken. In order to test for chemically adsorbed water molecules and determine whether the original structure of the adsorbent persists, this cycle of regeneration followed by subsequent exposure was repeated four times. Interpretation of the IR scans of the regenerated material after five cycles of exposure gave an understanding of the adverse effects of chemically adsorbed water.

Raman Spectroscopy

A Renishaw inVia Raman Microscope spectrometer was used to analyze the inorganic functional moieties in samples of MOFs that are Raman-active (with scattered light causing a change in polarizability within vibrating molecules) following the varying degrees of water exposure. The samples of water exposed MOFs generated from in-situ DRIFTS were used for Raman spectroscopy measurements. Raman spectra were gathered using a 785 nm NIR diode laser and a 532 nm DPSS laser in which the output powers were limited to 5% (maximum output powers were 100mW and 50mW, respectively). The Raman scattered photons were dispersed by a 1200 lines/mm grating monochromator and collected by a CCD camera with a 50× objective lens.

5.3 Results and Discussion

Crystallinity

XRD results for Cu-BTC, Fe-BTC, and MIL-53 are shown in Figure 5.1 (a, b, and c, respectively) at select water exposure conditions. Changes in the crystal structure are apparent. From previous studies on Cu-BTC,[29] dissolution and appearance of peaks in humidified samples occurred at approximately 6° and 15°, respectively, as shown in Figure 5.1a. Kaskel et al.[11] previously showed that immersion of Cu-BTC in liquid water resulted in a significant loss of crystallinity with the diminishment of most of the characteristic peaks. Though most of the characteristic peaks did diminish after liquid water immersion, two major peaks at 10° and 12° were still evident; however, they have been shifted to the right. This shift results from a decrease in the average distance between pore centers[42] and can be attributed to a collapse in pore structure with increasing water exposure.

XRD results shown in Figure 5.1b suggest poor crystallinity in all samples of Fe-BTC including the dehydrated form as is evident by dull, broad peaks with low counts as compared to Cu-BTC. As shown by similarities in XRD patterns for Fe-BTC samples, 50% or even 100% relative humidity did not affect the crystallinity of the material. Similar to Cu-BTC, immersion in liquid water drastically reduced both the intensity of peaks and showed dissolution of characteristic peaks, such as those at 7° and 11°.

XRD results shown in Figure 5.1c suggest a minimal effect on the crystallinity of MIL-53 upon 50% relative humidity exposure, as with Fe-BTC. The MIL-53 sample immersed in liquid water shows a significant shift in characteristic peaks to the right, as well as a reduction in the intensity of those peaks. This does not imply a dissolution of larger pores to make smaller pores, as occurred with Cu-BTC. Rather, the peak shift, which is much more significant compared with Fe-BTC, can be attributed to the "breathing effect" that is well understood for MIL-53, in which the pore structure compresses upon hydration and

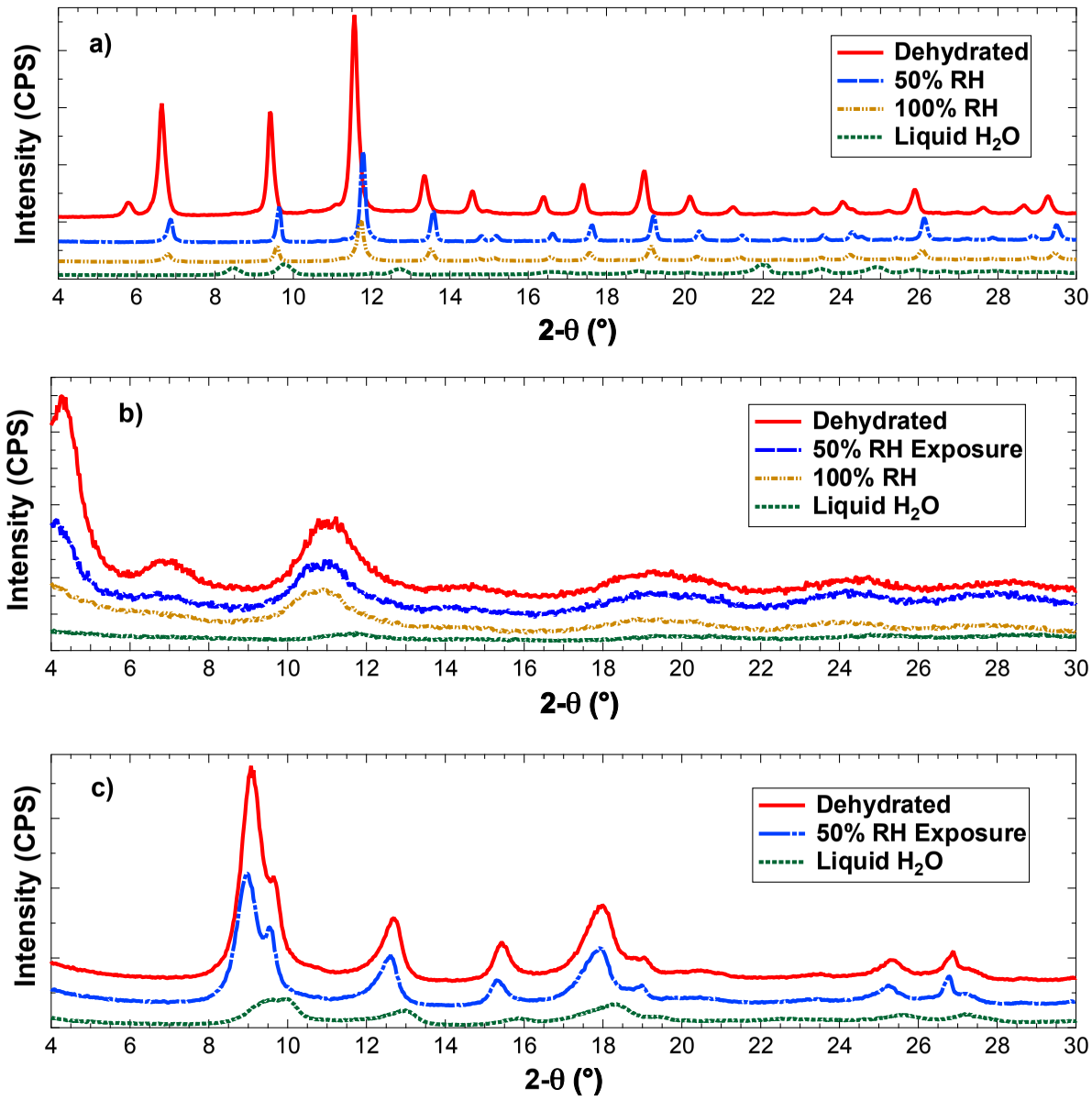

Figure 5.1. XRD patterns of (a) Cu-BTC, (b) Fe-BTC, and (c) MIL-53 samples exposed to: a dehydrated condition, 50% RH, and liquid water immersion.

decompresses upon dehydration.

Porosimetry

Nitrogen isotherms for Cu-BTC, Fe-BTC, and MIL-53 exposed to water are shown in Figure 5.2. The shape of each isotherm is classified as Type I according to IUPAC, representing the microporous nature of these MOF materials. As expected, isotherms of dehydrated samples show a higher overall quantity of nitrogen adsorbed relative to hydrated samples. All samples exposed to 50% RH show slightly less N_2 adsorption such that the low concentration of exposed water was enough to manipulate some traditional adsorption sites, but not enough to impact the overall adsorption capabilities of the MOF. After immersion in liquid water, Cu-BTC adsorbed hardly any nitrogen after re-dehydration ($\sim$95% decrease in capacity at atmospheric pressure), suggesting a loss in porosity and a lack of adsorption sites that are consumed by the chemisorption of water. Samples of Fe-BTC and MIL-53 immersed in water retained their ability to adsorb nitrogen with a capacity decrease of $\sim$10% and $\sim$25%, respectively.

Surface areas and pore volumes determined from the isotherms are shown in Table 5.1. Among the dehydrated samples, Cu-BTC has the highest available surface area. Consistent with the shift in XRD patterns for Cu-BTC, extreme water exposure significantly reduces pore volumes and surface areas. This is a result of structural degradation and the overall collapse of the crystalline framework. This was not the case for Fe-BTC, since pore volumes and surface areas were maintained even after liquid water immersion. Due to pore decompression after being degassed at its reactivation temperature, MIL-53 also maintained its surface area and pore volume after water exposure. For Fe-BTC and MIL-53, the slight decrease in measurements for samples immersed in liquid water may be attributed to any residual water trapped in the pores, even after degassing, which limits nitrogen adsorption.

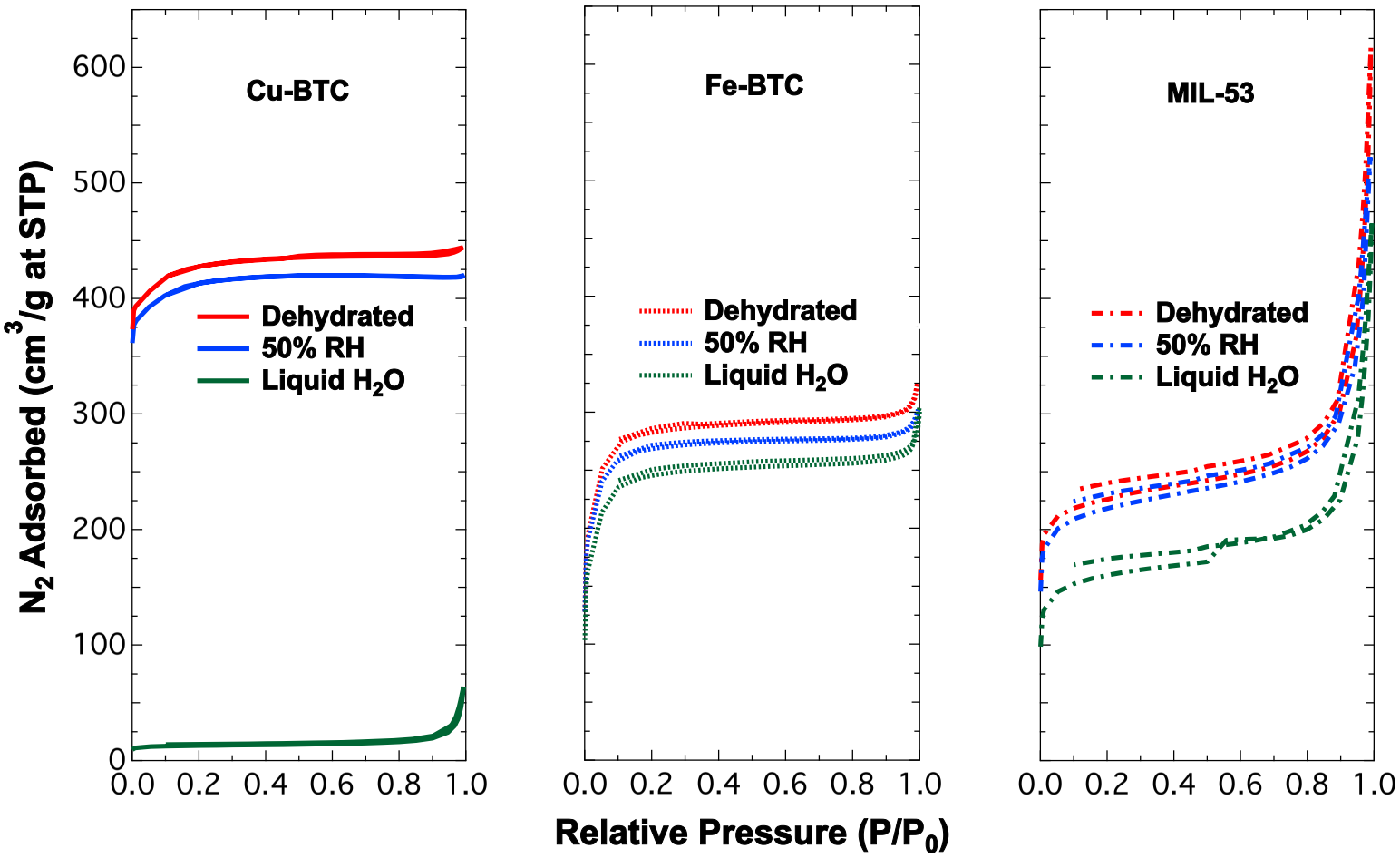

Figure 5.2. N_2 isotherms of Cu-BTC, Fe-BTC, and MIL-53 exposed to: a dehydrated condition, 50% RH, and liquid water immersion. (1 cm^3/g = 0.045 mol/kg)

Table 5.1. BET surface area and pore volumes of Cu-BTC, Fe-BTC, and MIL-53 exposed to varying amounts of water: 0% (dehydrated), 50% RH, and liquid water immersion (100%).

	Cu-BTC			Fe-BTC			MIL-53		
	0%	50%	100%	0%	50%	100%	0%	50%	100%
BET Surface Area (m^2/g)	1304	779	42	890	825	780	727	698	516
Total Pore Volume (cm^3/g)	0.65	0.48	0.10	0.50	0.47	0.47	0.95	0.81	0.72

Spectroscopy

Infrared spectroscopy data can provide an adequate understanding of which bonds are manipulated in these structures upon water exposure. The carboxylate anions within the aromatic-based organic linkers common to these MOFs are expected to react with water molecules to form carboxylic acids. On the other hand, unsaturated metal centers as well as metal-oxygen bonds may be subject to attack by water molecules given the oxidative state of the metals in the structure.

DRIFTS Spectra

Spectroscopic data from in situ DRIFTS shows the interaction of adsorbed water with the organic moieties within each MOF. Spectra shown in Figures 5.3 and 5.4 display evidence of hydration given the effects of water molecules on the protonation of the carboxylate functionality (1400–1800 cm^{-1}) present in each of the MOFs.

The chemical reaction of water molecules with the carboxylate anion is represented by the disappearance of the COO^- band (1370, 1400, 1425, and 1470 cm^{-1}) and an appearance of the COOH band (1700 - 1750 cm^{-1}). Amongst each of the MOFs, MIL-53 showed minimal changes in DRIFTS spectra of the carboxylate region. In contrast, characteristic peaks of Cu-BTC show the most significant changes upon varying levels of water exposure. Compared with Mg-DOBDC, Ni-DOBDC was able to regenerate characteristic peaks even after liquid water immersion. However, chemisorption of water was evident in Mg-DOBDC spectra as a result of permanent peak shifts and peak dissolutions. Although not shown in the spectra, water adsorption was also evident by significant broadening of peaks corresponding to hydroxyl stretches (3100–3800 cm^{-1}). Upon regeneration however, this physically adsorbed water could be removed.

Collecting infrared data during and after multiple cycles of humidity exposure allows real time bond changes to be reflected in the IR spectra. Peaks in the spectra that have been altered relative to the initial fully regenerated sample, even after dry purge and regeneration

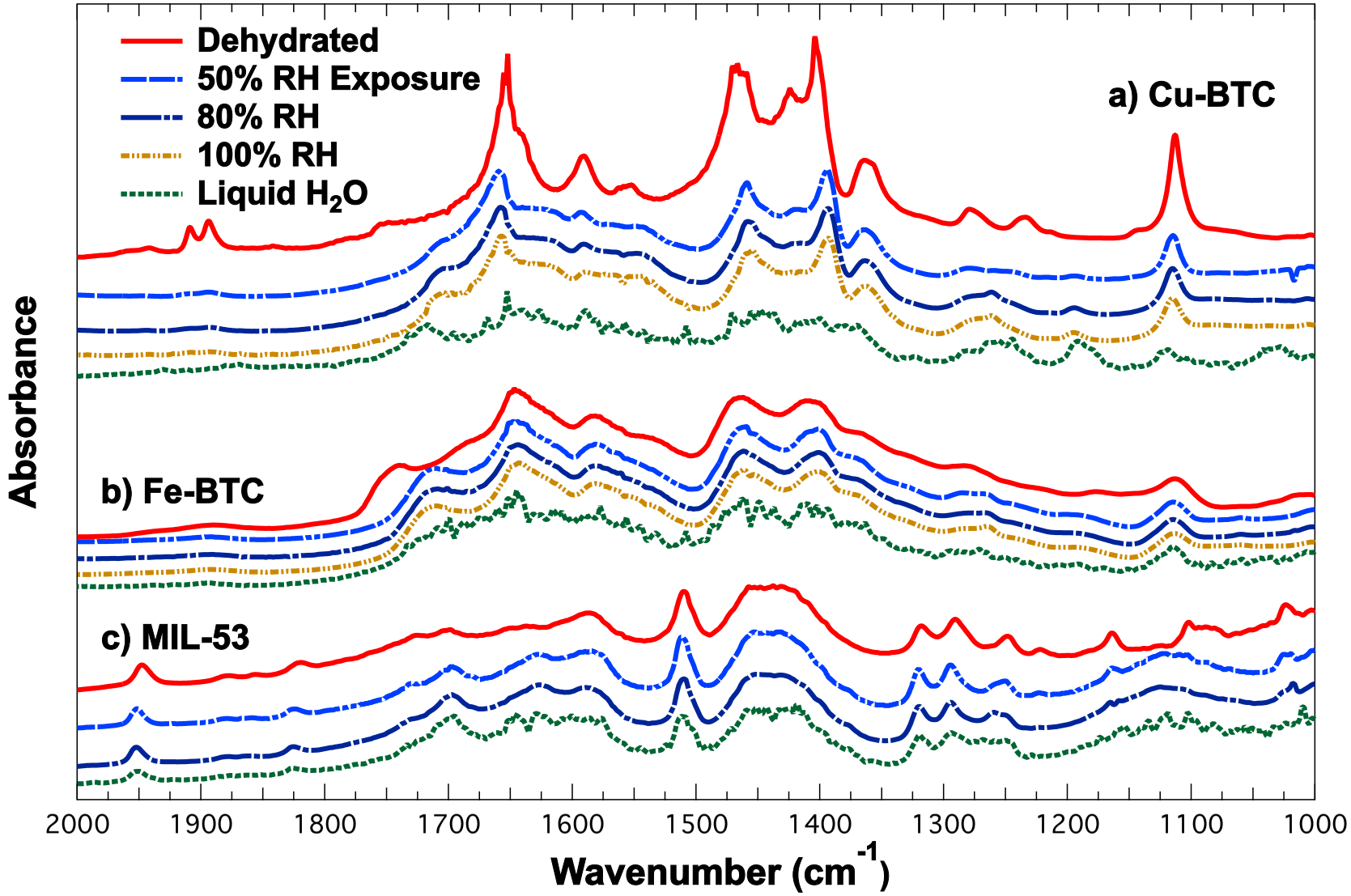

Figure 5.3. DRIFTS spectra of (a) Cu-BTC, (b) Fe-BTC, and (c) MIL-53 exposed to: a dehydrated condition, 50%, 80%, 100% RH, and liquid water immersion.

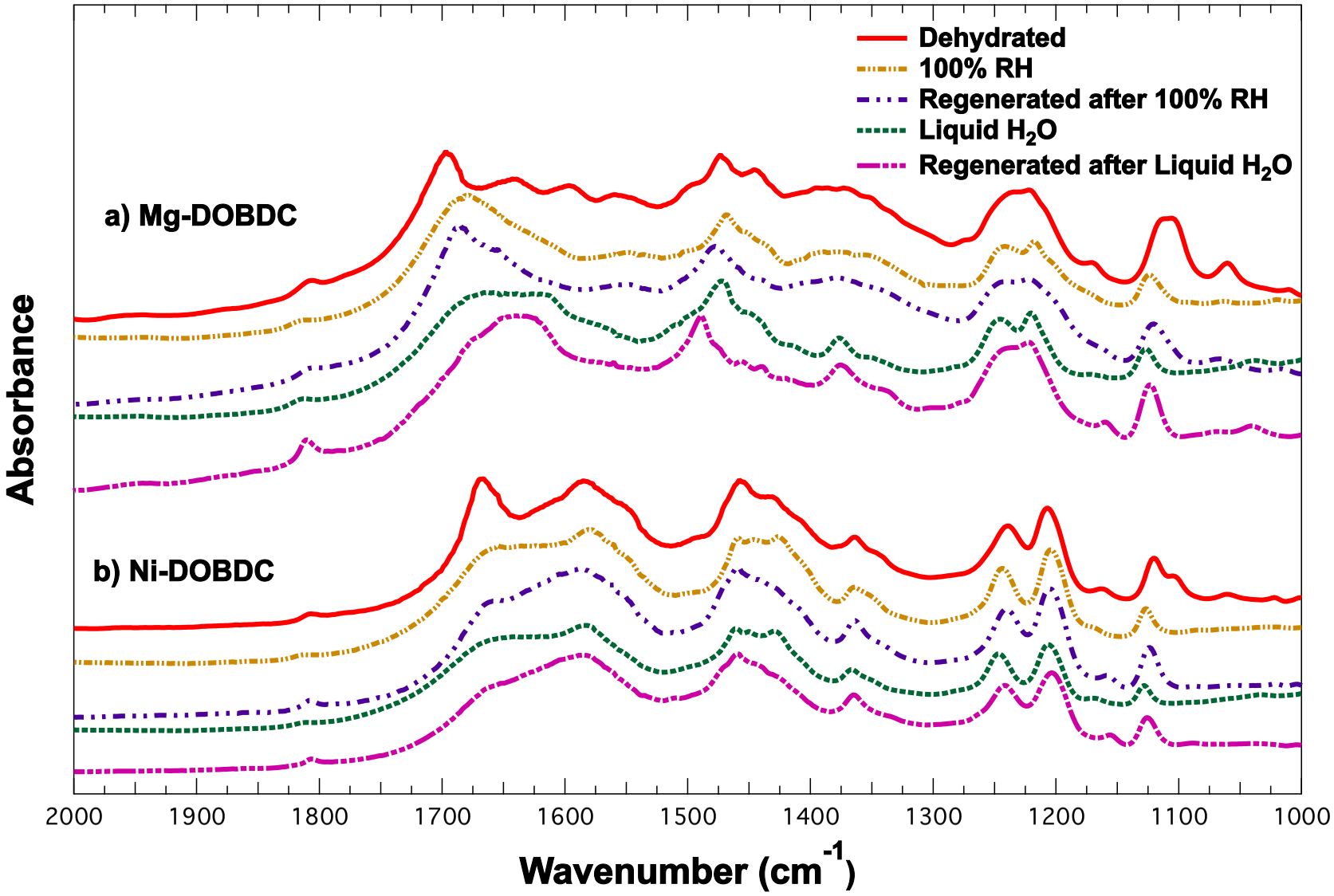

Figure 5.4. DRIFTS spectra of (a) Mg-DOBDC and (b) Ni-DOBDC exposed to: a dehydrated condition, 100% RH, regenerated after 100% RH, liquid water immersion, and regenerated after liquid water immersion.

steps, are evidence of bond changes by chemical adsorption of water that resulted in permanent structure manipulation. Evident in the DRIFTS spectra of Cu-BTC, the chemisorption of water on the framework is confirmed, as shown in Figure 5.5. In this experiment, encompassing the results of five cycles of 50% RH exposure, each scan was displayed as its difference relative to the original, non-exposed, regenerated Cu-BTC material. This depiction clearly shows the permanent appearance and disappearance of characteristic vibrational bands upon water exposure by a positive or negative absorbance difference, respectively. The scan of the regenerated material shows that after five cycles of exposure, the COO^- moiety is no longer present while the COOH functionality remains.

The lack of chemisorption in Fe-BTC, MIL-53, and Ni-DOBDC materials gives an understanding of the susceptibility of these frameworks to water molecules. Though they share similar carboxylate group functionality to Cu-BTC, it is apparent that water molecules bind reversibly to free carboxylate groups in those frameworks, and that the moieties binding the structure intact are not as susceptible to water.

Raman Spectra

Spectroscopic data from Raman scattering provides an understanding of the interaction of adsorbed water with the inorganic moieties within each MOF.

The Raman spectra for Cu-BTC, shown in Figure 5.6, displays regions associated with the Cu^{+2} ion. The Cu-Cu dimer present in the large cavity within the pore structure for the dehydrated scan is depicted by Raman shifts at 174, 230, 283 cm^{-1}.[43] Other regions associated with the Cu^{+2} ion are seen at 464 and 511 cm^{-1} correspond to stretching modes of the Cu-O bond. The remaining regions in the spectra seen at 748 and 828 cm^{-1} represent out-of-plane C-H vibrations from the benzene rings of the organic linker. Spectra show that 50% RH exposure does not significantly manipulate the bonds of Cu-BTC. However, with 100% RH and especially after immersion in liquid water, the spectra change significantly. Peaks representing Cu-Cu dimers dampen in intensity with increasing water adsorption.

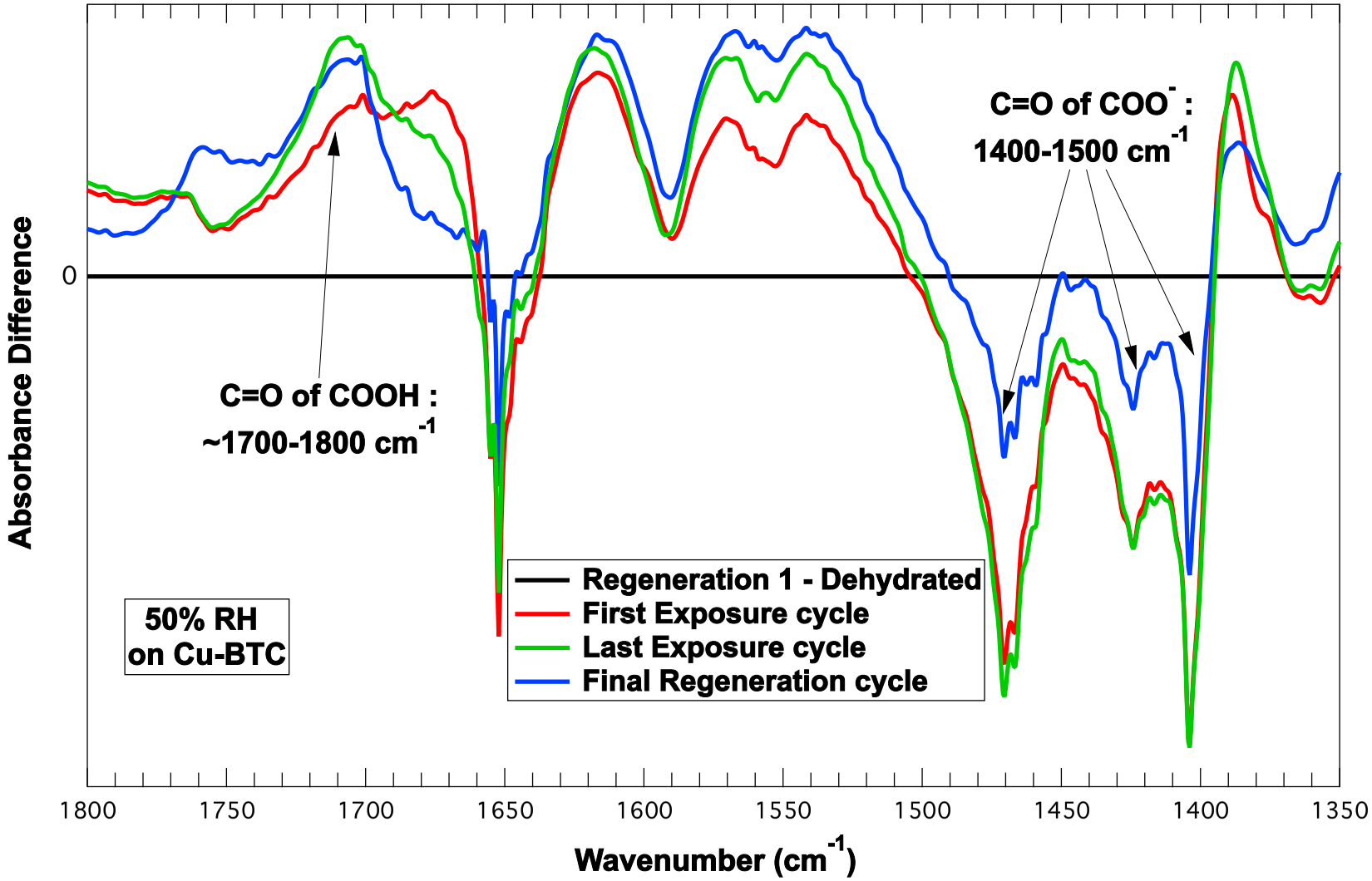

Figure 5.5. DRIFTS spectra of Cu-BTC exposed to multiple cycles of 50% RH exposure followed by He purges showing evidence of H_2O chemisorption.

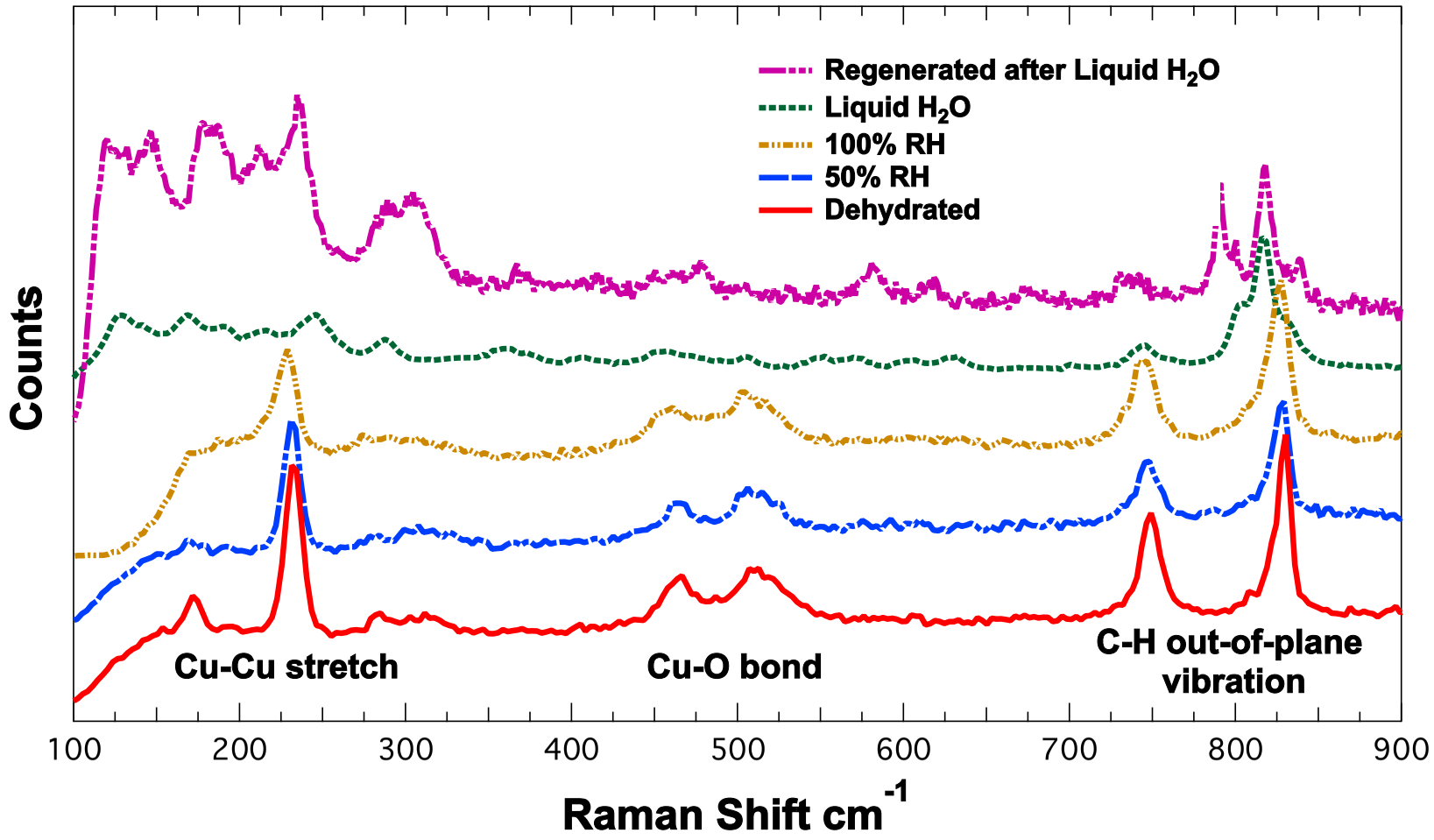

Figure 5.6. Raman spectra of Cu-BTC exposed to: a dehydrated condition, 50%, 100% RH, liquid water immersion, and regeneration after liquid water immersion.

The dissolution of characteristic peaks in this region (100 - 300 cm^{-1}) from the dehydrated sample to the relatively weak dampened peaks in the extremely hydrated sample suggests that hydrolysis of copper dimer occurs.

A similar red-shift and dampening effect is seen for characteristic peaks of the Cu-O bond upon exposure to liquid water (400 - 600 cm^{-1}), possibly due to the hydrolysis of Cu-O-C- to result in Cu-OH and OH-C-. To confirm the permanent loss of these bonds, the samples immersed in liquid water were re-dehydrated at conditions similar to the original dehydrated sample. The Raman spectra of this re-dehydrated sample show a single, low intensity peak at 478 cm^{-1} in place of two peaks corresponding to the Cu-O bond, suggesting the manipulation of Cu-O in the original structure to possibly form a new Cu-O bond after hydrolysis. Given these spectroscopic results for Cu-BTC and the loss in crystallinity, porosity, and surface area, the extreme hydration of the unsaturated metal centers in this MOF results in the cleavage of copper dimers that maintain the rigidity of the framework leading to the attack of the metal-ligand bond and the ultimate collapse of the hydrolyzed framework.

Raman spectra results for Fe-BTC, shown in Figure 5.7, are consistent with corresponding XRD and N_2 isotherm results. Characteristic peaks for Fe-O bonds reduce in intensity for the sample immersed in liquid water as a result of increased Raman scattering from physically adsorbed water molecules. However, re-dehydration of this material successfully regenerates the adsorbent to its native dehydrated form and suggests that no permanent manipulations occur to the inorganic moiety in Fe-BTC from water exposure.

The Raman spectra for MIL-53 samples were unable to be obtained due to high fluorescence from aluminum containing compounds, which masks the weaker Raman scattering intensities. However, as with the DRIFTS results for the organic carboxylate region of MIL-53, the inorganic components (consisting of Al-O bonds) are not affected by water exposure. In comparison with Cu-BTC, both MIL-53 and Fe-BTC remain unchanged after extreme water exposure. From a thermodynamic perspective, given the increased oxidative state of the

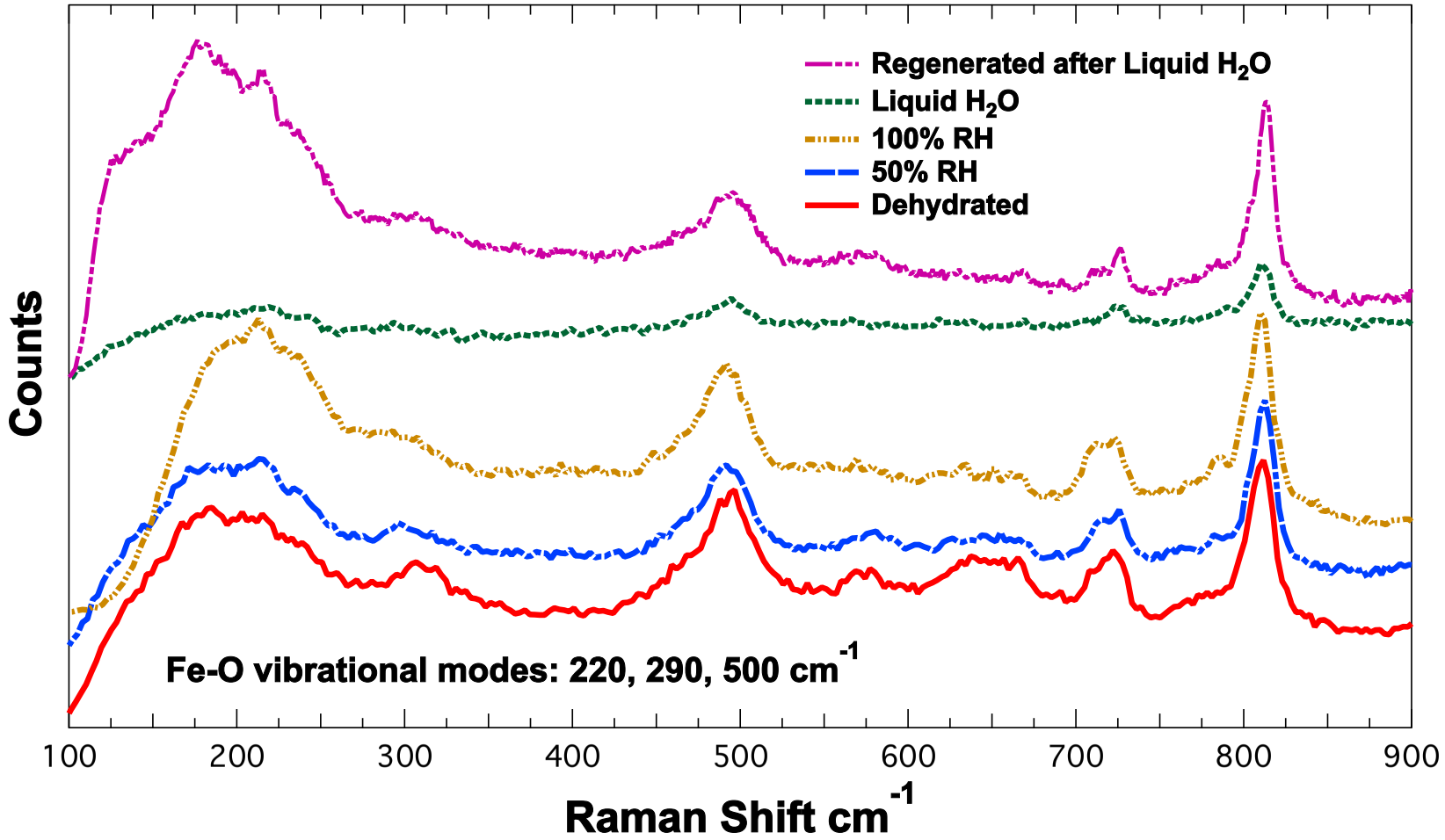

Figure 5.7. Raman spectra of Fe-BTC exposed to: a dehydrated condition, 50%, 100% RH, liquid water immersion, and regeneration after liquid water immersion.

aluminum and iron species in their respective frameworks, the smaller ionic radii must lead to a more tightly bound and rigid structure, corresponding directly with the metal-oxygen bond dissociation energies (Al-O > Fe-O > Cu-O).

Raman spectra results for Mg-DOBDC and Ni-DOBDC are shown in Figures 5.8 and 5.9, respectively. Characteristic peaks for the Mg-DOBDC sample are unable to be distinguished given the low signal-noise ratio evident in the spectra. For Ni-DOBDC, consistent with DRIFTS results, several of the characteristic peaks are regenerated even after immersion in liquid water, suggesting the poorer susceptibility of water molecules on its structure. This can be contributed to the reduction potential difference between the two MOF-74 analogs. Given the higher reduction potential of nickel compared with magnesium, the magnesium is a stronger reducing agent and more likely to react with water.[27]

5.4 Conclusions

The carboxylate-based MOFs, Cu-BTC, Fe-BTC, MIL-53, Ni-DOBDC and Mg-DOBDC have been exposed to water at varying degrees. Analysis of crystallinity and porosity measurements using XRD and N_2 isotherms gave insight on manipulations of the physical structure of each MOF upon water exposure. Interpretation of spectroscopic measurements using a humidity controlled, in situ DRIFTS apparatus, and a Raman spectrometer provided evidence for permanent structure changes due to chemisorption of water.

Characterization techniques have confirmed the well-studied susceptibility of Cu-BTC to water molecules showing evidence of chemisorption. As expected, extreme water exposure on Cu-BTC hydrolyzes the Cu-O bond. Interestingly, Raman spectroscopy results showed that copper dimers forming the backbone of the structure are susceptible to water molecules. This susceptibility is attributed to unsaturated copper sites available in the large pores of Cu-BTC that ultimately lead to a permanent collapse in the framework.

Due to a lack of unsaturated metal sites and higher bond dissociation energies, the

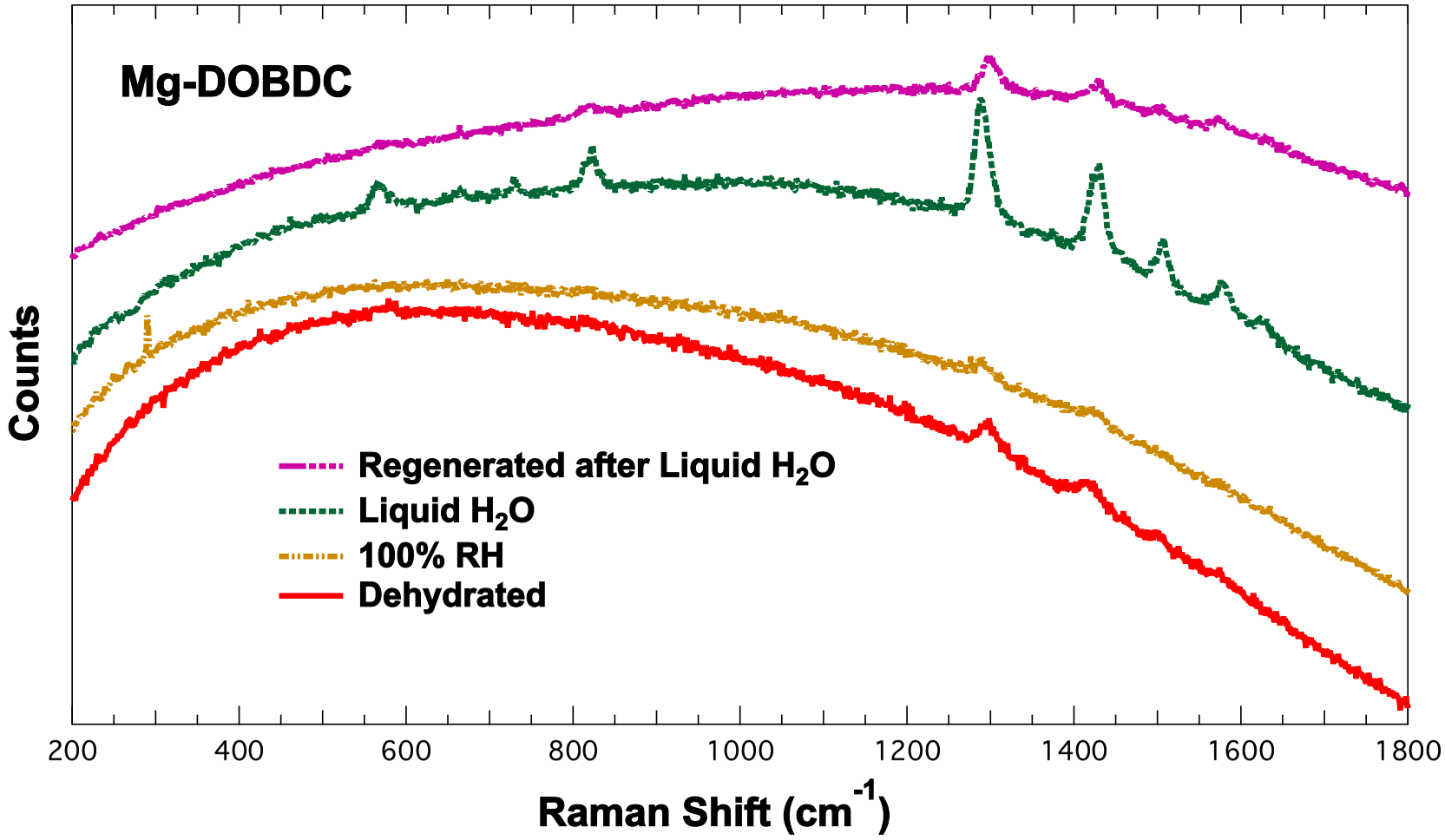

Figure 5.8. Raman spectra of Mg-DOBDC exposed to: a dehydrated condition, 100% RH, liquid water immersion, and regeneration after liquid water immersion.

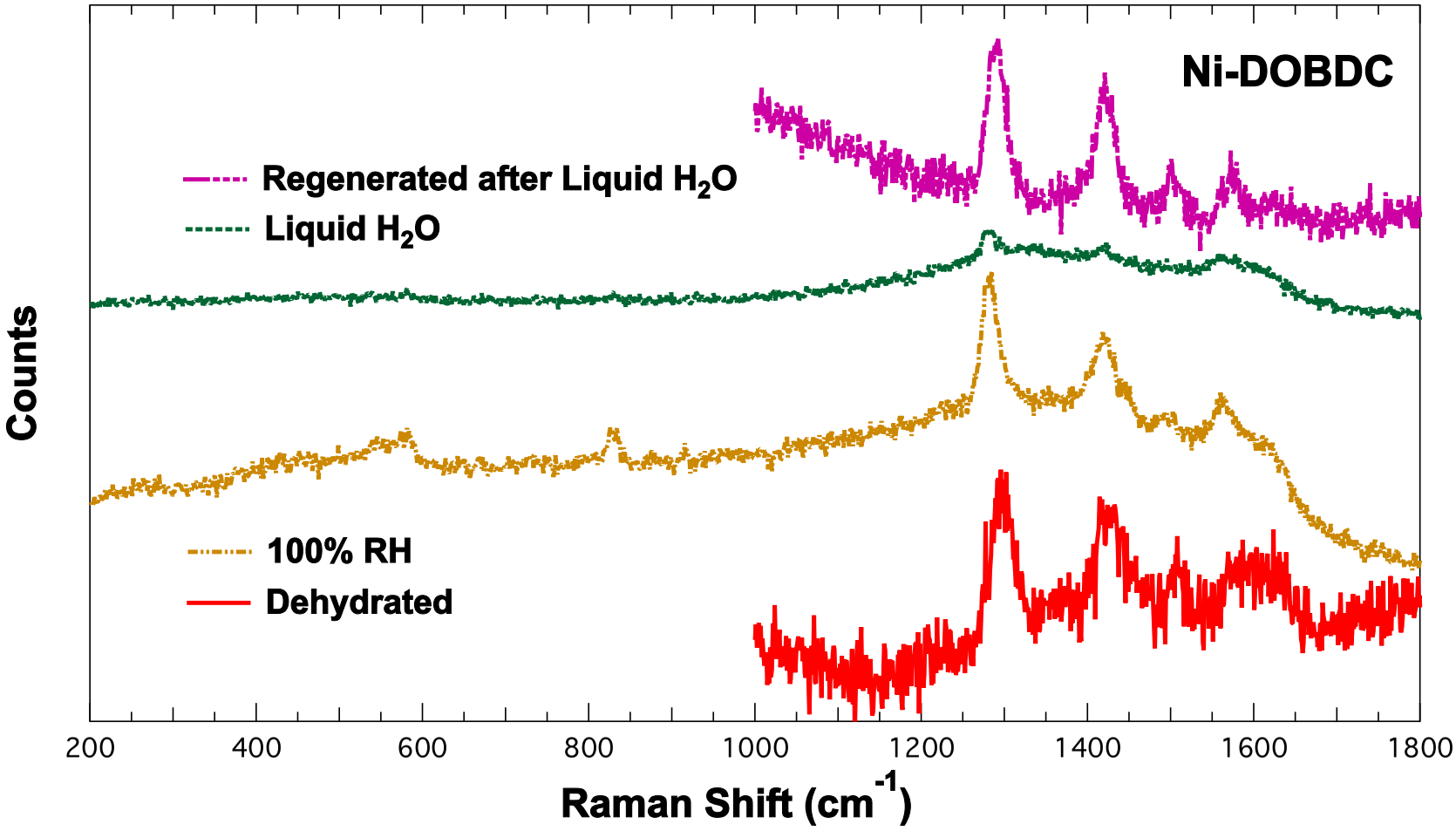

Figure 5.9. Raman spectra of Ni-DOBDC exposed to: a dehydrated condition, 100% RH, liquid water immersion, and regeneration after liquid water immersion.

frameworks of both Fe-BTC and MIL-53 remain virtually unchanged across varying degrees of water exposure. Evidence of physically adsorbed water can be seen in DRIFTS results of Fe-BTC, with regenerable spectra for re-dehydrated samples. DRIFTS spectra of MIL-53 samples remain unchanged and show minimal evidence of physically adsorbed water. Spectroscopic measurements of the organic moieties in DOBDC MOFs show much higher susceptibility of water on Mg-DOBDC leading to chemisorption at high exposure amounts.

References

(1) Karra, J. R.; and Walton, K. S. Effect of Open Metal Sites on Adsorption of Polar and Nonpolar Molecules in Metal-Organic Framework Cu-BTC. *Langmuir*. **2008**, *24*, 8620–8626.

(2) Chowdhury, P.; Bikkina, C.; Meister, D.; Dreisbach, F.; and Gumma, S. Comparison of Adsorption Isotherms on Cu-BTC Metal Organic Frameworks Synthesized from Different Routes. *Microporous Mesoporous Mater.*. **2009**, *117*, 406–413.

(3) Cheng, Y.; Kondo, A.; Noguchi, H.; Kajiro, H.; Urita, K.; Ohba, T.; Kaneko, K.; and Kanoh, H. Reversible Structural Change of Cu-MOF on Exposure to Water and its CO_2 Adsorptivity. *Langmuir*. **2009**, *25*, 4510-4513.

(4) Achmann, S.; Hagen, G.; Kita, J.; Malkowsky, I. M.; Kiener, C.; and Moos, R. Metal-Organic Frameworks for Sensing Applications in the Gas Phase. *Sensors*. **2009**, *9*, 1574-1589.

(5) Kizzie, A. C.; Wong-Foy, A. G.; and Matzger, A. J. Effect of Humidity on the Performance of Microporous Coordination Polymers as Adsorbents for CO_2 Capture. *Langmuir*. **2011**, *27*, 6368-6373.

(6) Wu, T.; Shen, L.; Luebbers, M.; Hu, C.; Chen, Q.; Ni, Z.; and Masel, R. I. Enhancing the Stability of Metal-Organic Frameworks in Humid Air by Incorporating Water Repellent Functional Groups. *Chem. Commun.*. **2010**, *46*, 6120-6122.

(7) Martín-Calvo, A.; García-Pérez, E.; García-Sánchez, A.; Bueno-Pérez, R.; Hamad, S.; and Calero, S. Effect of Air Humidity on the Removal of Carbon Tetrachloride from Air using Cu-BTC Metal-Organic Framework. *Phys. Chem. Chem. Phys.*. **2011**, *13*, 11165-11174.

(8) Jasuja, H.; Zang, J.; Sholl, D. S.; and Walton, K. S. Rational Tuning of Water Vapor and CO_2 Adsorption in Highly Stable Zr-Based MOFs. *J. Phys. Chem. C.* **2012**, *116*, 23526-23532.

(9) Jasuja, H.; Huang, Y.; and Walton, K. S. Adjusting the Stability of Metal-Organic Frameworks under Humid Conditions by Ligand Functionalization. *Langmuir.* **2012**, *28*, 16874-16880.

(10) Burtch, N. C.; Jasuja, H.; Walton, K. S. Water Stability and Adsorption in Metal-Organic Frameworks. *Chem. Rev.*. **2014**, *114*, 10575-10612.

(11) Küsgens, P.; Rose, M.; Senkovska, I.; Fröde, H.; Henschel, A.; Siegle, S.; and Kaskel, S. Characterization of Metal-Organic Frameworks by Water Adsorption. *Microporous Mesoporous Mater.*. **2009**, *120*, 325-330.

(12) Liu, J.; Wang, Y.; Benin, A. I.; Jakubczak, P.; Willis, R. R.; and LeVan, M. D. CO_2/H_2O Adsorption Equilibrium and Rates on Metal-Organic Frameworks: HKUST-1 and Ni/DOBDC. *Langmuir.* **2010**, *26*, 14301-14307.

(13) Yazaydin, A. O.; Benin, A. I.; Faheem, S. A.; Jakubczak, P.; Low, J. J.; Willis, R. R.; and Snurr, R. Q. Enhanced CO_2 Adsorption in Metal-Organic Frameworks via Occupation of Open-Metal Sites by Coordinated Water Molecules. *Chem. Mater.*. **2009**, *21*, 1425-1430.

(14) Schoenecker, P. M.; Carson, C. G.; Jasuja, H.; Flemming, C. J. J.; Walton, K. S. Effect of Water Adsorption on Retention of Structure and Surface Area of Metal-Organic Frameworks. *Ind. Eng. Chem. Res.*. **2012**, *51*, 6513-6519.

(15) DeCoste, J. B.; Peterson, G. W.; Schindler, B. J.; Killops, K. L.; Browe, M. A.; and Mahle, J. J. The Effect of Water Adsorption on the Structure of the Carboxylate

Containing Metal-Organic Frameworks Cu-BTC, Mg-MOF-74, and UiO-66. *J. Mater. Chem. A*. **2013**, *1*, 11922-11932.

(16) Liu, J.; Thallapally, P. K.; McGrail, B. P.; and Brown, D. R.. (2012). Progress in Adsorption-Based CO_2 Capture by Metal-Organic Frameworks. *Chem. Soc. Rev.* **2012**, *41*, 2308-2322.

(17) Gul-E-Noor, F.; Jee, B.; Poppl, A.; Hartmann, M.; Himsl, D.; and Bertmer, M. Effects of Varying Water Adsorption on a $Cu_3(BTC)_2$ Metal-Organic Framework (MOF) as Studied by 1H and 13C Solid-State NMR Spectroscopy. *Phys. Chem. Chem. Phys.*. **2011**, *13*, 7783-7788.

(18) Low, J.; Benin, A.; Jakubczak, P.; Abraharnian, J.; Faheem, S.; Willis, R. Virtual High Throughput Screening Confirmed Experimentally: Porous Coordination Polymer Hydration. *J. Am. Chem. Soc.*. **2009**. *131*, 15834-15842.

(19) Chui, S. S. Y.; Lo, S. M. F.; Charmant, J. P. H.; Orpen, A. G.; and Williams, I. D. A Chemically Functionalizable Nanoporous Material $[Cu_3(TMA)_2(H_2O)_3]_n$. *Science*. **1999**, *283*, 1148.

(20) Castillo, J. M.; Vlugt, T. J. H.; and Calero, S. Understanding Water Adsorption in Cu-BTC Metal-Organic Frameworks. *J. Phys. Chem. C*. **2008**, *112*, 15934-15939.

(21) Bourrelly, S.; Llewellyn, P. L.; Serre, C.; Millange, F.; and Loiseau, T. Different Adsorption Behaviors of Methane and Carbon Dioxide in the Isotypic Nanoporous Metal Terephthalates MIL-53 and MIL-47. *J. Am. Chem. Soc.*. **2005**, *127*, 13519-13521.

(22) Loiseau, T.; Serre, C.; Huguenard, C.; Fink, G.; Taulelle, F.; Henry, M.; Bataille, T. A Rationale for the Large Breathing of the Porous Aluminum Terephthalate (MIL-53) upon Hydration. *Chemistry*. **2004**, *10*, 1373-1382.

(23) Serre, C.; Millange, F.; Thouvenot, C.; Noguès, M.; Louër, D.; Féery, G. Very Large Breathing Effect in the First Nanoporous Chromium (III) Based Solids: MIL-53. *J. Am. Chem. Soc.*. **2002**, *124*, 13519-13526.

(24) Férey, G.; Latroche, M.; Serre, C.; and Millange, F. Hydrogen Adsorption in the Nanoporous Metal-Benzenedicarboxylate. *Chem. Commun.*. **2003**, *24*, 2976-2977.

(25) Dhakshinamoorthy, A.; Alvaro, M.; Chevreau, H.; Horcajada, P.; Devic, T.; Serre, C. and Garcia, H. Iron(III) Metal-Organic Frameworks as Solid Lewis Acids for the Isomerization of α-Pinene Oxide. *Catal. Sci. Tech.*. **2012**, *2*, 324-330.

(26) Zhu, B.; Yu, X.; Jia, Y.; Peng, F.; Sun, B.; Zhang, M.; Luo, T.; Liu, J.; and Huang, X. Iron and 1,3,5-Benzenetricarboxylic Metal-Organic Coordination Polymers Prepared by Solvothermal Method and their Application in Efficient As(V) Removal from Aqueous Solutions. *J. Phys. Chem.*. **2012**, *116*, 8601-8607.

(27) Liu, J.; Benin, A. I.; Furtado, A. M. B.; Jakubczak, P.; Willis, R. R.; LeVan, M. D. Stability Effects on CO_2 Adsorption for the DOBDC Series of Metal-Organic Frameworks. *Langmuir*. **2011**, *27*, 11451-11456.

(28) Yazaydin, A. O.; Snurr, R. Q.; Park, T. H.; Koh, K.; Liu, J.; LeVan, M. D.; Benin, A. I.; Jakubczak, P.; Lanuza, M.; Galloway, D. B; Low, J. J.; Willis, R. R. Screening of Metal-Organic Frameworks for Carbon Dioxide Capture from Flue Gas Using a Combined Experimental and Modeling Approach. *J. Am. Chem. Soc.*. **2009**, *131*, 18198Ð18199

(29) Schlichte, K.; Kratzke, T.; and Kaskel, S. Improved Synthesis, Thermal Stability and Catalytic Properties of the Metal-Organic Framework Compound $Cu_3(BTC)_2$. *Microporous Mesoporous Mater.*. **2004**, *73*, 81-88.

(30) Biswas, S.; Ahnfeldt, T.; and Stock, N. New Functionalized Flexible Al-MIL-53-X

(X= -Cl, -Br, -CH_3, -NO_2, -$(OH)_2$) Solids: Synthesis, Characterization, Sorption and Breathing Behavior. *Inorg. Chem.*. **2011**, *50*, 9518-9526.

(31) Drenchev, N.; Ivanova, E.; Mihaylov, M.; and Hadjiivanov, K. CO as an IR Probe Molecule for Characterization of Copper Ions in a Basolite C300 MOF Sample. *Phys. Chem. Chem. Phys.*. **2010**, *12*, 6423-6427.

(32) Karra, J. R.; and Walton, K. S. Molecular Simulations and Experimental Studies of CO_2, CO and N_2 Adsorption in Metal-Organic Frameworks. *J. Phys. Chem. C*. **2010**, *114*, 15735-15740.

(33) Marx, S.; Kleist, W. and Baiker A. Synthesis, Structural Properties, and Catalytic Behavior of Cu-BTC and Mixed Linker Cu-BTC-PyDC in the Oxidation of Benzene Derivatives. *J. Catal.*. **2011**, *281*, 76-87.

(34) Mu, B.; and Walton, K. S. Thermal Analysis and Heat Capacity Study of Metal-Organic Frameworks. *J. Phys. Chem. C*. **2011**, *115*, 22748-22754.

(35) Popovic, Z. V.; Thomsen, C.; Cardona, M.; Liu, R.; Stanisic, G.; Kremer, R.; and Konig, W. Phonon Characterization of $Bi_2(Sr_{1-x}Ca_xCuO_{6+\delta})$ by Infrared and Raman Spectroscopy. *Solid State Commun.*. **1988**, *66*, 965-969.

(36) Szanyi, J.; Daturi, M.; Clet, G.; Baer, D. R.; and Peden, C. H. F. Well-Studied Cu-BTC Still Serves Surprises: Evidence for Facile Cu^{2+}/Cu^{+} Interchange. *Phys. Chem. Chem. Phys.*. **2012**, *14*, 4383-4390.

(37) Zhao, H.; Ding, B.; Yang, E.; Wang, X.; and Zhao, X. A Novel 2-D Copper(II) Complex with Paddlewheel-like Building Block. *Z. Anorg. Allg. Chem.*. **2007**, *633*, 1735-1738.

(38) Bourrelly, S.; Moulin, B.; Rivera, A.; Maurin, G.; Devautour-Vinot, S.; Serre, C.; Daturi, M.; Lavalley, J.; Loera-Serna, S.; Denoyel, R.; Llewellyn, P.; and Férey, G.

Explanation of the Adsorption of Polar Vapors in the Highly Flexible Metal Organic Framework MIL-53(Cr). *J. Am. Chem. Soc.*. **2010**, *132*, 9488-9498.

(39) Heymans, N.; Vaesen, S.; and Weireld, G. D. A Complete Procedure for Acidic Gas Separation by Adsorption of MIL-53(Al). *Microporous Mesoporous Mater.*. **2012**, *154*, 93-99.

(40) Rallapalli, P.; Prasanth, K. P.; Patil, D.; Somani, R. S.; Jasra, R. V.; and Bajaj, H. C. Sorption Studies of CO_2, CH_4, N_2, CO, O_2 and Ar on Nanoporous Aluminum Terephthalate [MIL-53(Al)]. *J. Porous Mater.*. **2010**, *18*, 205-210.

(41) Si, X.; Zhang, J.; Li, F.; Jiao, C.; Wang, S.; Liu, S.; Li, Z.; Zhou, H.; Sun, L.; and Xu, F. Adjustable Structure Transition and Improved Gases (H_2, CO_2) Adsorption Property of Metal-Organic Framework MIL-53 by Encapsulation of BNH_x. *Dalton Trans.*. **2012**, *41*, 3119-3122.

(42) Sheppard D. A.; and Buckley C. E. Hydrogen Adsorption on Porous Silica. *Int. J. Hydrogen Energy*. **2008**, *33*, 1688-1692.

(43) Prestipino, C.; Regli, L.; Vitillo, J. G.; Bonino, F.; Damin, A.; Lamberti, C.; Zecchina, A.; Solari, P. L.; Kongshaug, K. O.; and Bordiga, S. Local Structure of Framework Cu(II) in HKUST-1 Metallorganic Framework: Spectroscopic Characterization upon Activation and Interaction with Adsorbates. *Chem. Mater.*. **2006**, *18*, 1337-1346

CHAPTER VI

CONCLUSIONS AND RECOMMENDATIONS

This dissertation focused on the development and characterization of novel materials used for high adsorption performance of both acidic and basic light gases. These adsorbents were incorporated with metal salts either by further functionalization of pre-synthesized substrates or as precursors in the formation of porous composites like metal-organic frameworks (MOFs). The biphasic substrate primarily used in this work was made up of a mesoporous silica derived from MCM-41 and a microporous carbon made from a polymerized alcohol. This carbon silica composite (CSC) was further functionalized by water-soluble metal salts in both single impregnations as well as dual salt incorporation. With MOFs, a characterization analysis was performed to interpret the degradation (or lack thereof) of chemical bonds within the framework that were susceptible to water adsorption.

In brief, the principal findings of this research are:

Single, salt impregnations on MCM-41 and CSC

- Various water-soluble metal salts were added to CSC, as well as MCM-41 for comparison, at concentrations ranging from 10-65 wt%. Their well-dispersed incorporation resulted in increased microporosity and reduced surface areas while maintaining structural integrity.
- Optimal metal salt loading concentrations between 10-30 wt% on CSCs and 30-50 wt% on MCM-41 yielded highest adsorption capacities.
- For NH_3 adsorption, $ZnCl_2$-CSC was most effective with a capacity as high as 5.8 mol/kg. For SO_2 adsorption, K_2CO_3-CSC was most effective with a capacity as high as

0.51 mol/kg. In order to target both adsorbates with one material, [30 wt% $Cu(NO_3)_2$]-CSC was identified as the best compromise with NH_3 and SO_2 capacities of 4.0 and 0.45 mol/kg, respectively.

In-pore synthesis of $ZnCO_3$ on CSC and various single phase adsorbents

- The CSC and multiple single phase adsorbents were functionalized with both K_2CO_3 and $ZnCl_2$ sequentially to consolidate their high NH_3 and SO_2 adsorption performance. This combination resulted in the formation of insoluble $ZnCO_3$ within the pores. This functionalization represents a novel in-pore synthesis method to incorporate otherwise water-insoluble salts as well-dispersed precipitates on porous materials.

- Characterization using X-ray diffraction, microscopy, and porosity measurements showed that successful incorporation of the insoluble salt was achieved with greater dispersion as compared to crude impregnation of pre-synthesized $ZnCO_3$ on CSC. In general, $ZnCO_3$ functionalization results in reduced surface areas and shifts in pore size distributions while maintaining structural integrity.

- Breakthrough measurements reveal a significant increase in the adsorption capacities of $ZnCO_3$ functionalized CSCs. Due to increased dispersion, in-pore synthesis of $ZnCO_3$ provides higher capacities than the incorporation of pre-synthesized $ZnCO_3$.

- In-pore synthesis of $ZnCO_3$ on the mesoporous carbon Norit SX Ultra activated carbon significantly improves SO_2 capacities up to 1.2 mol/kg.

- In order to target both ammonia and sulfur dioxide effectively, K_2CO_3-$ZnCl_2$-CSC is identified as the best material with NH_3 and SO_2 capacities of 4.2 and 0.59 mol/kg, respectively.

Dual salt functionalization on MCM-41 and CSC

- CSC and MCM-41 were functionalized with combinations of potassium carbonate and potassium phosphate with various metal chlorides leading to the formation of insoluble precipitates via in-pore synthesis.
- The adsorption capacities of all dual salt functionalized materials was shown to increase. Amongst the metal chlorides tested, zinc and copper chloride provided significant increases in TIC adsorption, while magnesium chloride provided the least enhancement in capacities. Amongst the potassium salts tested, potassium carbonate containing composites yielded higher performance materials than potassium phosphate.
- Overall, in-pore synthesis of metal carbonates and metal phosphates on CSC and MCM-41 via dual salt functionalization resulted in significant enhancement of NH_3 and SO_2 capacities, with K_2CO_3 and $ZnCl_2$ identified as the best material.

Spectroscopic analysis of water susceptibility on MOFs

- The carboxylate-based MOFs, Cu-BTC, Fe-BTC, MIL-53, Ni-DOBDC, and Mg-DOBDC were exposed to water at varying degrees.
- The well-studied susceptibility of Cu-BTC to water molecules is confirmed by evidence of chemisorption with DRIFTS. As expected, extreme water exposure on Cu-BTC hydrolyzes the Cu-O bond. Interestingly, Raman spectroscopy results showed that IR signatures for copper dimers forming the backbone of the structure disappear. This susceptibility was attributed to unsaturated copper sites available in the large pores of Cu-BTC that ultimately lead to a permanent collapse in the framework.
- Due to a lack of unsaturated metal sites and higher bond dissociation energies, the frameworks of both Fe-BTC and MIL-53 remain virtually unchanged across varying degrees of water exposure. Evidence of physically adsorbed water can be seen in DRIFTS

results of Fe-BTC, with regenerable spectra for re-dehydrated samples. DRIFTS spectra of MIL-53 samples remain unchanged and show minimal evidence of physically adsorbed water.

- Spectroscopic measurements of the organic moieties in DOBDC MOFs show much higher susceptibility of water on Mg-DOBDC leading to chemisorption at high exposure amounts.

Some recommendations that may provide potential opportunities to extend this work include:

- The CSC can be optimized by identifying various other combinations of mesoporous silica templates with self-polymerizing alcohols such as SBA-15 with acetylene dicarboxylic acid. A composite containing a larger pore structure could accommodate increased amounts of functional moieties to enhance TIC adsorption.

- The application of MOF materials for TIC adsorption is promising. To address stability issues, the least water-susceptible MOFs can be analyzed with breakthrough measurements and infrared spectroscopy with in situ DRIFTS to analyze real time manipulations in characteristic peaks representative of structural changes upon NH_3 and SO_2 adsorption.

- Given the high SO_2 adsorption capacities obtained via the bridging and terminal hydroxyl groups of $Zr(OH)_4$ and the high NH_3 adsorption capacities with surface hydroxyl groups of mesoporous silica such as MCM-41, a hybrid composite material to consolidate two such phases may yield a promising multifunctional adsorbent.

- The functionalization of metal salts on a support such as $Zr(OH)_4$ should be considered. Although the impregnants are expected to coordinate and react themselves with the hydroxyl groups of the structure, they may maintain reactive potential to supplement additional adsorption of various other substrates.

- The stability issues of promising functionalized adsorbents containing metal salts added via incipient wetness should be considered. In humid environments, water-soluble impregnants are expected to be released and reduce the adsorption capabilities of the material.